Jakob Aichberger, BSc

Model-based Analysis and Design of Spread Spectrum Techniques to Improve EMC of Voltage Source Inverters in Automotive Applications

MASTER'S THESIS

to achieve the university degree
Diplom-Ingenieur
Master's degree programme: Electrical engineering

submitted to

Graz University of Technology

Supervisor:

Ass.Prof. Dipl.-Ing. Dr.techn. Klaus Krischan
Electric Drives and Machines Institute
Graz University of Technology

Co-Supervisor:

Univ.-Prof. Dipl.-Ing. Dr.techn. Bernd Deutschmann
Institute of Electronics
Graz University of Technology

Graz, February 2019

Affidavit

I declare that I have authored this thesis independently, that I have not used other than the declared sources/resources, and that I have explicitly indicated all material which has been quoted either literally or by content from the sources used. The text document uploaded to TUGRAZonline is identical to the present master's thesis.

18.02.2019

date

signature

Preface

This piece of work is the result of my master's thesis which deals with the reduction of electromagnetic emissions of a prototype of an electric drive system developed by the *Engineering Center Steyr GmbH & Co KG* (ECS). As the research scope comprises both the topic of electric drive systems as well as the topic of Electromagnetic Compatibilty, the thesis was realized by a cooperation between the *Electric Drives and Machines Institute* (EAM) and the *Institue of Electronics* (IFE) of the *Graz University of Technology* (TUG).

At this point, I would like to especially thank Dipl.-Ing. Thomas Karer, head of the electronic hardware development of the ECS who made it possible to do this project at the company.

A special thanks also goes to Ass.Prof. Dipl.-Ing. Dr.techn. Klaus Krischan of the EAM who supported me dedicatedly on the subjects of power electronics, electric drives and spectral analysis.

May I also express my gratitude to Univ.-Prof. Dipl.-Ing. Dr.techn. Bernd Deutschmann of the IFE for helping me with expert advice regarding the topics of Electromagnetic Compatibilty and the spread spectrum techniques.

On the part of the ECS, my warmest thanks to Dipl.-Ing. Patrick Lamplmayr and Markus Kratzer, MSc for the great collaboration and the excellent support.

Moreover, I would like to pay particular thanks to my parents, Margarete and Kurt, for their mental and financial support during my academic training and who also accepted a two-year break from my studies in order to play an active part in the Formula Student team of the TUG.

Let me conclude with heartfelt thanks to my girlfriend Britta for encouraging me during my studies as well as for proofreading this thesis.

Abstract

Electromagnetic compatibility (EMC) is gaining more and more relevance in the design and development of electronic devices and systems. Especially in electronic power converters for electric drive systems, the power density increases rapidly whereby less space remains for filtering at the same time.

One common strategy for reducing switching losses in power electronics is to reduce the switching times of the power semiconductors in order to minimize the overlapping section in which voltage and current perform opposing transitions in halfbridge configurations. The reduction of the switching times is equivalent to the increase of the signals' slew rates and thereby results in a higher amount of electromagnetic emission (EME) which often leads to a dilemma between efficiency and EMC behavior.

Therefore, so-called spread spectrum techniques can be applied in switching electronic power devices that allow an emission reduction by spreading narrowband emissions over a wider frequency range. Fortunately, some applications do not require changes on the systems' hardware but only on its software by using appropriate switching schemes of the pulse width modulated signals (PWM signals). For this reason, using spread spectrum in electronic power converters can lead to a reduction of the filter effort and further on to a saving of costs, particularly in high volume productions.

In this thesis, spread spectrum is applied to an electric drive system consisting of a 48V MOSFET based 6-phase voltage source inverter and a dual 3-phase permanent magnet synchronous motor (PMSM) by manipulating its control signals in order to reduce electromagnetic emissions caused by the switching activity of the MOSFET switches. At first, the effects of different spread spectrum approaches on the Fourier spectrum are analyzed in the sense of a rough preselection. Then, the development of a simulation model for the evaluation of conducted electromagnetic emissions (CE) will be presented. This will permit an analysis with regard to the measuring system according to the standards CISPR25 [1] and CISPR16 [2]. Hence, the CE generated by the electronic under test (EUT) can, on the one hand, be estimated in advance. On the other hand, the model will aid to optimize the spread spectrum techniques investigated especially for the considered EUT during the design process. The spread spectrum techniques which show the best overall performance when it comes to a broadband emission reduction are implemented in software and verfied by measurements afterwards. At last, an approach is presented which allows the systematic reduction of the peak- and average-detector values used in EMI test receivers.

Kurzfassung

In der Entwicklung elektronischer Geräte und Systeme erlangt die Elektromagnetische Verträglichkeit (EMV) eine immer größer werdende Bedeutung. Vor allem in leistungselektronischen Anwendungen, wie in der elektrischen Antriebstechnik oder der Elektromobilität, steigt die Leistungsdichte stetig an, wodurch weniger Bauraum für die Filterung hochfrequenter, elektromagnetischer Störemissionen verbleibt. Für die verwendeten Leistungshalbleiter werden dabei stets kürzere Schaltzeiten angestrebt, um deren Verlustleistung während des Schaltens so klein wie möglich zu halten. Die resultierenden steileren Schaltflanken wirken sich jedoch negativ auf die elektromagnetische Störaussendung elektronischer Geräte aus und führen somit zu einem Dilemma zwischen Effizienz und elektromagnetischer Verträglichkeit.

In derartigen schaltenden Anwendungen können sogenannte *Spread Spectrum* Verfahren eingesetzt werden, welche durch Manipulation der pulsweiten-modulierten (PWM) Steuersignale eine Streuung der schmalbandigen Störenergie in ein breiteres Frequenzband bewirken und in weiterer Folge eine Emissionsreduktion erlauben. Einige Anwendungen benötigen dabei keine Änderung in deren Hardware, sondern können lediglich durch den Einsatz geeigneter Pulsmuster für die Leistungshalbleiter umgesetzt werden. Aus diesem Grund stellt *Spread Spectrum* eine Möglichkeit dar, den Filteraufwand zu reduzieren und somit auch die damit verbundenen Kosten, besonders bei hohen Produktionszahlen, zu senken.

Diese Arbeit beschäftigt sich mit der Analyse verschiedener *Spread Spectrum* Verfahren anhand eines automotiven Antriebssystems, bestehend aus einem 6-phasigen Pulswechselrichter mit 48V Spannungszwischenkreis und einer doppelt-dreiphasigen, permanenterregten Synchronmaschine. Im Sinne einer groben Vorselektion werden dabei zuerst die untersuchten Verfahren auf jeweils eine Phase des Systems angewandt und deren Auswirkung auf das Fourier Spektrum der Phasenspannung analysiert. Anschließend wird die Entwicklung eines Simulationsmodells zur Evaluierung leitungsgeführter Störemissionen vorgestellt, welches unter Rücksichtnahme auf die zugrundeliegenden Standards CISPR25 [1] und CISPR16 [2] bzw. auf deren Messverfahren entworfen wird. Diese Herangehensweise erlaubt somit einerseits eine Abschätzung der tatsächlichen, durch das reale System hervorgerufenen *Peak*- und *Average*-Störemissionen, und dient andererseits für die weitere Eingrenzung geeigneter *Spread Spectrum* Verfahren. Diejenigen Verfahren, welche in der Simulation die beste Emissionsunterdrückung erreichen, werden danach in Software umgesetzt und abschließend durch Messungen verifiziert. Zudem werden die Vor- und Nachteile von *Spread Spectrum* anhand von Simulationen und Messungen diskutiert, und des weiteren Vorschläge für die systematische *Peak*- und *Average*-Emissionsreduktion für den späteren Einsatz präsentiert.

Contents

Abbreviations

CE	Conducted (electromagnetic) emission
EMC	Electromagnetic compatibility
EME	Electromagnetic emission
EMI	Electromagnetic interference
EUT	Electronic und test
FM	Frequency modulation
PWM	Pulse width modulation
PMSM	Permanent magnet synchronous motor
SVM	Space vector modulation
RCF	Randomized carrier frequency
RPP	Randomized pulse position

Chapter 1

Introduction

In order to reduce electromagnetic emissions, spread spectrum utilizes the signal energy distribution at the signal's fundamental frequency and its harmonics over a wider frequency range. As a further consequence, this leads to the reduction of the frequency spectral components' peaks since the total signal energy stays unchanged (see figure 1.1). Therefore, it is a commonly used strategy to reduce electromagnetic emissions in switch mode electronic systems.

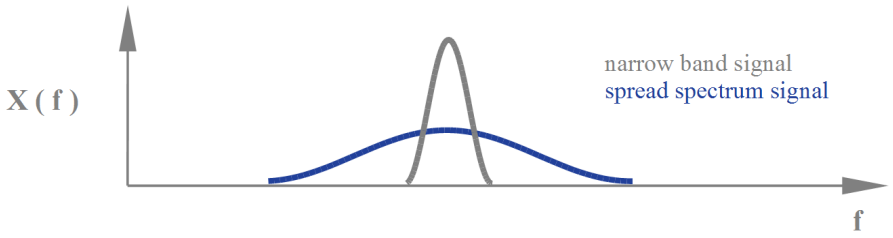

Figure 1.1: Spread spectrum concept

Due to the unfavorable properties of rectangular signals, spread spectrum is commonly utilized in systems in which digital signals with high frequencies and high signal slopes are used. For example, this could also be a clock signal inside a PC. Hence, from the EMC point of view, a fast switching of low voltages can be as problematic as a slow switching of high voltages. Therefore, spread spectrum applications range from high frequency chargepumps in the MHz range, to low power DCDC converters in the sub MHz range to very high power converters for electric drive systems or electric power generation in the kHz or even in the sub kHz range.

The system on which the effects of spread spectrum should be analyzed, and subsequently applied to, consists of a 48V MOSFET based 6-phase voltage source inverter and a dual 3-phase permanent magnet synchronous motor (PMSM) which is depicted in the block diagram in figure 1.2.

Thereby, the spread spectrum technique to be developed should manipulate the control signals of the MOSFET Gates generated by two independet space vector modulation blocks (SV PWM) for the corresponding 3-phase systems UVW and XYZ.

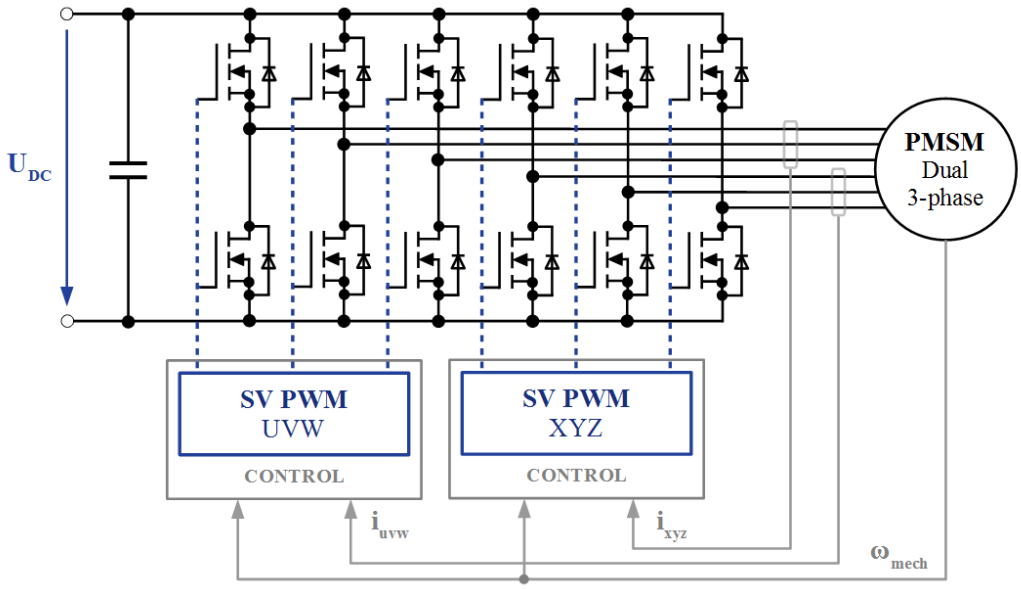

Figure 1.2: Overview of the system where spread spectrum should be applied

1.1 Motivation

Even though the strategy of spread spectrum has been known for a long time it is often applied in an unfavorable way. When it comes to electric drive systems, the spread spectrum techniques are often conducted in the same manner or considered incomplete. In other cases, for example, the performance of the used spread spectrum strategies are only evaluated by the Fourier spectrum and do not take the properties of the EMI measuring system into account. With regard to EMC, this can in consequence cause a loss of performance of the spread spectrum method in an application.

The purpose of this work is to clarify why a good understanding of the interaction between the used spread spectrum method and the EMI measuring system is essential to obtain maximum output of the spread spectrum technique used in voltage source DC to AC converters in electric drive systems.

1.2 Outline

Chapter 2 discusses various spread spectrum techniques which could be promising to be applied in electronic power converters for electric drives. To understand both the theory of the control signals used in electric drive systems and of the spectral analysis, the most important basics and notations are declared in chapter 3. For a well-founded development of an appropriate spread spectrum technique the methodology for setting up an efficient and sufficiently valid simulation model which comprises all relevant system components is described in chapter 5. The following chapter 6 analyzes two different spread spectrum methods based on the simulation model which comprises a critical reflection by naming the advantages and disadvantages of using spread spectrum in an application. In chapter 7 the simulations are verfied by measurements. It also provides a suitable spread spectrum parameter setting for the drive system considered. The last chapter 8 examines topics related to spread spectrum techniques which are not treated sufficiently and which could be investigated in the future.

Chapter 2

State of the Art and Literature Research

Spreading the energy of a narrow band signal over a wider frequency range can be done in different ways and in many areas of application. To convey a differentiated perspective of possible methods and which systems are well suitable to apply spread spectrum techniques a selection of previous works is presented in this chapter in the sense of a literature research.

In section 2.1, on the one hand, several selected non-deterministic spread spectrum approaches and their applications are presented. Section 2.3, on the other hand, points out the deterministic spread spectrum methods and where they are used most commonly. The last section 2.4 provides a tabular summarization of the treated literature.

2.1 Possible Spread Spectrum Approaches

The basic concept of spread spectrum is the variation of one or more signal parameters in a way that the average value or information stays unchanged over time. For example, considering a PWM signal, in which the information corresponds to the signal's duty cycle, there are two parameters that can be varied over time without affecting the average value of the information. If in addition the mean value of the duty cycle is equivalent to the original one as well, there are three parameters in total. Namely the signal period T, the position p of the pulse within the period and the duty cycle d itself.

The signal depicted in figure 2.1(a) has a constant period T, a constant position of the pulse center p and a constant duty cycle of d=50%. The signals in figure 2.1(b)–(d), however, show a variation of the parameters p, d and T over time. If the averaging is carried out over the four demonstrated signal periods the voltage-time area matches with the description in figure 2.1(a) with constant parameters. If, in sense of spectral analysis, the observation time of the signal is chosen longer than one signal cycle, more than one component will appear in the frequency spectrum, as the new signal edges do not coincide exactly with the original edge positions anymore.

Another factor is the manner of how and how fast these parameters are varied over time. This can be done either deterministically or not deterministically in a random way as can be seen in figure 2.2. A deterministic scheme, for example, can be a triangular waveform as illustrated in figure 2.2(a).

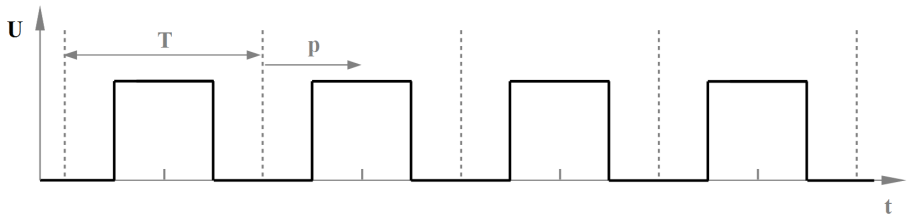

(a) constant pulse center p, duty cycle d and period

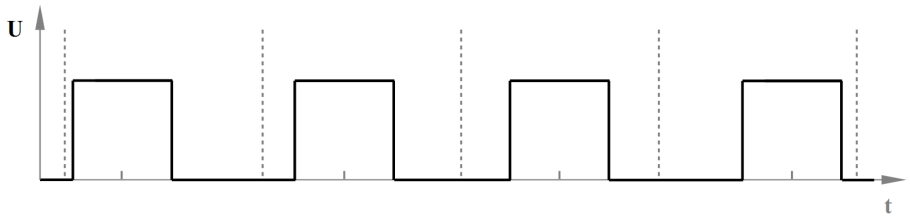

(b) varition of the pulse center p

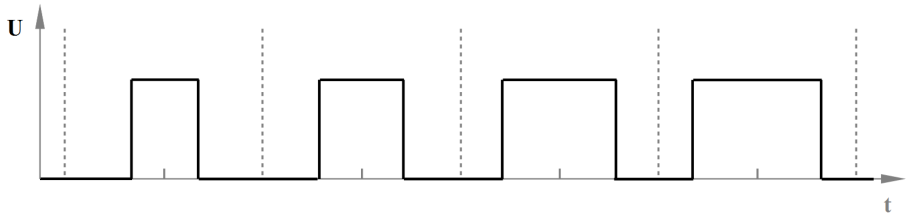

(c) variation of the duty cycle d

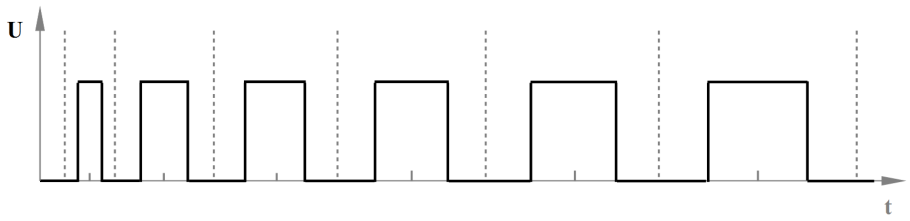

(d) variation of the period T

Figure 2.1: Possible parameter variations for PWM signals

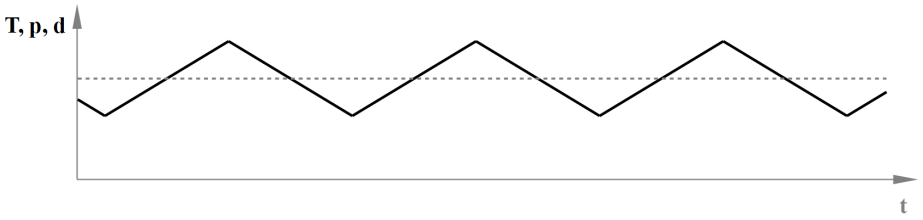

(a) Deterministic scheme

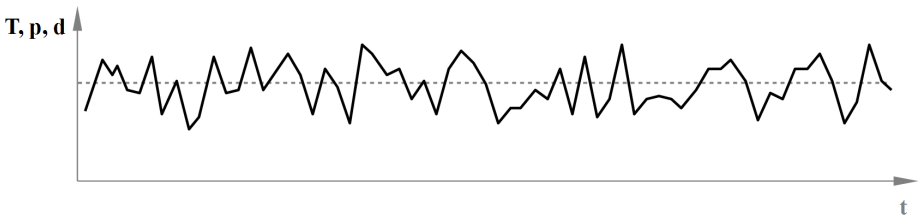

(b) Non-determinictic scheme

Figure 2.2: Deterministic- and non-deterministic spread spectrum scheme

In some publications, the chosen spread spectrum method interestingly correlates with the type of application.

For example, there is much literature as [3], [4], [5], [6], [7], which treat non-deterministic spread spectrum methods in DC to AC converters in electric drive systems in order to reduce both electromagnetic- and acoustic emissions.

In applications for lower power as used in charge pumps or DCDC converters, however, deterministic spread spectrum approaches are discussed in [8], [9], [10], [11], to reduce electromagnetic emissions more specifically by considering different detectors used in EMI measurement systems as well.

2.2 Non-deterministic Spread Spectrum Techniques

A common approach for the application of spread spectrum in PWM inverters for electric drives is the randomization of the pulse position within the PWM period with different implementations.

In [4], for example, a non-deterministic spread spectrum scheme is applied to a 5-phase DC to AC inverter which uses both random switching periods and pulse positions for the space vector modulation. The latter is reached by randomizing the distribution of the two possible zero vectors, where all phases are either tied to the positive or negative DC link potential.

Another approach for spread sprectrum in a DC to AC converter for an induction motor is presented in [6], where the pulse positions depend on a random selection from one out of two carrier signals with the same frequency. Figure 2.3(a) shows the principle of generating a symmetric center aligned PWM signal U_{out} from the reference signal U_{ref} with the use of a triangular carrier signal U_{car}. An inverted triangular carrier on the other hand leads to a splitting of the PWM signal's ON time which

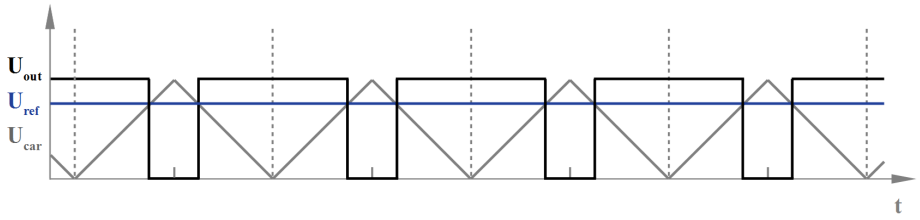

(a) Triangular carrier

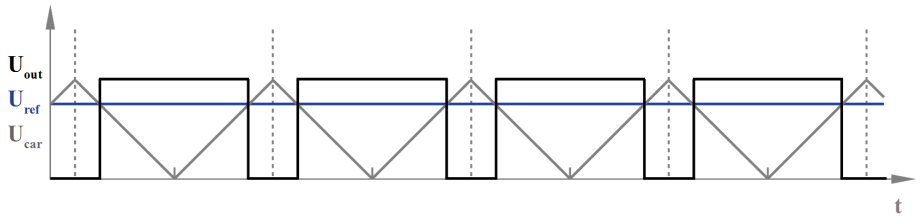

(b) Inverted triangular carrier

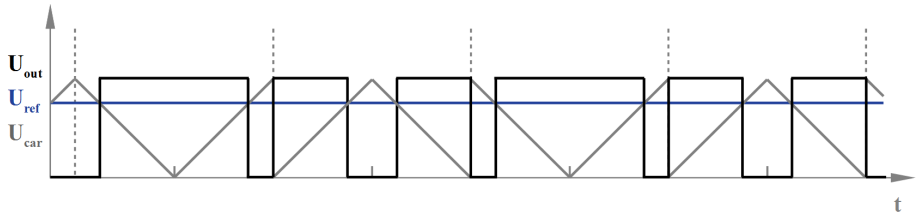

(c) Random selection between triangluar- and inverted triangular carrier

Figure 2.3: Variation of the pulse position due to random carrier selection

results in a time shift for a constant reference signal as depicted in figure 2.3(b). If the carrier is selected in a random manner as in figure 2.3(c), the output signal's PWM pattern will be random as well, without affecting its duty cycle d.

This, in turn, does not have any influence on the mean value of the output voltage, as the voltage-time area which corresponds to the reference signal stays unchanged.

A different implementation for random pulse position PWM for the use in inverter driven motors is also presented in [7]. Unlike the previous method, the pulse can be shifted contiuously over time, which leads to a higher variance and further on to a more random distribution of the pulses positions. In addition, the PWM period is randomized by a random selection of carrier signals with different frequencies which leads to an even higher variance of the signal shape.

2.3 Deterministic Spread Spectrum Techniques

Deterministic schemes apply the frequency modulation (FM) to the presented parameters as the period, pulse position or the duty cycle in which the PWM period seems to be the most effective one and is therefore most used in spread spectrum techniques.

There are three key parameters in the application of the frequency modulation in [9], [8], [11], namely the maximum frequency deviation Δf_c, the modulation time T_m and the modulation profile.

The frequency deviation defines the maximum excursion from the nominal PWM frequency $f_{c,nom}$ and has the greatest influence on the spreading effect. This can be performed either symmetrically around or beginning from $f_{c,nom}$ in the positive or negative direction, as also referred to as center-spreading, up-spreading or down-spreading scheme. The higher Δf_c is chosen, the wider is the occupied bandwidth of the fundamental frequency and its harmonics. As these bandwidths depend on the harmonic order, there is a certain point at which the bandwidths and their sidebands start to overlap. This has a negative influence on the emission level and thus is a limiting factor for the implementation.

The second key parameter in deterministic spread spectrum schemes is the modulation time T_m (or the modulation frequency f_m). It defines the distance between the harmonics sidebands and influences the distribution of the spectral energy as well. An appropriate selection of these parameters strongly depends on the measuring system since every spectrum analyzer or EMI receiver has a certain reception channel, that is the resolution bandwidth (RBW) which depends on the considered frequency range and the used detectors [8], [9], [11].

The third key parameter is the modulation signal itself that defines the way how the frequency f_c is varied over time. As it has a direct impact on the Bessel functions [8] that are used to decribe the frequency modulated signals, the shape of the envelope in the frequency domain can be influenced in a profitable manner.

Apart from the conventional profiles (e.g. sine, triangular, sawtooth), the use of the so-called Hershey-Kiss^{TM}modulation profile [12], [13], [14], should lead to the flattest top of the spectrum outline, which is a triangular modulation scheme with the extension of a cubic term.

2.4 Summary of Selected Literature

The table below lists literature only relevant to the spread spectrum technique.

		Spread Spectrum Variable		
		PWM frequency	Pulse Position	PWM Carrier
Non-deterministic	Random	[4]	[4],[7]	
	Random assortment	[7]	[3],[6]	[3],[6],[7]
Deterministic	FM	[8],[9],[10],[11]		

Table 2.1: Summary of the covered contents

Chapter 3

Theoretical Fundamentals

In order to understand the methodical steps derivated in chapter 5 the most important theoretical fundamentals are explained in this chapter. To show the PWM strategies in DC to AC converters used in electric drive systems, the theory of space vector modulation is shown in section 3.1. The basics for spectral analysis are explained in section 3.2. On the one hand, this will be necessary for developing a model for the EMI measuring receiver in chapter 5.2 and, on the other hand, to become familiar with the impact of the signal parameters on the frequency spectrum illustrated in section 3.2.1.

3.1 Control Signals in the DC to AC Converter

As a part of the drive system's field-oriented control technique the space vector modulation block generates the control signals for the DC to AC converter's power semiconductors from a given voltage space vector. To elucidate the principle of space vector modulation, the basic structure of a 3-phase pulse inverter is shown in figure 3.1(a). In an idealized consideration the switches of the three halfbridges perform opposing switching transitions which are represented by the namings, e.g. $S1$ for the highside switch and $\overline{S1}$ for the lowside switch of the first halfbridge. Therefore, it is sufficient to define the states of the inverter by defining only the states of the highside switches, that corresponds to the states {S1 S2 S3} illustrated in figure 3.1(b). It shows that the OFF state is declared with "0" and the ON state is declared with "1". The relation between a highside switch's ON state and the PWM period of a signal is denoted by the duty cycle d, see equation 3.1.

$$d = \frac{t_{ON}}{T} = \frac{t_{ON}}{t_{ON} + t_{OFF}} \tag{3.1}$$

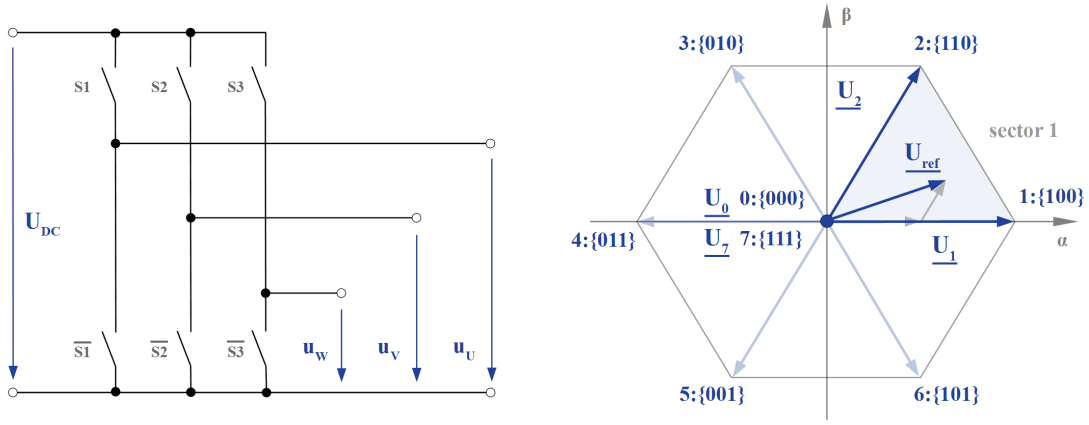

(a) Structure of a 3-phase pulse inverter

(b) Spacevector composition in a 3-phase pulse inverter

Figure 3.1: Principle of space vector modulation

The voltage vectors that can be formed by the eight different states of the 3-phase PWM inverter form the hexagon shown in figure 3.1(b). A desired space vector $\underline{U_{ref}}$ is approximated as a weighted average in time of the four adjacent voltage vectors. The triangular sectors are defined by the two adjacent active voltage vectors and the zero vectors $\underline{U_0}$ {111} and $\underline{U_7}$ {000}. Each of the four switching states according to the four adjacent voltage vectors is applied for a certain time summing up for the PWM period T (equation 3.3). The mathematical representation of the weighted average in time for sector 1 is given in equation 3.3.

$$T = t_1 + t_2 + t_0 + t_7 \tag{3.2}$$

$$\underline{U_{ref}} = (t_1 \cdot \underline{U_1} + t_2 \cdot \underline{U_2} + t_0 \cdot \underline{U_0} + t_7 \cdot \underline{U_7}) \frac{1}{T} \tag{3.3}$$

To add dynamic behavior as used in a 3-phase DC to AC inverter, the representation of a voltage space vector which yields sinusoidal phase voltages in a symmetric system with constant frequency is shown in equation 3.4. There, the angular velocity ω_{el} of the space vector complies with the angular velocity of the generated rotating field in an AC machine.

$$\underline{U_{ref}} = \left|\underline{U_{ref}}\right| \cdot e^{-\omega_{el} \cdot t} \tag{3.4}$$

The magnitude of the space vector corresponds to the degree of modulation, or modulation index m_i that defines the attainable fundamental peak values of the phase voltages u_p (u_U,u_V,u_W) and the phase-to-phase voltages u_{pp} (u_{UV},u_{VW},u_{WU}), see equation 3.5 [15].
$\hat{\underline{u}}_p^{<1>}$ and $\hat{\underline{u}}_{pp}^{<1>}$ denote the peak values of the fundamentals of the averaged voltages u_p and u_{pp} over one PWM cycle.

In the interval for $m_i = [0\ 1]$, also called linear modulation range, the space vector is located within or on the incircle of the hexagon in figure 3.1(b). The maximum value for the fundamental of the phase-to-phase voltage u_{pp} can be achieved by choosing the modulation index to be $m_i = 1$ where the space vector is guided along the incircle. Values between $m_i =]1\ \frac{2\sqrt{3}}{\pi}[$ define the overmodulation range. The modulation range for $m_i \geq \frac{2\sqrt{3}}{\pi}$ is called 6-step mode in which the voltage space vector jumps through the consecutive states.

$$m_i = \frac{\hat{\underline{u}}_{pp}^{<1>}}{U_{DC}} = \frac{\sqrt{3} \cdot \hat{\underline{u}}_{p}^{<1>}}{U_{DC}} \tag{3.5}$$

The relation between the PWM Period T and the fundamental frequency ω_{el} of the space vector defines the frequency modulation index m_f (see equation 3.6). As this thesis deals with two fundamentally different types of modulations which are the SVM and the FM utilized in deterministic spread spectrum techniques, it is worth noting that the frequency modulation index m_f is a different parameter than the spread spectrum modulation frequency f_m.

$$m_f = \frac{f_{pwm}}{f_{el}} = \frac{2\pi}{T \cdot \omega_{el}} \tag{3.6}$$

In the considered system, the zero vector times in equation 3.3 were evenly divided to $t_0 = t_7$ utilizing a center aligned PWM strategy. Therefore, a special state of the inverter is accomplished if the modulation index is set to $m_i = 0$, in which all three halfbridges perform in phase at a constant duty cycle of $d = 0.5$. As a result the attained magnitude of voltage space vector $\left|\underline{U}_{ref}\right|$ is zero.

Another arbitrary state in the linear modulation range is analyzed at $m_i = 0.7$ that leads to phase-to-phase voltages u_{pp} different from zero corresponding to the difference between the duty cycles of the involved halfbridges which deviate from zero as well.

Figure 3.2 shows the relation between modulation index m_i, duty cycles of the highside switches d_p and the phase voltages u_p for a quasi steady state of a 3-phase inverter at which ω_{el} and $\left|\underline{U}_{ref}\right|$ are constant. The angular frequency was set to $\omega_{el} = 2\pi \cdot 1000\ s^{-1}$ which, together with a PWM frequency of $f_{pwm} = 20kHz$, result in a frequency modulation index of $m_f = 20$.

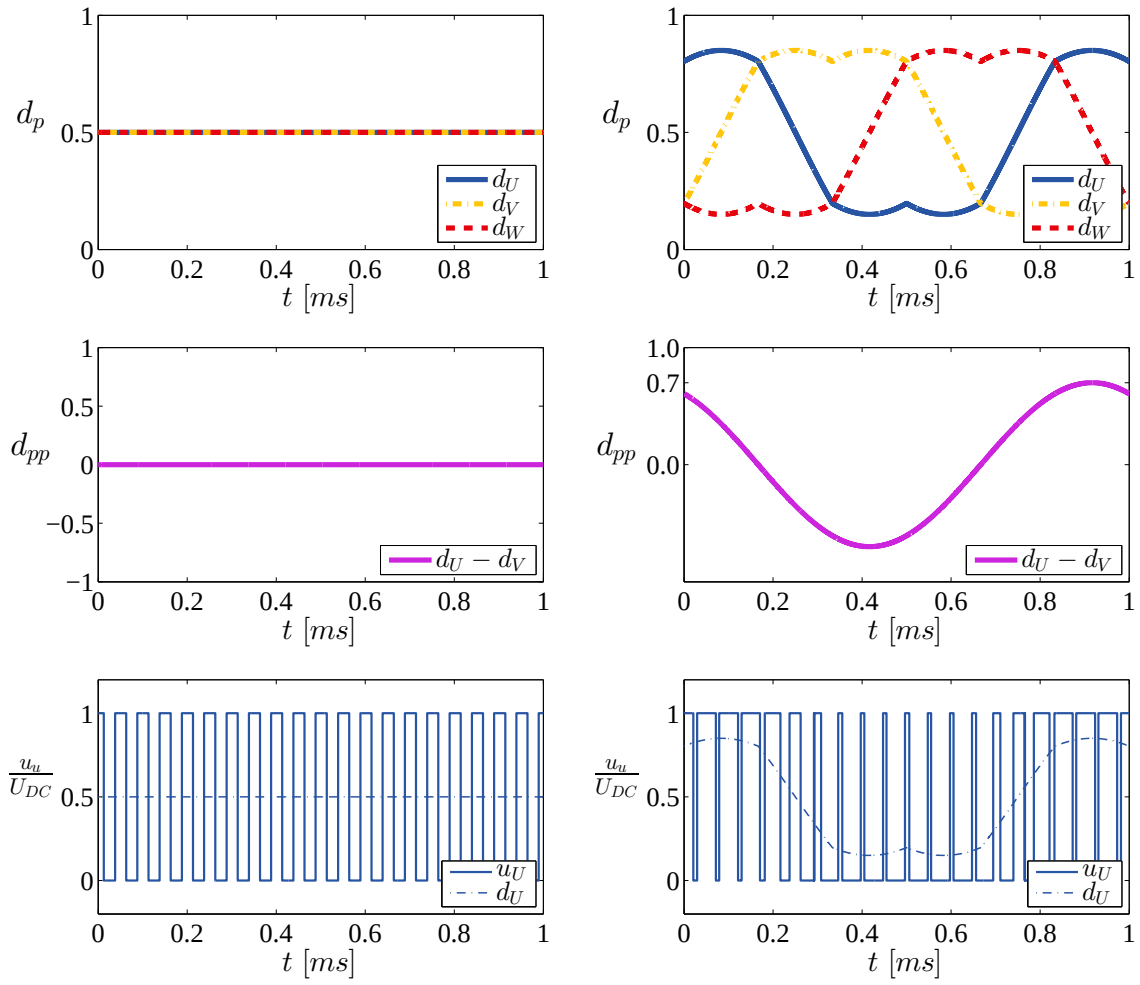

Figure 3.2: Modulation index $m_i = 0$ (left) and $m_i = 0.7$ (right)

3.2 Methods for Spectral Analysis

There are various mathematical methods for different types of application to analyze signals in the frequency domain For the evaluation of electromagnetic emissions by simulation, the behavior of the EMI measuring receiver can be modeled by using the Discrete Fourier Transform (DFT) or the Short-Time Discrete Fourier Transform (STDFT) as will be discussed in chapter 5.2. Due to the discretization in time, these methods are well applicable in practical measurements or simulations. However, there is the problem of not reflecting the real frequency spectrum. Moreover, this section also presents an analytic method for the calculation of the real Fourier coefficients to obtain a better understanding of the impact of the signal parameters specially for trapezoidal PWM signals.

3.2.1 Analytic Calculation of the Fourier Spectrum

As we will see later in chapter 5.1.4, a common source of electromagnetic emissions are PWM signals. For this reason a good understandig of the PWM signal parameters and their effect on the frequency spectrum is necessary. Figure 3.3 shows a trapezoidal PWM signal with the period T, the rise- and fall time t_r and t_f and the pulse duration τ which is defined by the intersection points at $\frac{A}{2}$ with A being the amplitude of the PWM signal.

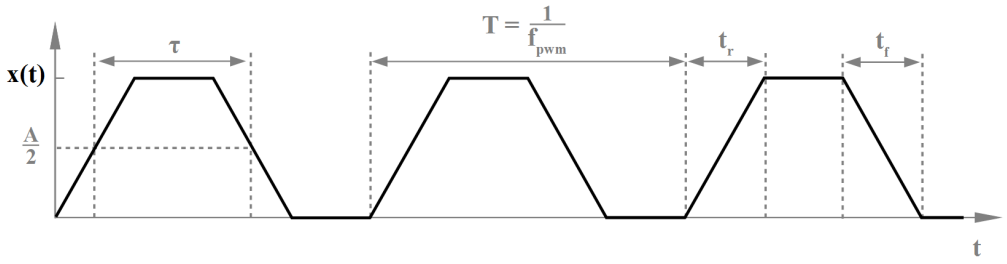

Figure 3.3: Signal parameters for a trapezoidal PWM signal

The general Fourier series representation of a continuous-time signal $x(t)$ is defined by equation 3.7.

$$x(t) = \frac{a_0}{2} + \sum_{n=1}^{\infty} a_n \cdot cos(nt) + b_n \cdot sin(nt) \tag{3.7}$$

A suitable analytic method to calculate the Fourier coefficents a_n and b_n for space vector PWM signals is derived in [16]. The basic concept of this method is that the Fourier coefficients of periodic functions can be obtained by evaluating the function's discontinuities or jumps j and the function derivatives' jumps j', as illustrated in figure 3.4 and in equations 3.8 and 3.9. The line spectrum $\hat{X}(f)$ can then be computed with equation 3.10. There, T_1 is the fundamental period of the considered signal which is defined by the angular velocity ω_{el} of the space vector in this case.

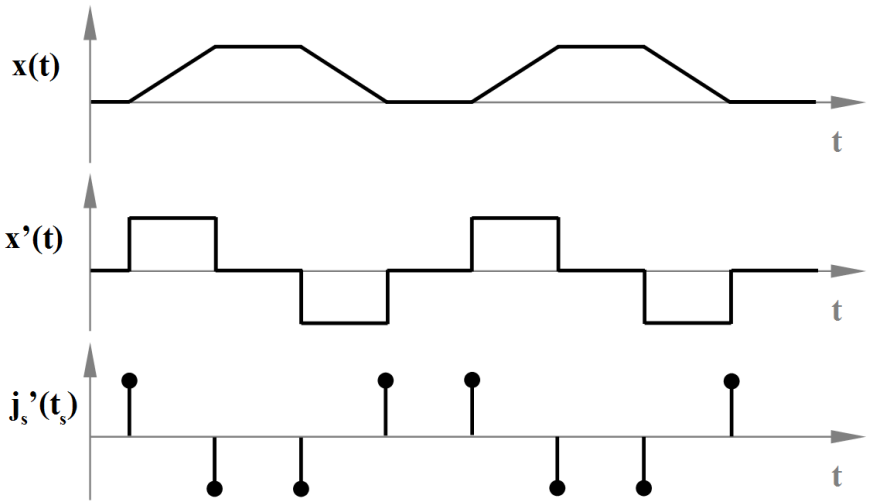

Figure 3.4: Illustration for calculating the fourier coefficients in equation 3.8 and 3.9

$$a_n = \frac{1}{n\pi}[-\sum_{s=1}^{m} j_s \sin(K_n t_s) - \frac{1}{K_n}\sum_{s=1}^{m} j_s' \cos(K_n t_s) + \frac{1}{K_n^2}\sum_{s=1}^{m} j_s'' \sin(K_n t_s) + \frac{1}{K_n^3}\sum_{s=1}^{m} j_s''' \cos(K_n t_s) \quad - \; - \quad + \; + \; ...] \tag{3.8}$$

$$b_n = \frac{1}{n\pi}[\sum_{s=1}^{m} j_s \cos(K_n t_s) - \frac{1}{K_n}\sum_{s=1}^{m} j_s' \sin(K_n t_s) - \frac{1}{K_n^2}\sum_{s=1}^{m} j_s'' \cos(K_n t_s) + \frac{1}{K_n^3}\sum_{s=1}^{m} j_s''' \sin(K_n t_s) \quad + \quad - \; - \quad + \; + \; ...] \tag{3.9}$$

$$\hat{X}(K_n) = |a_n + jb_n| \quad , \quad K_n = n \cdot \frac{2\pi}{T_1} \tag{3.10}$$

The coefficient a_0 respresents the mean value (or DC component) of the signal $x(t)$ over time and can be obtained by integration as it is described in equation 3.11.

$$a_0 = \frac{1}{T}\int_{-\frac{T}{2}}^{+\frac{T}{2}} x(t)dt \tag{3.11}$$

In the following sections, a case analysis is done to become familiar with the effects of the signal parameters τ, tr and t_f on the frequency spectrum. Therefore, the line spectra of the PWM signals in figure 3.2 will be analyzed.

Constant Slew Rate and Constant Pulse Duration

As depicted in 3.2, the special state at which the phase voltages attain a constant pulse duration and thereby a constant duty cycle ($d = 0.5$) can be achieved by choosing the modulation index to $m_i = 0$.

The corresponding frequency response is depicted in figure 3.5, in which the signal parameters are chosen to $A = 1$, $f_{pwm} = 20kHz$, $t_r = t_f = 200ns$ and $\tau = 5\mu s$ that complies with a duty cycle of (approximately) $d = 0.5$.

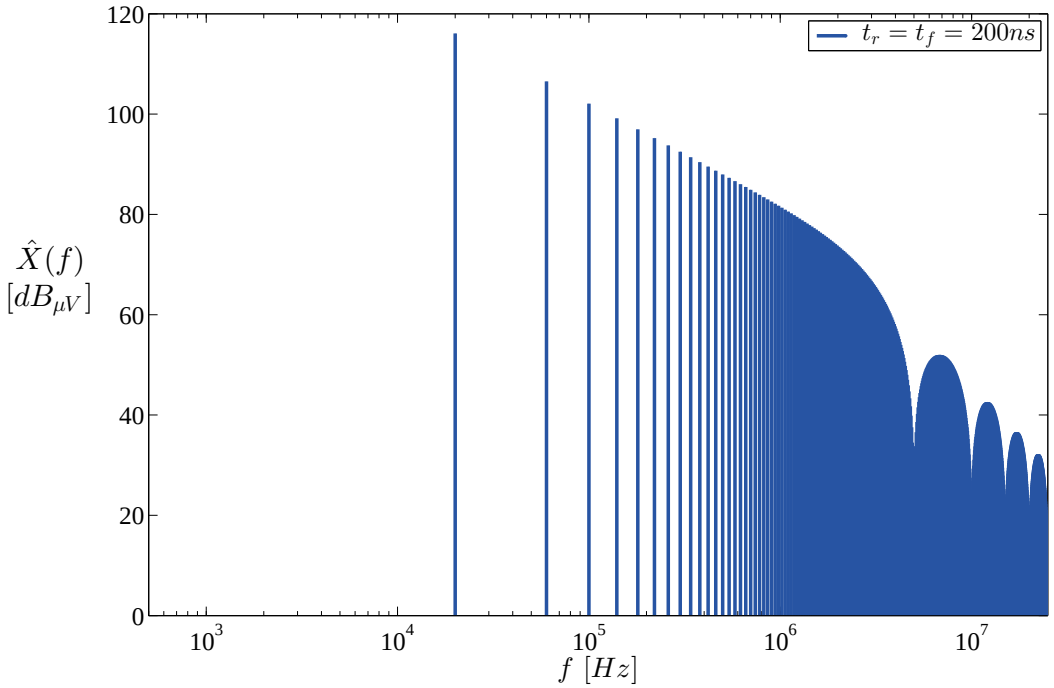

Figure 3.5: Line spectrum of a spacevector PWM signal with modulation index $m_i = 0$ ($d = 0.5$)

Considering figure 3.5, it becomes apparent that only odd harmonics are present in the line spectrum. This lies in the fact that the coefficients a_n are all zero in symmetric functions and b_n is zero for even n.

In [17], an analytic method for calculating the line spectra of trapezoidal signals with equal rise- and fall times $t_r = t_f =$ is presented (equation 3.12).

$$\hat{X}(nf_{pwm}) = 2\,A\,f_{pwm}\,\tau \left|\frac{sin(\pi\,\tau\,n\,f_{pwm})}{\pi\,\tau\,n\,f_{pwm}}\right| \left|\frac{sin(\pi\,t_r\,n\,f_{pwm})}{\pi\,t_r\,n\,f_{pwm}}\right| \quad , \quad n = 1, 2, 3, \ldots \tag{3.12}$$

Applying the logarithm to equation 3.12 leads to a subdivision of the line spectrum into three sections. The horizontal section of the line spectrum's envelope is defined by the the signal frequency f_{pwm} and the pulse duration τ. The second section results from the pulse duration τ, where the envelope of the line spectrum drops with $-20dB\mu V$ per decade. The third section is determined by the rise and fall time $t_r = t_f$, where the envelope declines with $-40dB\mu V$ per decade. The associated corner frequencies f_{c1} and f_{c2} are specified in equation 3.13.

$$f_{c1} = \frac{1}{\pi\,\tau} \quad , \quad f_{c2} = \frac{1}{\pi\,t_r} \tag{3.13}$$

Constant Slew Rate and Varying Pulse Duration

Regarding figure 3.2, for constant modulation indices different from zero, the half bridge duty cycles d_p will yield to varying pulse durations over time.

Figure 3.6 shows the Fourier line spectrum for a space vector PWM signal with a modulation index of $m_i = 0.7$, where the angular frequency of the voltage space vector was chosen to be $\omega_{el} = 2\pi \cdot 1000\,s^{-1}$ (see figure 3.2). The rise and fall times of the signal was set to $t_r = t_f = 200ns$.

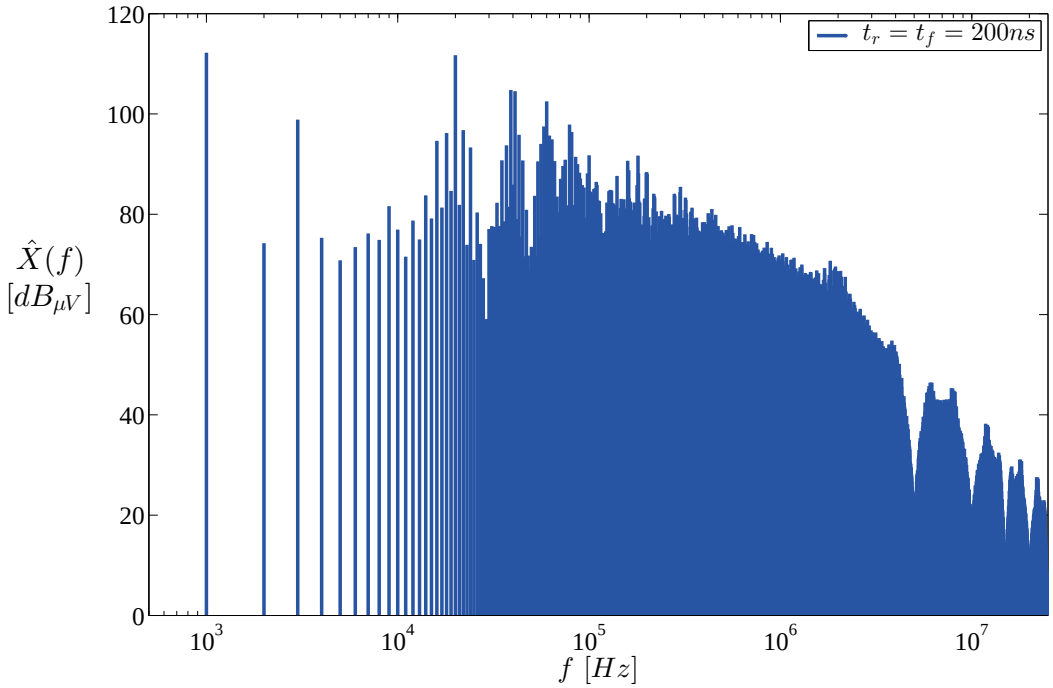

Figure 3.6: Line spectrum of a spacevector PWM signal with modulation index $m_i = 0.7$

Comparing figure 3.5 and 3.6, the fundamental frequency of the space vector at $1kHz$ and its third order harmonic appear in the Fourier spectrum. The corner frequency f_{g2} stays almost unchanged since the rise and fall times in both cases were set equally to $t_r = t_f = 200ns$.

Varying Slew Rate and Varying Pulse Duration

In general, the slew rates of the phase voltages on the half bridge outputs will not be constant within the fundamental period of ω_{el} in real applications. This, for example, can be explained by the charging and discharging processes of the output capacitances of the used power semiconductors, as they depend on the current flowing into or out of the half bridge. To elucidate this effect, a time variable slew rate was added to the signal analyzed in 3.2.1 that varies sinusoidally and in phase with the fundamental of the PWM voltage signal (see figure 3.7).

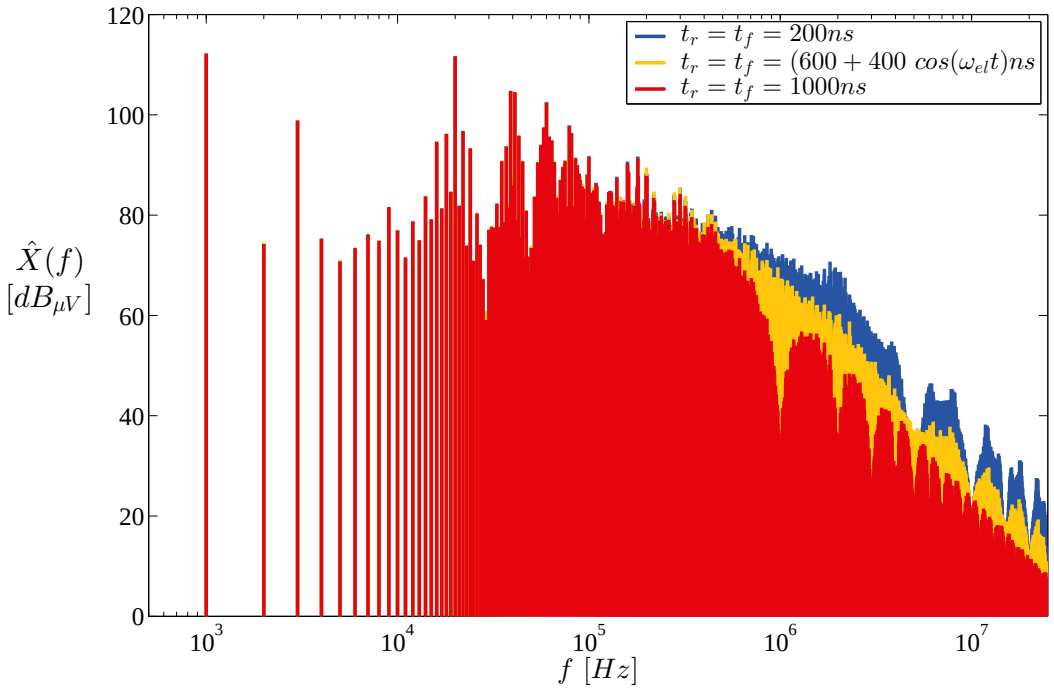

Figure 3.7: Variable rise and fall times, $t_r = t_f = (600 + 400 \cdot cos(\omega_{el}t))\mu s$

If now the line spectrum in 3.7 is considered, the effect of a varying slew rate can be interpreted as a mixture of the line spectra of the occuring maximum and minimum values for the rise and fall times $t_r = t_f = 200ns$ and $t_r = t_f = 1000ns$.

Influence of the Frequency Modulation Index m_f

To illustrate the impact of the frequency modulation index, the Fourier spectrum was calculated for the values m_f = 400, 100 and 20 which correspond to the fundamental frequencies f_{el} = 50Hz, 200Hz and 1000Hz of the voltage space vector at a constant PWM frequency of f_{pwm} = 20kHz according to equation 3.6. The modulation index was set to m_i = 0.7 and the rise and fall times to $t_r = t_f$ = 200ns.

Considering figure 3.8 it becomes apparent that on the one hand, the frequency modulation index m_f determines the distance between the sideband harmonics. On the other hand, the harmonic's bandwidth expands with increasing harmonic order which becomes clearly evident at higher modulation indices.

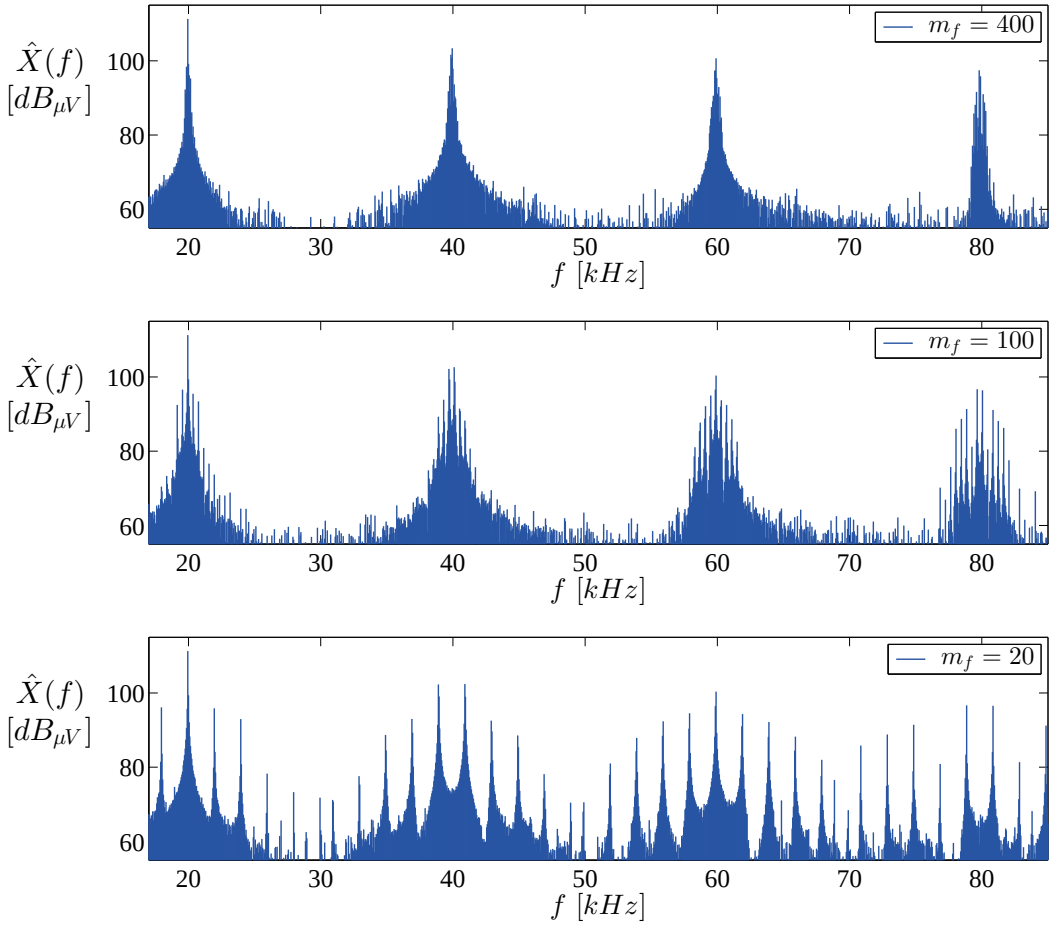

Figure 3.8: Impact of the frequency modulation index m_f on the Fourier spectrum

3.2.2 Numeric Spectral Analysis Methods

In practical measurements as well as in computational simulations, signal analysis deals with signals with a generally unknown composition of spectral components, in which analytic methods cannot be applied anymore. For this reason two different numeric analytical methods are presented. On the one hand, the Discrete Fourier Transform is destined for stationary signals. The Short Time Discrete Fourier Transform, on the other hand, is well suited for non-stationary signals which change their properties over time.

The Discrete Fourier Transform

With the Fourier Transform, continuous-time signals with infinite duration can be transformed into the frequency domain and result in a continuous Fourier spectrum [18], see equation 3.14.

$$X(\omega) = \int_{-\infty}^{\infty} x(t) \cdot e^{-j \cdot \omega \cdot t} \, dt \tag{3.14}$$

Since only discrete-time signals with finite duration can be processed in computational simulations, the DFT can be used to calculate an approximated version of the FT [18]. The structure of the DFT implementation and the discretization of a continuous-time signal are depicted in figures 3.9(a) and 3.9(b). A continuous-time signal $x(t)$ is discretized by the sampling time T_S to the signal $x[n]$. To limit the signal $x[n]$, an N-point sample is taken by multipliplying $x[n]$ with a window function $w[n]$ of the length T_W or N which can be interpreted as the observation length of the DFT.

The distance between the frequency bins in the discrete spectrum $V[k]$ is defined by the window length N and is also referred to as the frequency resolution Δf of the DFT, see 3.15.

$$\Delta f = \frac{\Delta \omega}{2\pi} = \frac{1}{N \cdot T_S} = \frac{1}{T_W} \tag{3.15}$$

The mathematical description of this procedure is provided in equation 3.16 [18]. A characteristic property of the DFT is the periodic assumption of the N-point sample with the period N, which in general leads to discontinuities in time and to spectral leakage (leakage effect) as described later.

$$\begin{aligned} x[n] &\approx x(n \cdot T_S) \\ v[n] &= x[n] \cdot w[n] \end{aligned}$$

$$V[k] = \sum_{n=0}^{N-1} v[n] \cdot e^{-j \cdot \frac{2\pi}{N} \cdot k \cdot n} \tag{3.16}$$

Considering the frequency responses $W(\omega)$ of a rectangular window and a Gaussian window in figure 3.10, the rectangular window provides the best distinction between two adjacent spectral components due to its narrow main lobe.

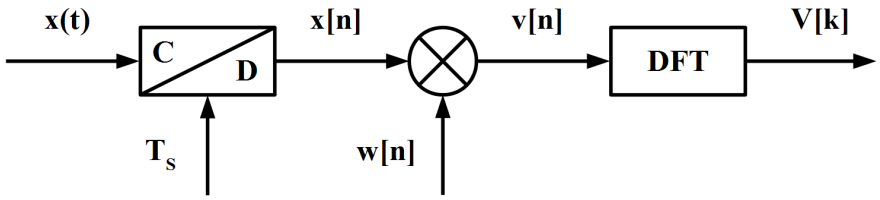

(a) DFT structure

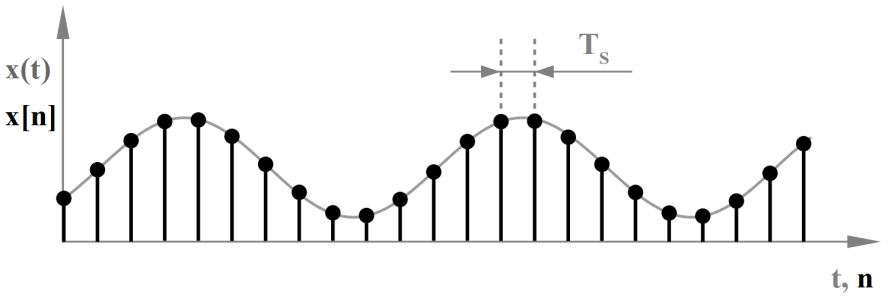

(b) Discretization of a continuous time signal

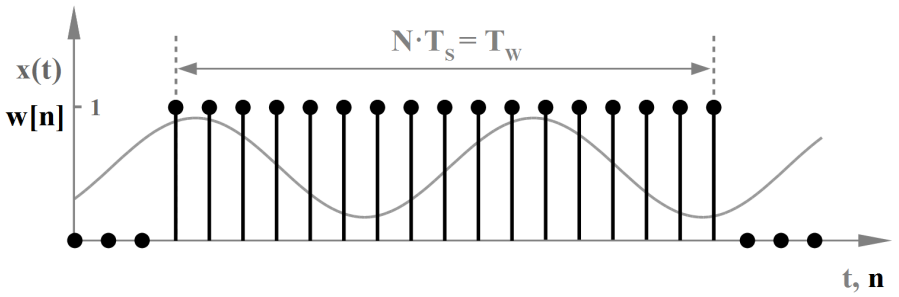

(c) Application of a rectangular window

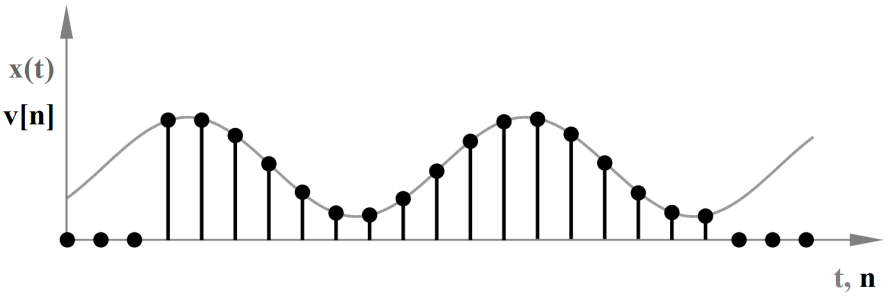

(d) Windowed signal

Figure 3.9: Calculation principle for the N-point DFT

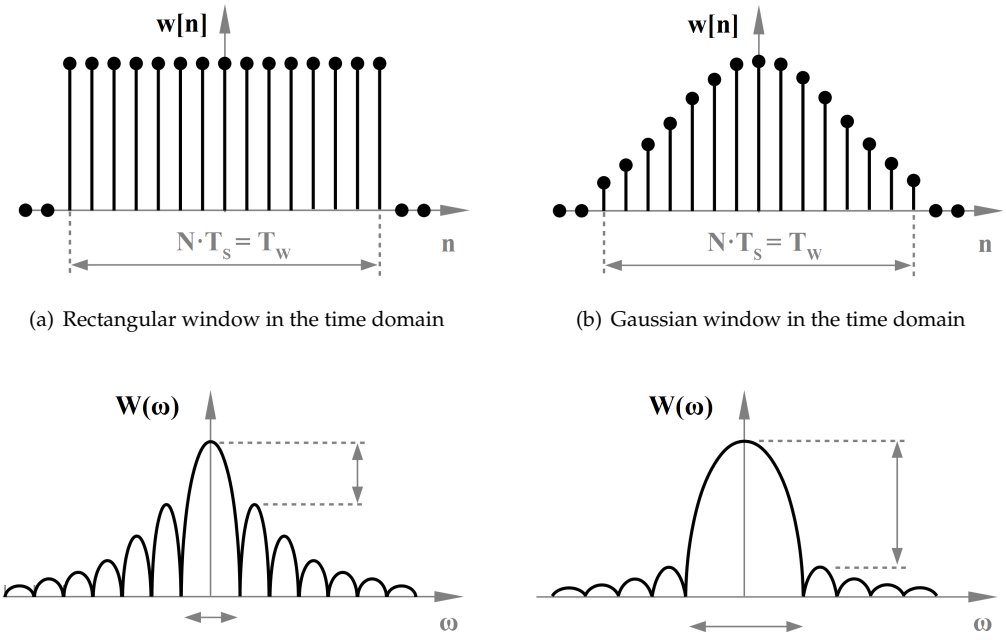

(a) Rectangular window in the time domain

(b) Gaussian window in the time domain

(c) Rectangular window in the frequency domain

(d) Gaussian window in the frequency domain

Figure 3.10: Frequency response of a rectangular and a gaussian window

Applying a window function $w[n]$ to a signal $x[n]$ is equal to a multiplication of $w[n]$ and $x[n]$ in the time domain that corresponds with a convolution of the frequency responses $W(\omega)$ and $X(\omega)$ in the frequency domain. Hence, the frequency response of the window function gets shifted by a sinusoidal signal by its frequency. This property is known as the so-called *Modulation Theorem*.

For example, the application of a rectangular window to a sinusoidal signal where the DFT observation time T_W is different from the signal period (or multiples of the signal period) results in a high leakage of the frequency bins over the spectrum. This is due to the high side lobes of the rectangular window as shown in 3.11(a).

This effect can be suppressed by using a suitable window function in which the discontinuities of the observed signal are less weighted. Figure 3.11(b) illustrates the reduction of the leakage effect by using a Gaussian window which has smaller side lobes than the rectangular window.

Synchronous sampling is a special case in which the window length N coincides with multiples of the signal period. For the rectangular window there does not occur any leakage, since the signal frequency matches with a certain frequency bin of the DFT, see figure 3.11(c). However, the DFT for a synchronous sampled signal with a Gaussian window stays almost unchanged.

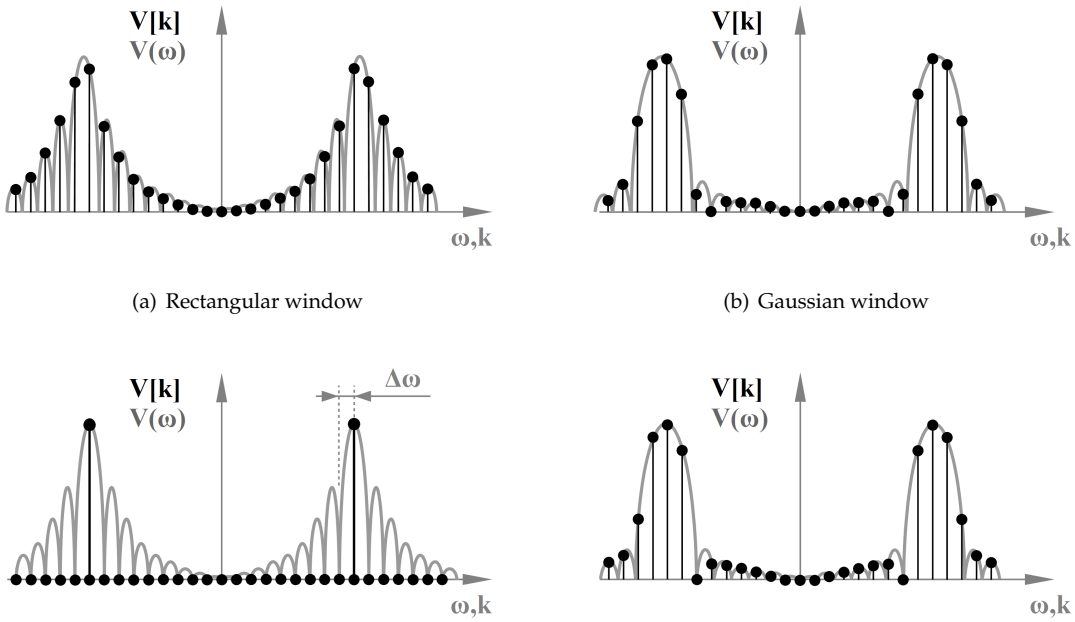

(a) Rectangular window

(b) Gaussian window

(c) Rectangular window, synchronous sampling

(d) Gaussian window, synchronous sampling

Figure 3.11: Principle of windowing and spectral leakage

The Short Time Discrete Fourier Transform

Unlike the DFT, the result of the STDFT provides information about the discrete-time n in addition to the disrete frequency k. This makes the STDFT well suitable to analyse nonstationary signals that change their behavior over time. A possible calculation method of the STDFT is shown in 3.17 [19], where the signal of interest is again $x[n]$ and the window function is $w[n]$ with the length L and the DFT length N.

$$X[n,k] = \sum_{m=0}^{L-1} x[m+n] \cdot w[m] \cdot e^{-j \cdot \frac{2\pi}{N} \cdot k \cdot m} \tag{3.17}$$

To gain a better understanding of equation 3.17, equation 3.18 can be derived by substituting the term $m + n$ with m'. Due to the modulation theorem, the term $h_\omega[m' - n]$ can be interpreted as a modulated window that slides along the frequency response $X[k]$ of $x[n]$. This explanation will be of great interest for the modeling of the superheterodyne principle used in swept-tuned spectrum analyzers as well as in EMI measuring receivers in chapter 5.2.

$$
\begin{aligned}
X[n,k] &= \sum_{m=0}^{L-1} x[m+n] \cdot w[m] \cdot e^{-j \cdot \frac{2\pi}{N} \cdot k \cdot m} \\
&= \sum_{m'=0}^{L-1} x[m'] \cdot \underbrace{w[m'-n] \cdot e^{-j \cdot \frac{2\pi}{N} \cdot k \cdot (m'-n)}}_{\mathrm{h}_\omega[\mathrm{m'-n}]}
\end{aligned} \tag{3.18}
$$

Similar to the DFT, the frequency resolution results from the DFT length N as explained in 3.2.2. According to equation 3.18, the signal to be analyzed is evaluated by overlapping window functions in time. Hence, the windowed time segments have a certain degree of correlation depending on the chosen window function and subsequently lead to a limited resolution in time as well. As a consequence, both frequency resolution and time resolution are only defined by the window function. This leads to the dilemma that one parameter can only be optimized at the expense of the other which is also referred to as the *uncertainty principle*. For example, when utilizing a rectangular window function, a high frequency resolution can be achieved by applying a long window, conversely a high time resolution by a short window. In general, the product of the time- and frequency resolution spans a region in the frequency-time range which is called *Heisenberg Box* and can be minimized by using a Gaussian window [19] and is also known as the *Gabor Transformation*.

Chapter 4

Spectral Analysis of Different Spread Spectrum Approaches

In this chapter, the effects of the most promising spread spectrum techniques applied to a space vector PWM signal are analyzed in the frequency domain by using the spectral analysis method presented in 3.2.1.

The analyzed space vector PWM signal is equivalent to the normalized voltage between phase and ground and is defined by a quasi stationary space vector with constant frequency ω_{el} and modulation index m_i as illustrated in figure 3.2. For a clear representation how spread spectrum affects the Fourier spectrum, the frequency modulation index is set to $m_f = 400$ at a PWM frequency of $f_{pwm} = 20kHz$ ($f_{el} = 50Hz$) in order to reduce the distance between the signal's sideband harmonics (see figure 3.8). The modulation index was set to $m_i = 0.7$ and the rise and fall times to $t_r = t_f = 200ns$.

To find the most suitable spread spectrum technique for the considered application, both the deterministic and non-deterministic approaches are investigated in the following sections.

4.1 Non-deterministic Spread Spectrum

In this section two different spread spectrum techniques are analyzed in which the non-deterministic behavior is implemented by a randomized sequence with a uniform distribution function. Thereby, the varied parameters are the pulse position within the PWM period and the period itself, as illustrated in figure 2.1(b) and 2.1(d).

4.1.1 Randomized Pulse Position Spread Spectrum

The randomization of the pulse position is achieved by the variation of the triangular carrier's slope as depicted in figure 4.1(b), where the position can be represented by the parameter β. That means a constant value for $\beta = 0.5$ results in a symmetric or center aligned PWM signal (figure 4.1(a)), whereas value of $\beta = 0$ or $\beta = 1$ yield to (left or right) edge aligned PWM signals. The maximum deviation $\Delta\beta$ from $\beta = 0.5$ then defines the boundaries within the instanteneous pulse position will be randomized and is limited to $\Delta\beta = 0.5$. In figure 4.2, the effect of the randomization of the pulse postion on the Fourier spectrum is shown for different values of β.

Regarding the case of the highest possible variation at $\Delta\beta = 0.5$, a reduction of the fundamental's peak of around $5dB_{\mu V}$ becomes evident, whereby at $\beta = 0.05$ (that corresponds to a variation of the

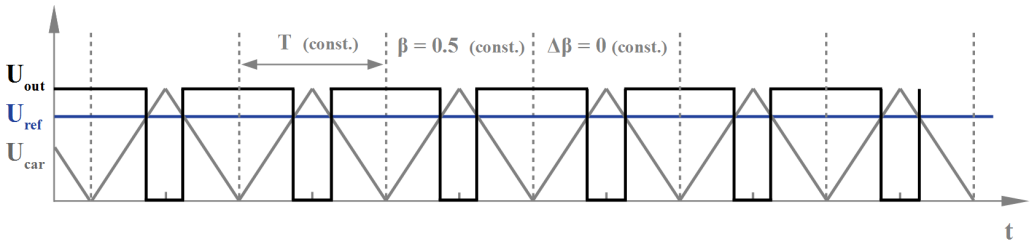

(a) Conventional carrier signal

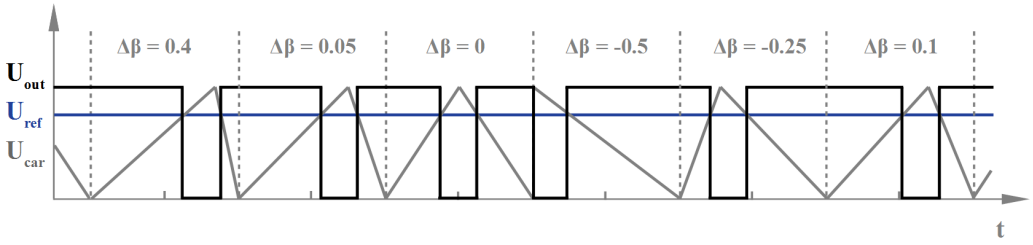

(b) Randomized pulse position concept (RPP)

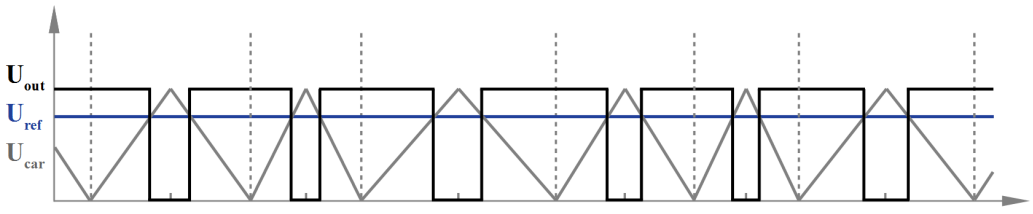

(c) Random carrier frequency concept (RCF)

Figure 4.1: Non-deterministic spread spectrum concepts

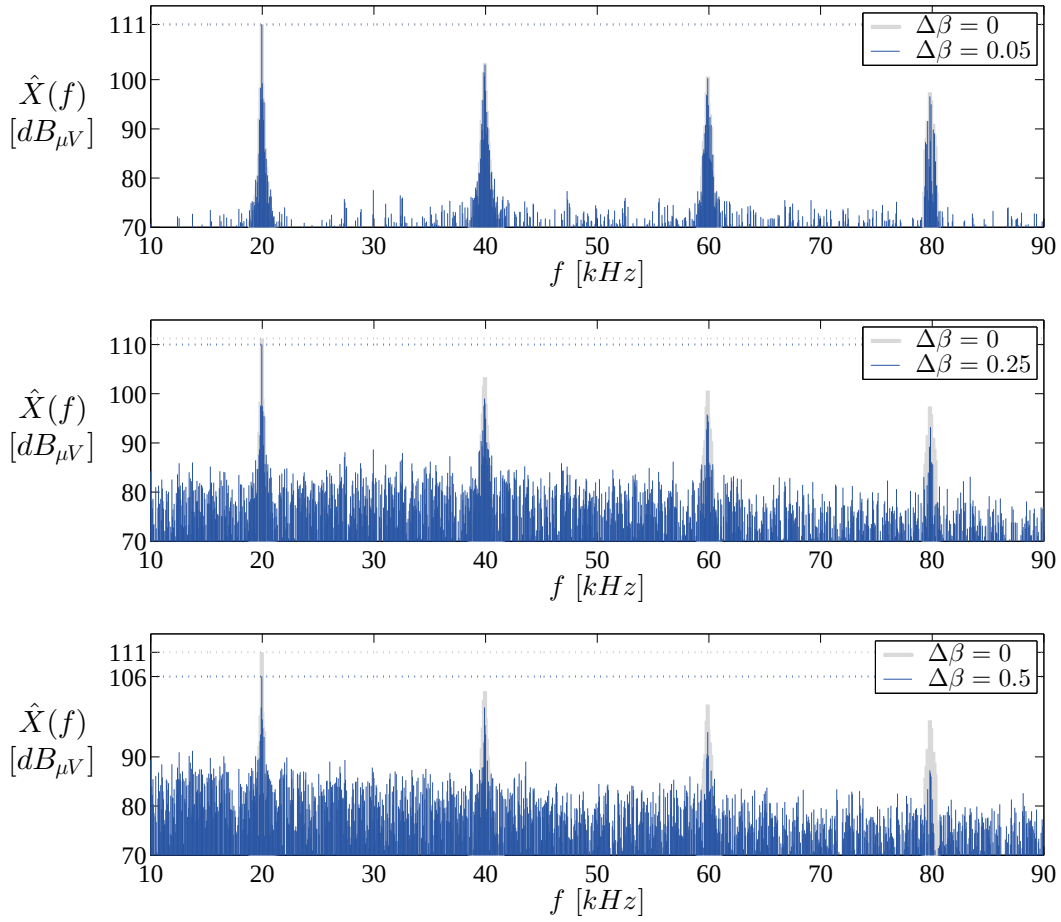

Figure 4.2: Impact of randomized pulse position variation β

pulse postion of 10%) almost no peak reduction can be achieved. Interestingly, the peak value at the fundemental frequency for $\Delta\beta = 0.25$ can be reduced by only $1dB_{\mu V}$, while the reduction at the 3^{rd} harmonic is significantly higher. This effect can be interpreted by the fact that the relative deviation of the pulse position gets higher with the harmonic's order. Furthermore, higher emissions can be observed in the bands between the harmonics.

4.1.2 Randomized Carrier Frequency Spread Spectrum

Similar to the implementation of the ranomized pulse position, the variation range of the carrier frequency f_c around the nominal carrier frequency $f_{c,nom}$ is defined by the highest possible frequency deviation Δf_c. It also has a direct influence on the harmonics' and sideband harmonics' bandwidth and peak value.

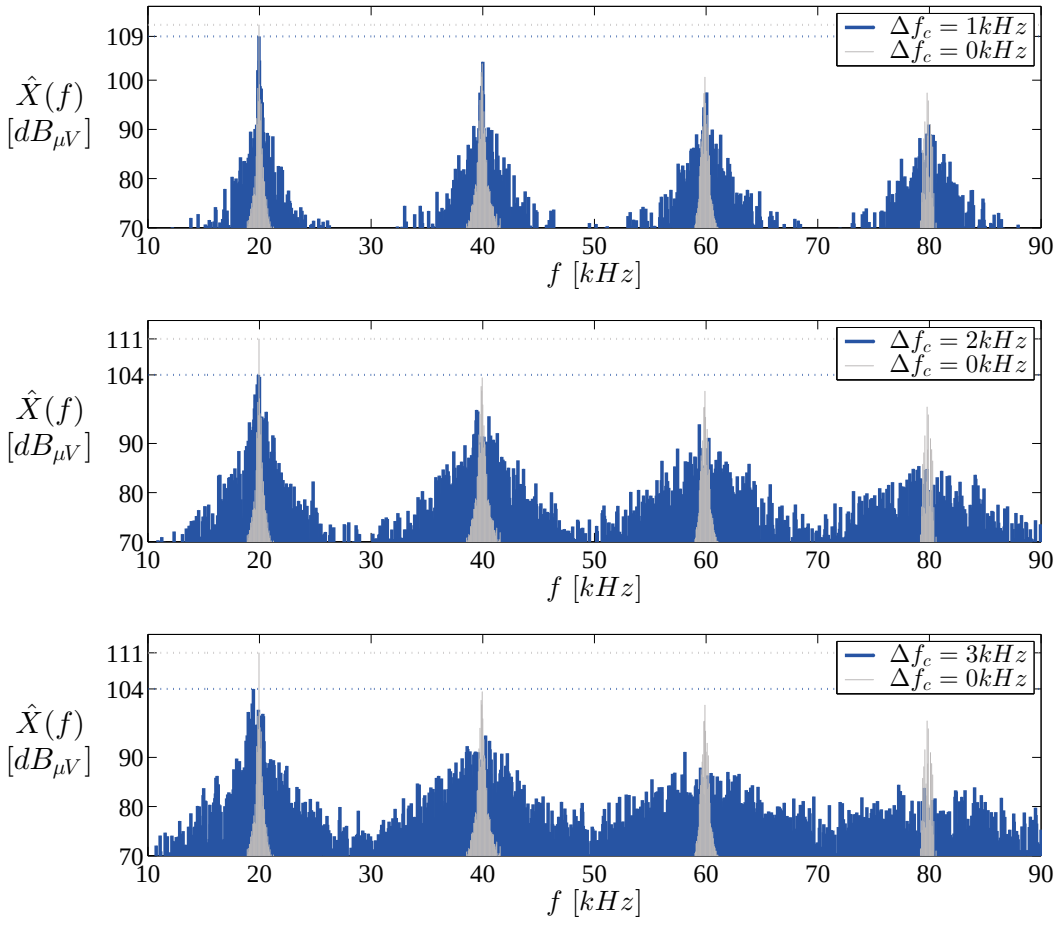

Figure 4.3: Impact of the maximum frequency deviation Δf_c in randomized carrier frequency selection

Figure 4.3 illustrates the effect of the maximum frequency deviation for different values of Δf_c, whereby the value of $\Delta f_c = 0$ means that no spread spectrum is applied to the signal.

Comparing the randomized carrier frequency (RCF) with the randomized pulse postion technique (RPP), the RCF provides a better suppression of the harmonics' peak values by a more evenly distribution of the signal energy.

4.2 Deterministic Spread Spectrum

As could be seen in section 4.1, the application of spread spectrum on the carrier frequency (=PWM period), which is demonstrated in figure 2.1(d), is more promising than the variation of the pulse position, whereby only the former is investigated. Therefore, the key parameters, namely the frequency deviation Δf_c, the modulation frequency f_m and the modulation profile, are varied separately while keeping the other parameters constant in order to gain a better understanding of their impact on the Fourier spectrum.

4.2.1 Influence of the Frequency Deviation Δf_c

As the frequency deviation Δf_c defines the maximum excursion of the carrier frequency $f_c = f_{pwm}$ from the nominal carrier frequency $f_{c,nom}$, it has a direct influence on the signals' harmonics and sideband harmonics' bandwidth and peak value. A symmetric deviation of f_c from $f_{c,nom}$ is shown in figure 4.4(a) and is often referred to as *center-spreading*.

Figure 4.5 illustrates the effect of the frequency deviation for different values of Δf_c at a constant modulation frequency of $f_m = 50Hz$ and a triangular modulation profile (see figure 4.4(a)), whereby the value of $\Delta f_c = 0$ means that no spread spectrum is applied to the signal.

Basically, the harmonic envelopes' peak values will get lower for higher values of Δf_c. However, reminding the fact that the bandwidth of the $n^{th}-$ harmonic and side band harmonics will be enlarged by the factor n (see 3.2.1), the envelopes of the harmonics (and sideband harmonics) start to overlap at a certain frequency depending on the value of Δf_c which leads to a decrease of the emission reduction. This effect becomes apparent between the 2^{nd} and 3^{rd} harmonic at a frequency slightly below 70kHz for a frequency deviation of $\Delta f_c = 3kHz$.

4.2.2 Influence of the Modulation Frequency f_m

The modulation frequency f_m corresponding to the modulation time T_m defines how fast the instantaneous carrier frequency f_c is changed over time, as illustrated in figure 4.4(a). According to the modulation theorem presented in [8] and [20], the application of frequency modulation to a narrow band signal leads to a spreading of the signal's energy over a large bandwidth, where the spectral components occur at fixed frequencies. More specifically, the distance between these components is equal to the value of the modulation frequency f_m, whereby their peak value result from the respective Bessel functions $J_n(\beta)$. A similar effect appears for space vector PWM signals with a frequency modulation index m_f and can be observed by comparing the figures 4.6 and 3.8.

Considering figure 4.6, one would suppose that smaller values for f_m always lead to a higher emission reduction. However, this does not apply during the measurement with spectrum analyzers or EMI measuring receivers as they use different detectors and certain resolution bandwidths (RBW) depending on the frequency range. The utilization of the effect of the modulation frequency with regard to the measuring receivers RBWs and detectors is explained in more detail in chapter 6.

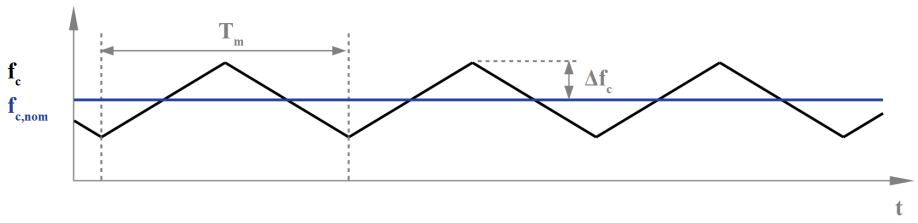

(a) Maximum frequency deviation Δf_c and modulation time T_m

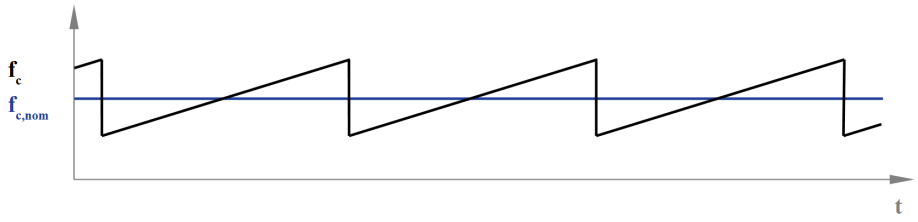

(b) Sawtooth modulation profile (up-ramp)

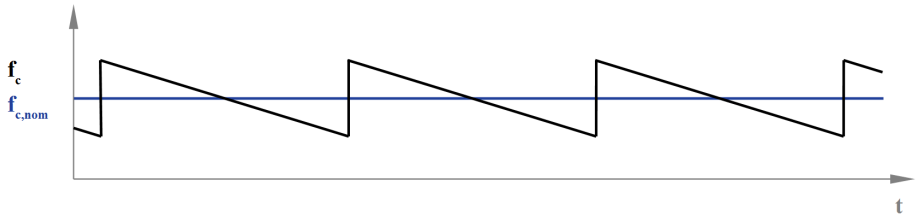

(c) Sawtooth modulation profile (down-ramp)

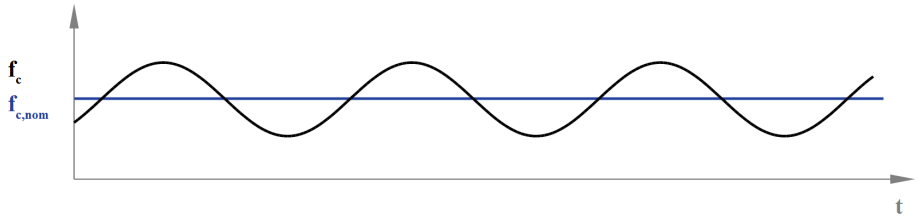

(d) Sinusoidal modulation profile

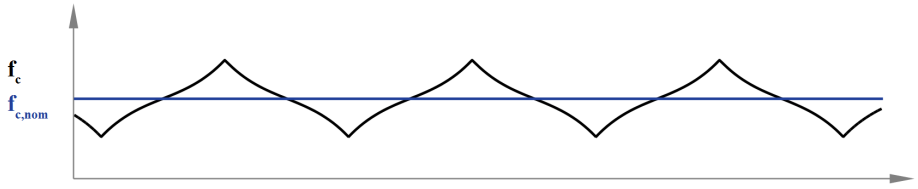

(e) Hershey-Kiss^{TM}modulation profile

Figure 4.4: Deterministic modulation profiles

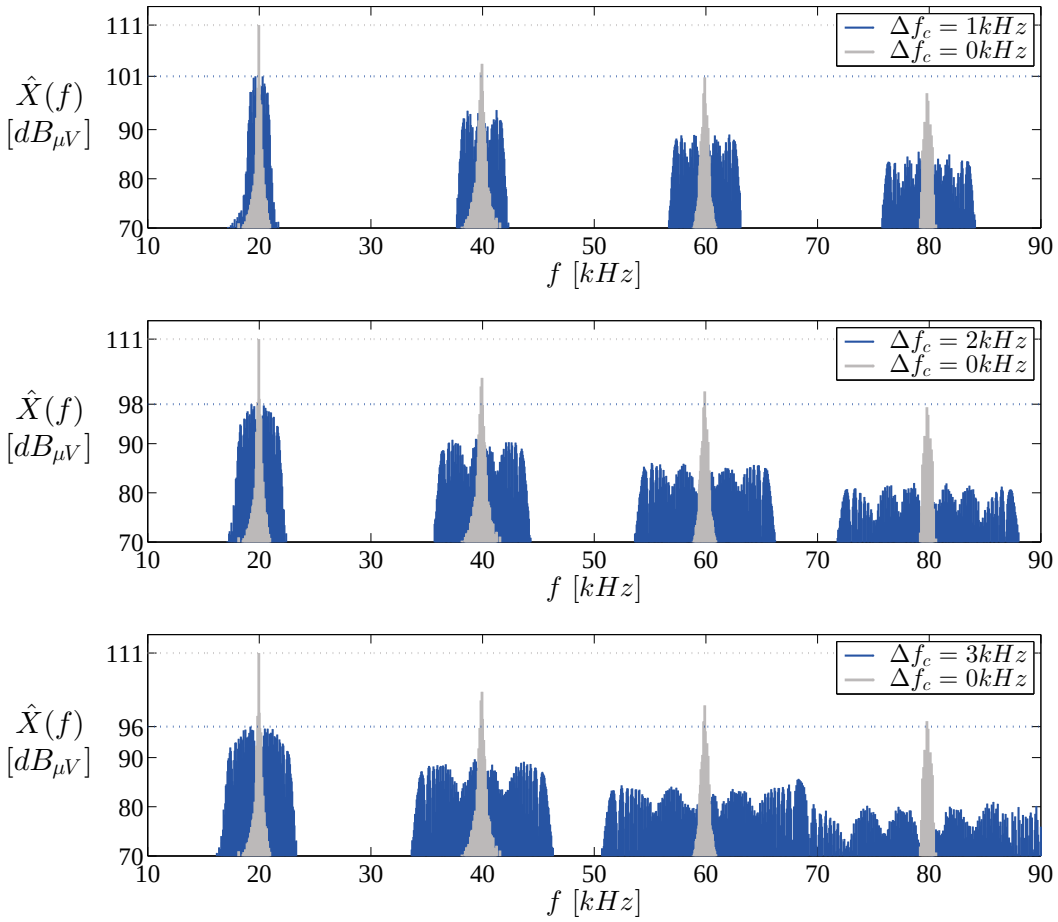

Figure 4.5: Impact of the maximum frequency deviation Δf_c at a modulation frequency of $f_m = 50Hz$ and a triangular modoulation profile

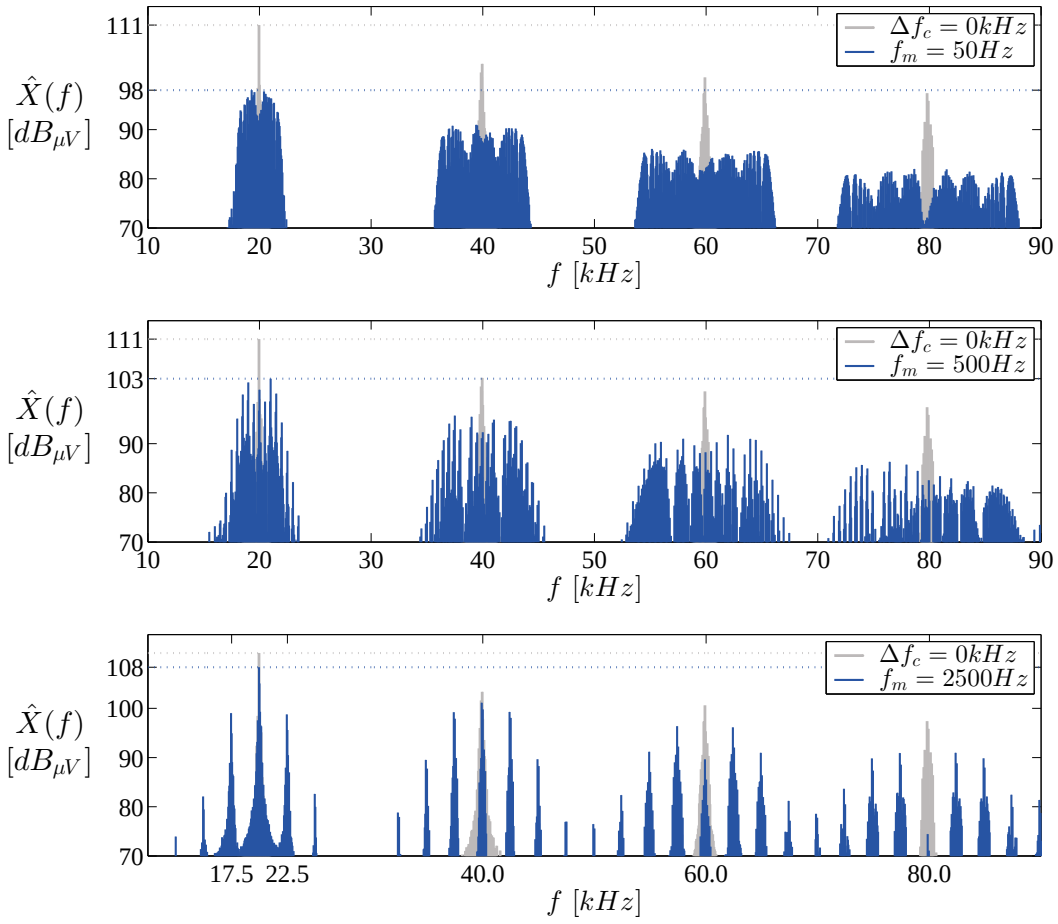

Figure 4.6: Impact of the modulation frequency f_m at a frequency deviation of $\Delta f_c = 2kHz$ and a triangular modulation profile

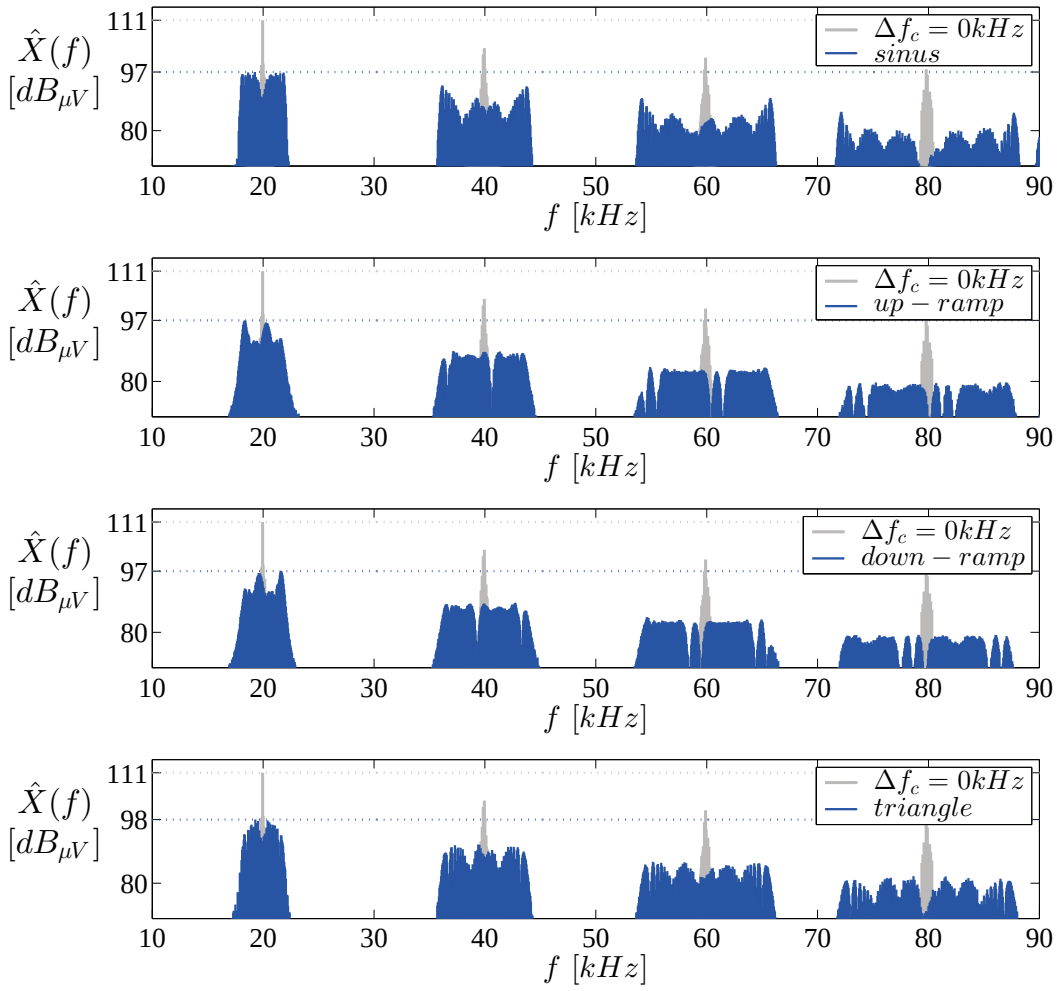

Figure 4.7: Impact of the modulation profile at a frequency deviation of $\Delta f_c = 2kHz$ and a modulation frequency of $f_m = 50Hz$

4.2.3 Influence of the Modulation Profile

The modulation signal defines the way how the frequency f_c is varied over time. This can, for example, be a sine-, a triangular-, a sawtooth or a Hershey-Kiss^{TM}profile, as depicted in figure 4.4.

Compared to the frequency deviation and modulation frequency, the modulation profile has the smallest influence on the emission reduction. Figure 4.7 shows a comparison of the named profiles in the frequency domain. It can be observed that the choice of the used modulation profiles affects the flatness of the harmonics' envelope.

By evaluating the Fourier spectrum over the highest occurring period for the sinusoidal profile which corresponds to the modulation frequency f_m in this case, there will be more PWM cycles at the peak excursions of f_c as the respective gradient of the sinusoidal function reaches a minimum value. This results in remarkable bumps in each harmonic.

The sawtooth- and the triangular modulation profiles, however, lead to a better flatness of the spectrum outline as a result of a uniform distribution of the PWM cylces' instanteneous carrier

frequencies.

According to [12], [13] and [14], the so-called *Hershey – Kiss*^{TM} profile should provide the best flatness of spectrum outline, which follows the equation 4.1.

$$f_c(t) = a \cdot t + b \cdot t^2 \tag{4.1}$$

Figure 4.8 depicts the Fourier spectra for the application of different parameters a and b.

It is noticeable that indeed the *Hershey Kiss* 2 profile in figure 4.8 shows most likely the flattest top of the spectrum's fundamental envelope, but that does not apply for higher order harmonics. The profile *Hershey Kiss* 3, which more or less corresponds to a triangular profile, provides a flat top of higher order harmonics at the same time. Obviously, the *Hershey Kiss*^{TM} profile is probably not the right choice for the application in space vector PWM signals.

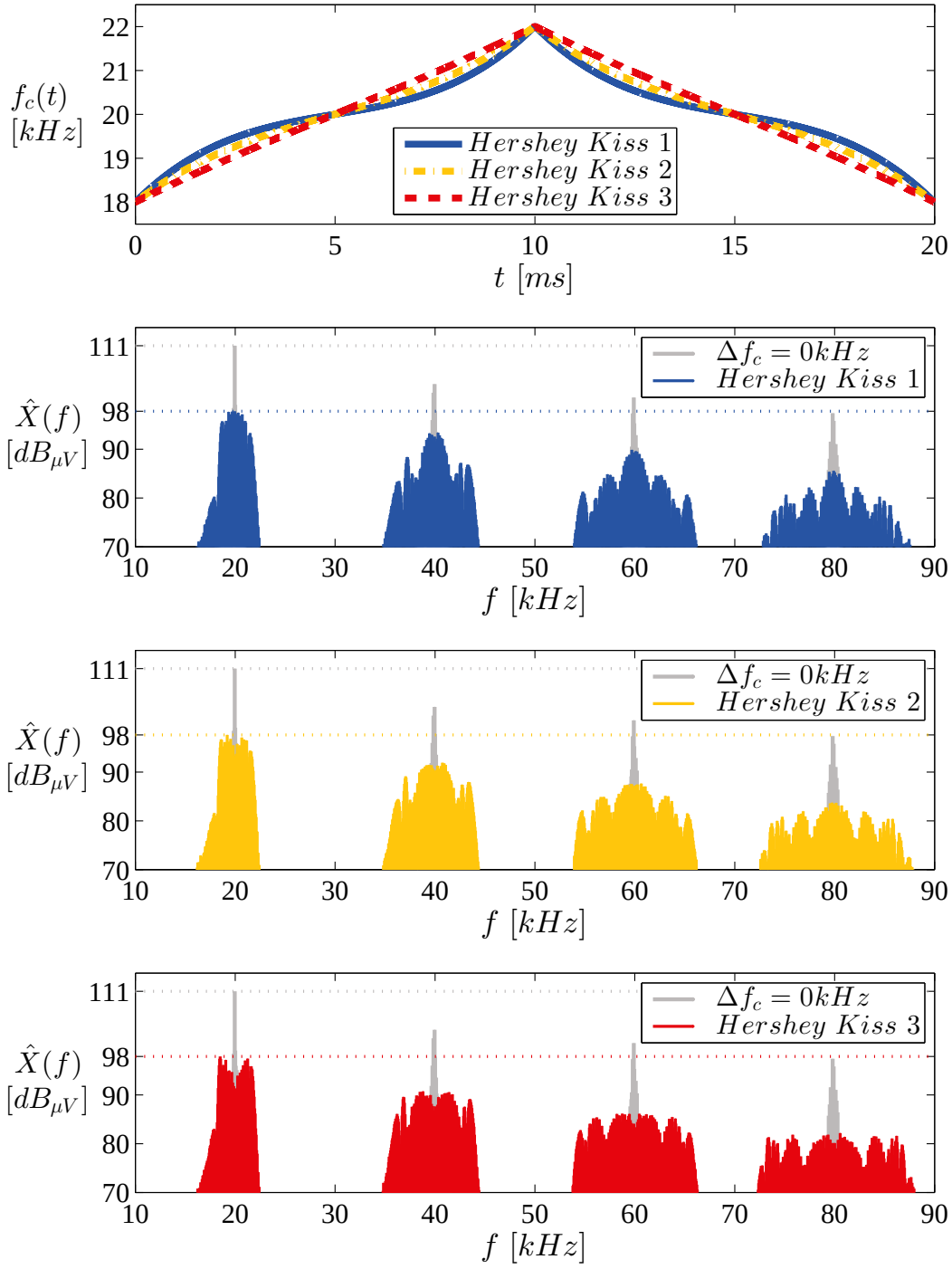

Figure 4.8: Comparison of different *Hershey Kiss*™ modulation profiles at a frequency deviation of $\Delta f_c = 2kHz$ and a modulation frequency of $f_m = 50Hz$

4.3 Comparison of the Most Promising Spread Spectrum Techniques

In this section, the discussed spread spectrum techniques with the best parameter combination according to the maximum reduction of the analyzed signals harmonics will be compared. For the randomized pulse position spread spectrum (RPP) a parameter of $\beta = 0.5$ achieved the maximum reduction. As both the randomized carrier frequency spread spectrum technique (RCF) and the frequency modulated spread spectrum technique underlie the same spreading mechanism, they are well comparable. Figure 4.9 shows the Fourier spectra of the above mentioned techniques in one diagram.

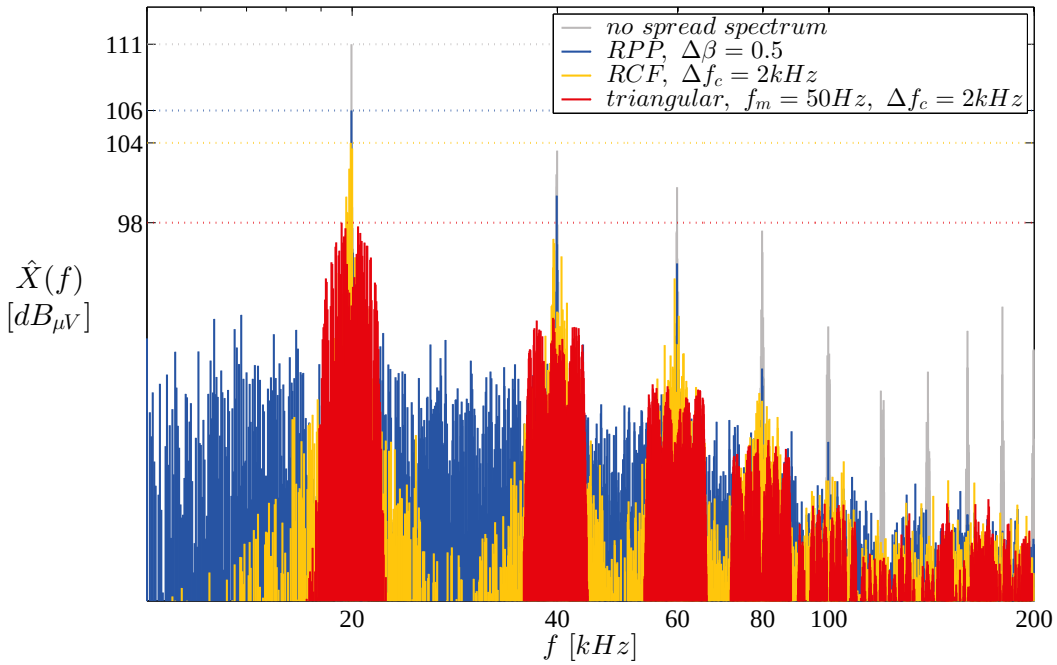

Figure 4.9: Direct comparison of RPP, RCF and frequency modulation spread spectrum

Considering figure 4.9, the deterministic spread spectrum approach obviously provides the best suppression of the fundamental frequency and its harmonics in the considered frequency range. As, in general, randomized spread spectrum techniques only allow the adjustment of one parameter, the deterministic spread spectrum techniques additionally offer two further degrees of freedom, namely the modulation frequency f_m and the modulation profile. As will be explained in chapter 6, the resulting possibilites of a freely selectable modulation frequency in deterministic spread spectrum techniques outperform the non-deterministic spread spectrum techniques, when the resolution bandwidth (RBW) of a measuring receiver and its detectors are also taken into account.

Chapter 5

Development of a Simulation Model for Condcuted Electromagnetic Emissions

This chapter documents the development of a simulation model of the drive system which provides a good representation of the real application in a measurement setup for the evaluation of conducted emissions (CE) according to CISPR25 [1]. This simulation model allows an estimation for the effectiveness of the presented spread spectrum techniques.

Thereby, the model should be sufficiently accurate and simple at the same time.

An overview of the simulation model is depicted in figure 5.1, where the electronic system under test (EUT) consists of the inverter and the stator of the PMSM.

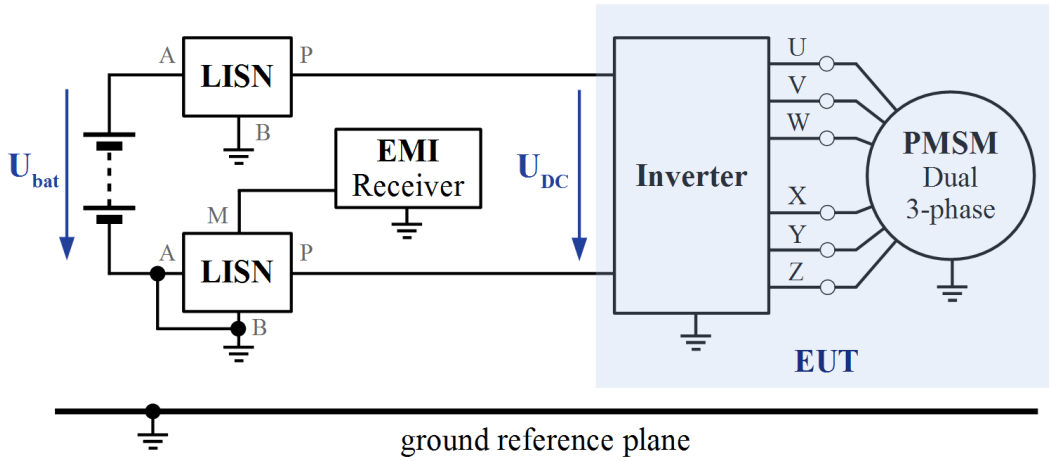

Figure 5.1: CE measurement setup

The left hand side represents the EMI measurement equipment which is necessary for measuring the CE. It comprises the line impedance stabilization networks (LISN), the EMI measuring receiver and the ground reference plane. The LISN, also referred to as artificial network (AN), emulates the 48V mains supply in a vehicle and additionally contains a passive highpass filter for coupling the CE into the EMI receiver. This provides a frequency selective evaluation of the the high frequency signal power. The ground reference plane emulates the vehicle's chassis.

The following sections will give a more detailed explanation of each component with the subsequent modeling approach.

5.1 Circuit Based Modeling of the EUT

The easiest and most obvious approach to fullfil the requirements regarding simplicity and efficiency is the modeling of the parasitic effects by lumped circuit elements with a subsequent adjustment using a measured impedance curve from an impedance analyzer. As impedance analyzers usually measure at fixed voltages, it has to be mentioned that this procedure does not reflect the reality for devices with nonlinear behavior according to the voltage. Nevertheless, the described method should be used as a first approximation. To compute the impedance curve, an AC analysis is performed in LTSpice by using a frequency swept current source as shown in figure 5.2. The impedance $\underline{Z}$ for the respective frequency can then be calculated by the relation between voltage and current. The derived model parameters of the considered components can be found in the appendix in table A.1.

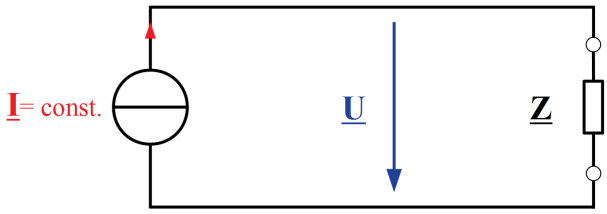

Figure 5.2: Obtaining impedance characteristics from a frequency sweep

5.1.1 Modeling of the Inverter

In the considered system, the voltage source inverter comprises 6 power MOSFET halfbridges and a range of parallel electrolytic DC link capacitors linked on the bus bars V_{bb+} and V_{bb-}, where always two halfbridges are connected to a full-bridge configuration into one package with a built-in ceramic decoupling capacitor and a snubber resistor. Thereby, the motor phases of the two 3-phase systems (UVW) and (XYZ) are interconnected as depicted in figure 5.3. This structure, in turn, can be modeled in two sub models in which its parameters can be obtained by two separate impedance measurements. These are the DC link capacitors and the fullbridge modules.

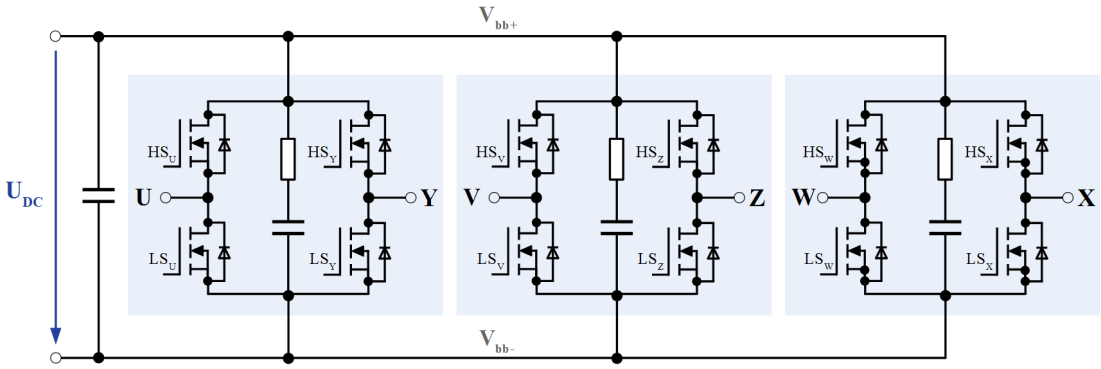

Figure 5.3: Structure of the inverter power electronics

Modeling of the DC Link Capacitors

An electrolytic capacitor can be modeled by the well-known equivalent circuit in figure 5.4(a) in which C_{DC} is the actual value of the capacitance, ESR_{DC} defines a constant equivalent ohmic resistance and ESL_{DC} represents the overall loop inductance. Figure 5.4(b) shows the impedance curve of one capacitor where in total seven capacitors are connected in parallel on the DC link.

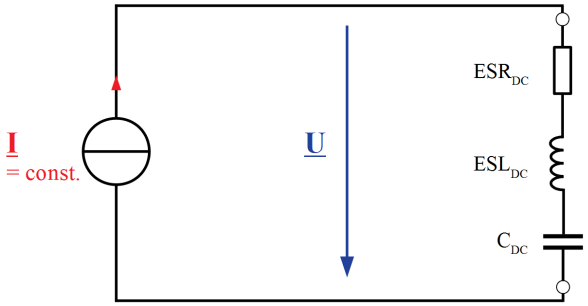

(a) Impedance model

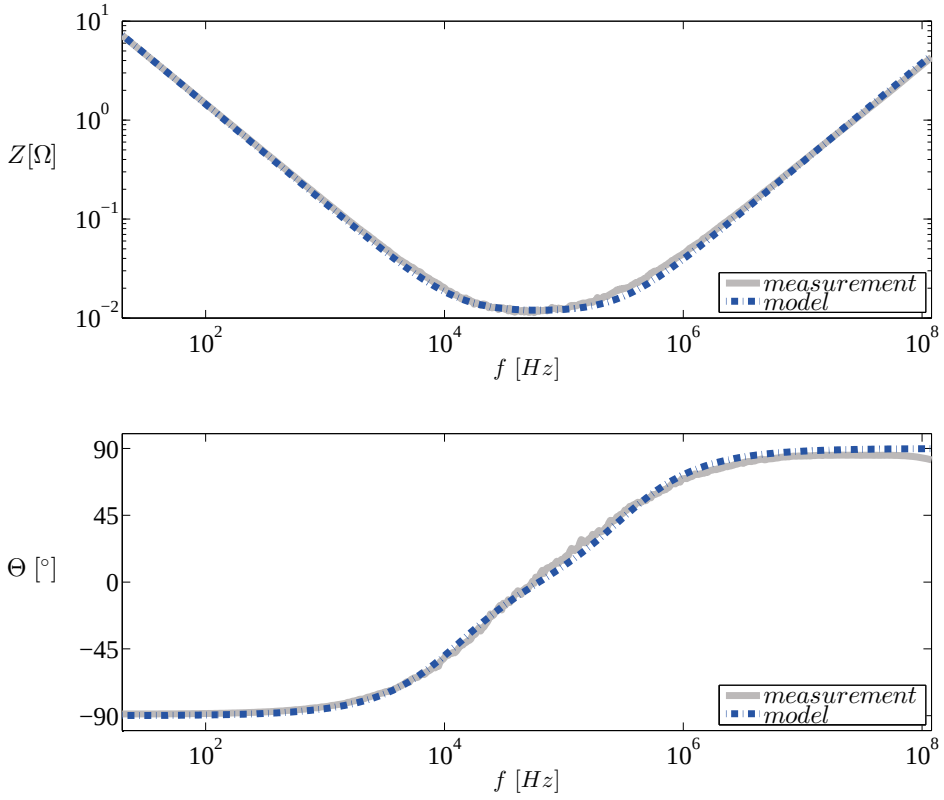

(b) Measured and simulated impedance characteristics

Figure 5.4: Impedance characteristics of one DC link capacitor

Modeling of the Full-Bridge Modules

A very simplified model that decribes the most essential properties of a discrete enhancement type n-channel MOSFET is shown in figure 5.5. $R_{DS,ON}$ and $R_{DS,OFF}$ describe the values for the ohmic channel resistance between Drain and Source of the MOSFET in the ON- and OFF-state. As descibed in section 3.2.1, a key parameter that defines the corner frequency f_{c1} of the frequency spectrum's envelope of a trapezoidal signal is the slew rate, or the rise and fall times t_r and t_f, respectively. For the switch model, the simulation tool allows a continuous transition between the resistance values for the ON- and the OFF state. The parameters of the switch model together with the RC circuit for the control signals were chosen to achieve load voltage transition times of approximately 200ns according to the transition times of the measured inverter output voltage waveform, averaged over one output voltage modulation period.

The parasitic body diode between Source and Drain is modeled by an ohmic resistance R_f characterizing the diode's ON-state resistance and a forward threshold voltage V_f allowing the ideal diode to pass from the blocking into the conducting state. Another crucial property, when it comes to EMC, is the equivalent output capacitance between Drain and Source that is modeled by the capacitance C_{oss}, a series resistance $R_{s,Coss}$ and a parallel resistance $R_{p,Coss}$. At this point, attention should be paid by choosing C_{oss} to a constant value, as, in reality, the output capacitance highly depends on the Drain-Source voltage U_{DS} and shows nonlinear behavior.

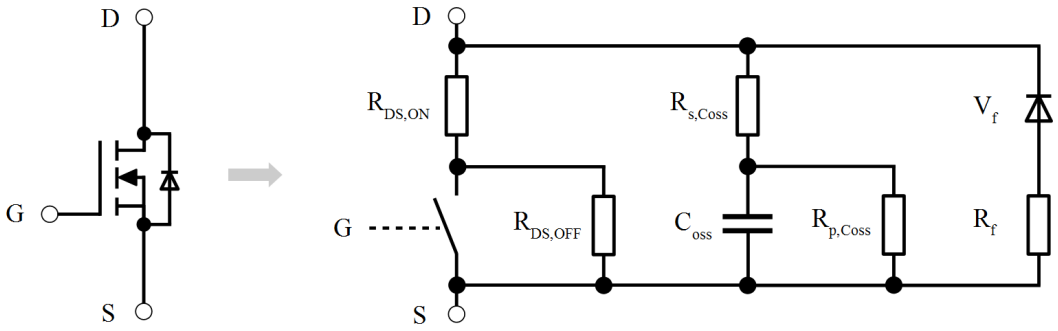

Figure 5.5: Simplified model of an enhancement type n-channel MOSFET

One module consists of 4 MOSFET dies that are connected via bonding wires to the package's lead frame. Both the package leads and the bonding wires contribute to a certain inductance which is modeled by the inductances L_{bb-lf} and L_{lf-die}, see figure 5.6(a). The ohmic part is represented by the corresponding values R_{bb-lf} and R_{lf-die}. The built-in RC-snubber circuit can be modeled in a similar way as described in 5.1.1 with the series elements $R_{s,snub}$ and $L_{s,snub}$ and the capacitance C_{snub} which is extended by a parallel resistance $R_{p,snub}$.

Figure 5.6(b) shows the comparison of the simulated and the measured impedance characteristic of one fullbridge module. The measurement was done for open switches by pulling the MOSFET's gate signals for both high-side (HS) and low-side switches (LS) to ground level. Considering the magnitude and phase in the plot, a parallel resonance occurs at above 20MHz which is caused by the capacitances C_{oss} in the switch branches, the snubber capacitor C_{snub} and the parasitic inductances L_{lf-die} and L_{snub}. If for example, a lower value is chosen for C_{oss} in the simulation, which corresponds

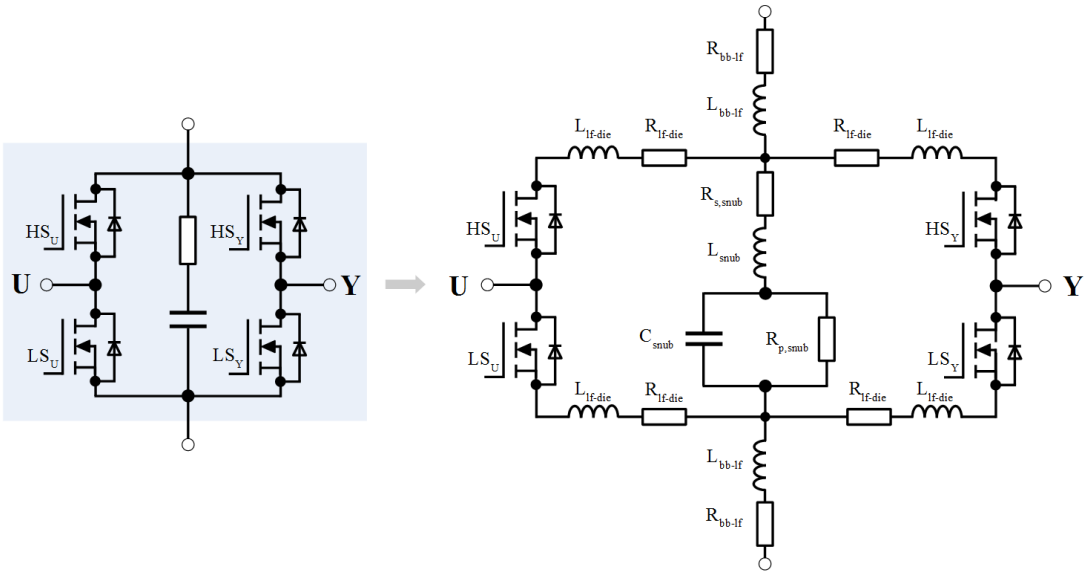

(a) Model of one full-bridge module

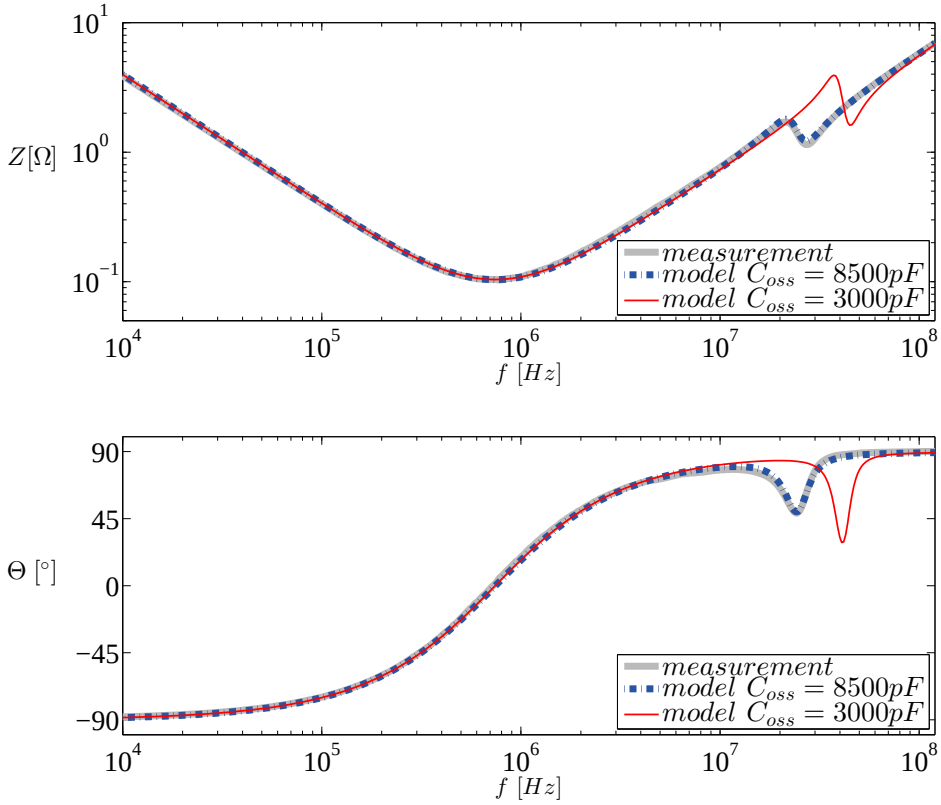

(b) Measured and simulated impedance characteristics

Figure 5.6: Impedance characteristics of one fullbridge module

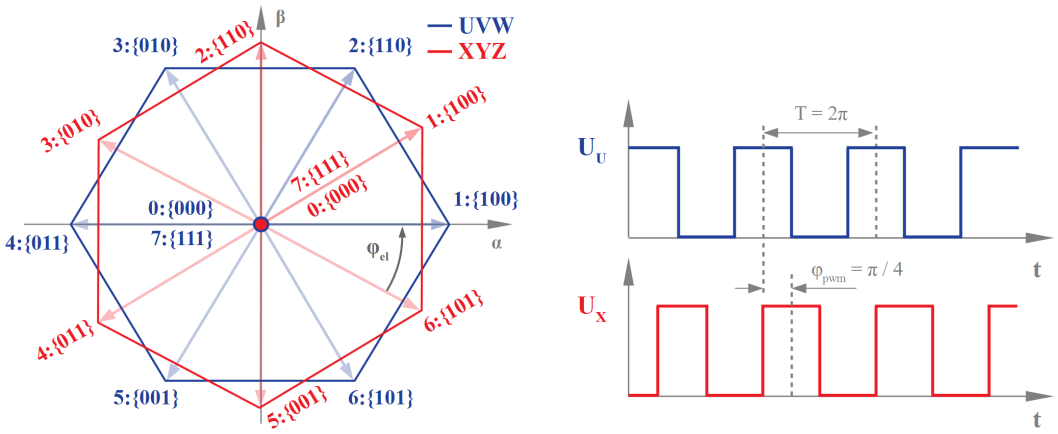

(a) Relation between the space vector systems

(b) Relation between the PWM systems

Figure 5.7: Relation between the 2 phase systems UVW and XYZ

to a higher Drain-Source voltage U_{DS}, the resonant frequency is shifted to a higher value. This effect applies equally to the voltage dependent behavior of the ceramic snuber capacitor's value.

PWM-Pattern Generation for the Gate Signals

In 3.1 an idealization of the gate signals was shown, where the switches in a halfbridge were switched simultaneously. Since MOSFET switches have a certain switching time, a transition region would occur in which the DC-link voltage would be shorted by the highside- and the lowside switch.

To avoid this case, an interlock time T_{lock} is applied where the result of the interlock algorithm is the same as of a turn-on delay for both the highside and the lowside switches. This, however, leads to an error in the voltage-time area of the halfbridge output voltage which is defined by its output current's sign during the interlock time. This, in turn, results in a distortion of the phase currents, especially at its zero crossings. Therefore, the control system in the real application utilizes the measured phase currents in a feedforward compensation as a countermeasure for the described nonlinear effect.

For measuring the conducted emissions in the system, a quasi stationary state is chosen, where a certain target value is set in the inverters current control loop with a certain frequency of the rotating magnetic field. Different from the real system, a constant amplitude voltage spacevector is used in the simulation model which leads to the same RMS phase currents, in order to drastically reduce simulation time. In the model, the compensation of the interlock time was implemented by adding or subtracting a constant value to the voltage spacevector components in the $\alpha\beta$-plane depending on the sign of the halfbridge output currents in the circuit simulation.

The electric phase between the two 3-phase systems is $\phi_{el} = \frac{\pi}{6}$, according to the spatial arrangement of the winding systems of the motor, see figure 5.7(a). As shown in figure 5.7(b), the phase angle between the two PWM signals is set to $\phi_{pwm} = \frac{\pi}{4}$ with the intention to reduce the voltage ripple on the DC-link.

5.1.2 Modeling of the PMSM's Stator

The structure of the PMSM consists of two separate 3-phase windings with a number of pole pairs $p = 3$ and a spatial arrangement of $\phi_{el} = \frac{\pi}{6}$ that are interconnected in a Δ-configuration. Since the measurements are performed without the machine's rotor the stator can be modeled by the circuit depicted in figure 5.8(a). Due to the symmetry, an impedance measurement between the phases U and V is sufficient to obtain the values for R_{ph} and L_{ph}. The measured and simulated impedance curves between the phases U and V are shown in figure 5.8(b), where the frequency range for the measurement system was limited to 120kHz.

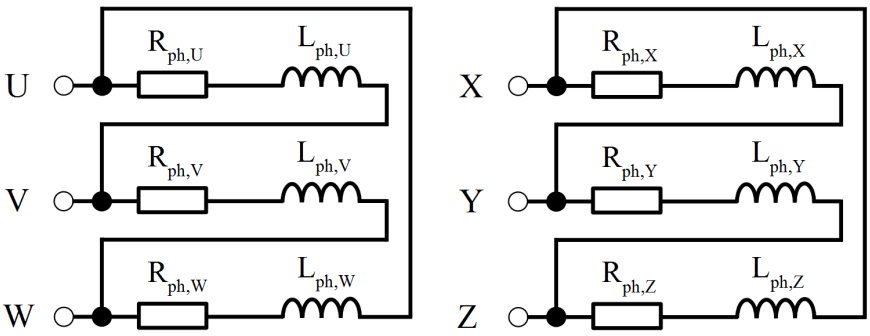

(a) Impedance model of the PMSM's stator

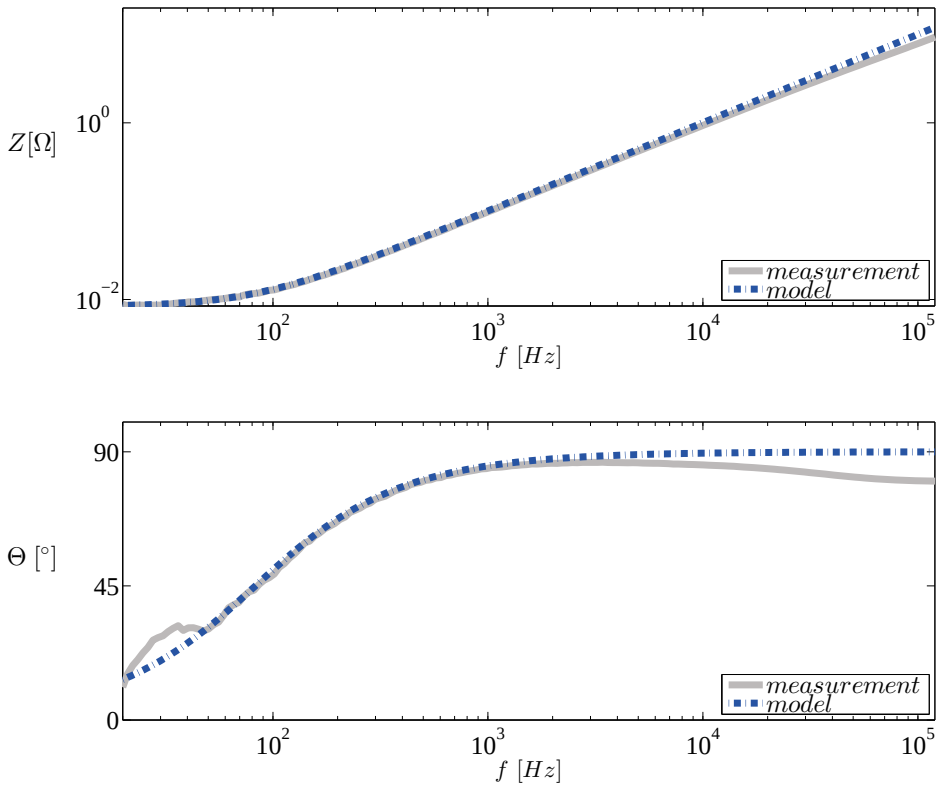

(b) Measured and simulated impedance between the phases U and V

Figure 5.8: Impedance characteristics of the PMSM's stator

5.1.3 Modeling of the Ground Connections of the EUT

As grounding connection between the EUT and the ground reference plane, ground straps were used for both inverter and motor which were modeled by a circuit depicted in figure 5.9(a). The measured and the simulated impedance characteristics of one ground strap are shown in 5.9(b).

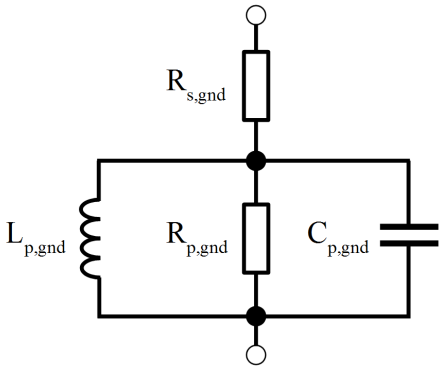

(a) Impedance model for one ground strap

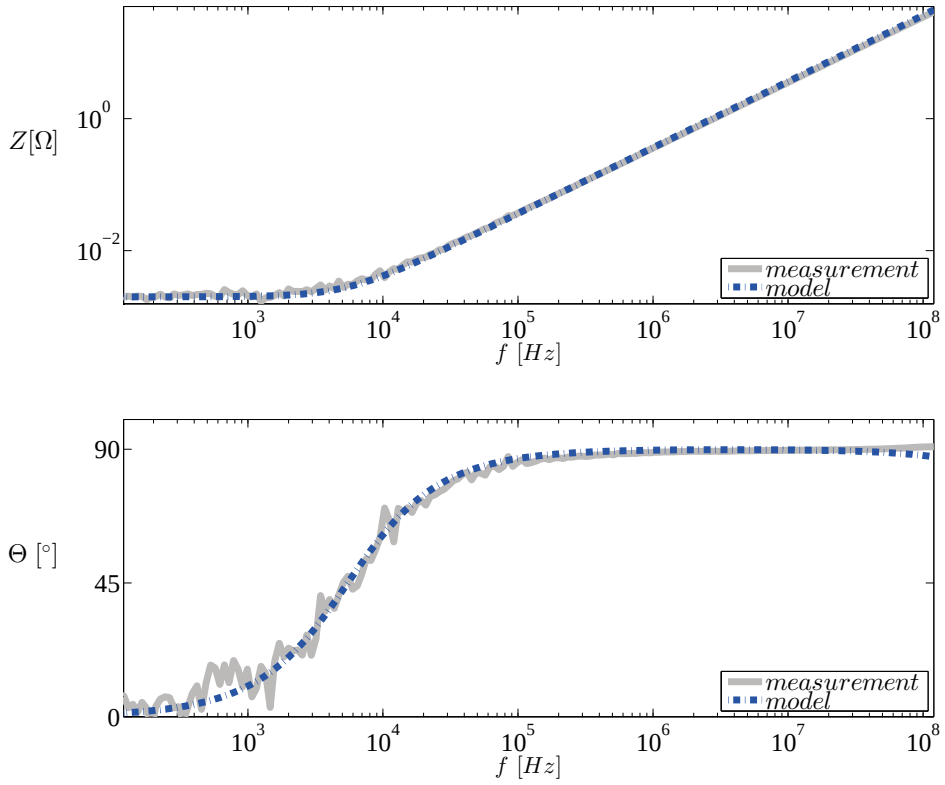

(b) Measured and simulated impedance characteristics

Figure 5.9: Impedance characteristics of one ground strap connection

5.1.4 Sources of Electromagnetic Emissions and Modeling of the Coupling Paths

In the system, the conducted electromagnetic emissions can be divided into common mode- (CM) and the differential mode emissions (DM). 5.10 illustrates the capacitive coupling path for CM emissions for one phase and the occurrence of DM emissions, which are explained in more detail in the following sections.

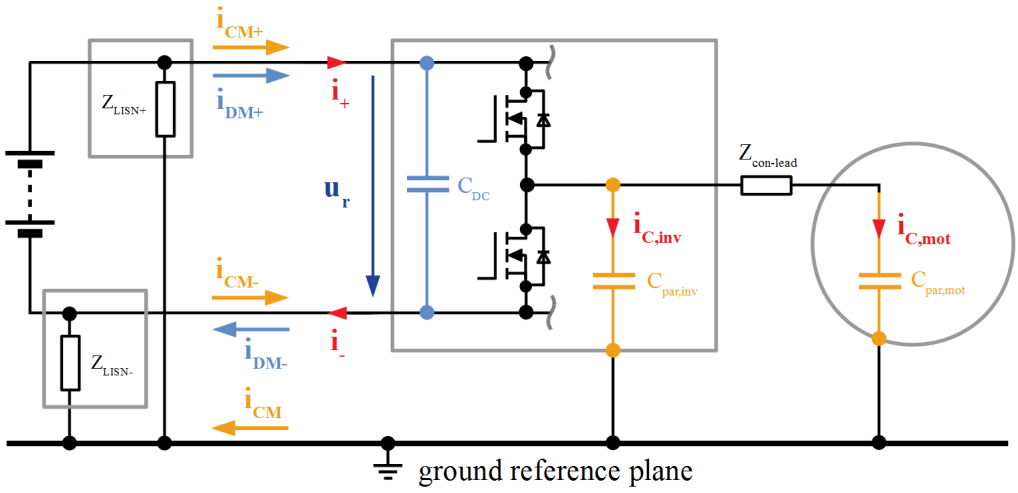

Figure 5.10: Definition of common mode- and differential mode emissions

Common Mode Emissions

Due to the high slopes of the phase voltages, currents i_c arise through the parasitic capacitances $C_{par,inv}$ and $C_{par,mot}$ according to the relation in equation 5.1, which close their loop through the connections to the ground reference plane and the impedace of the artificial networks Z_{LISN+} and Z_{LISN-}.

$$i_c = C_{par} \cdot \frac{du_c}{dt} \tag{5.1}$$

The distribution of the currents i_+ and i_- in both supply lines (KL40, KL41) further leads to the common mode current i_{cm} according to equation 5.2.

$$i_{CM} = i_+ - i_- = i_{CM+} + i_{CM-} \tag{5.2}$$

The parasitic motor capacitance is formed by the stator windings and the stator slots. Due to the large surface and at the same time small clearance between the wires and the slots in the stator, the motor capacitances have the greatest share of CM emissions. As a first approximation of the motor capacitance a model with lumped capacitances $C_{par,mot}$ is used for each phase, since a modeling attempt with distributed parameters seems too complex with respect to the simulation target. Figure 5.11(a) shows the measured and the simulated impedance characteristics between the short-circuited motor phases UVW and the motor housing, whereby the modeling was done in the same manner as shown in figure 5.4(a) with the series elements $R_{par,mot}$ and $L_{par,mot}$ and $C_{par,mot}$.

Similarily, the parasitic capacitances $C_{par,inv}$ between the lead frame connections of the phases within the fullbridge modules and the inverter's cooling plate also contribute to the capacitive coupling path (see figure 5.10).

The measured impedance characteristics of the parasitic inverter capacitance between one phase and the fullbridge module's cooling plate is shown in 5.11(b). Again, a model consisting of the series elements $R_{par,inv}$, $L_{par,inv}$ and $C_{par,inv}$ is utilized.

Differential Mode Emissions

The DM emission arise through the voltage ripple u_r on the DC link evoked by the charging and discharging cycles of the DC link capacitors and can be described by the DM current as shown in equation 5.3.

$$i_{DM} = \frac{i_+ + i_-}{2} = \frac{i_{DM+} + i_{DM-}}{2} \tag{5.3}$$

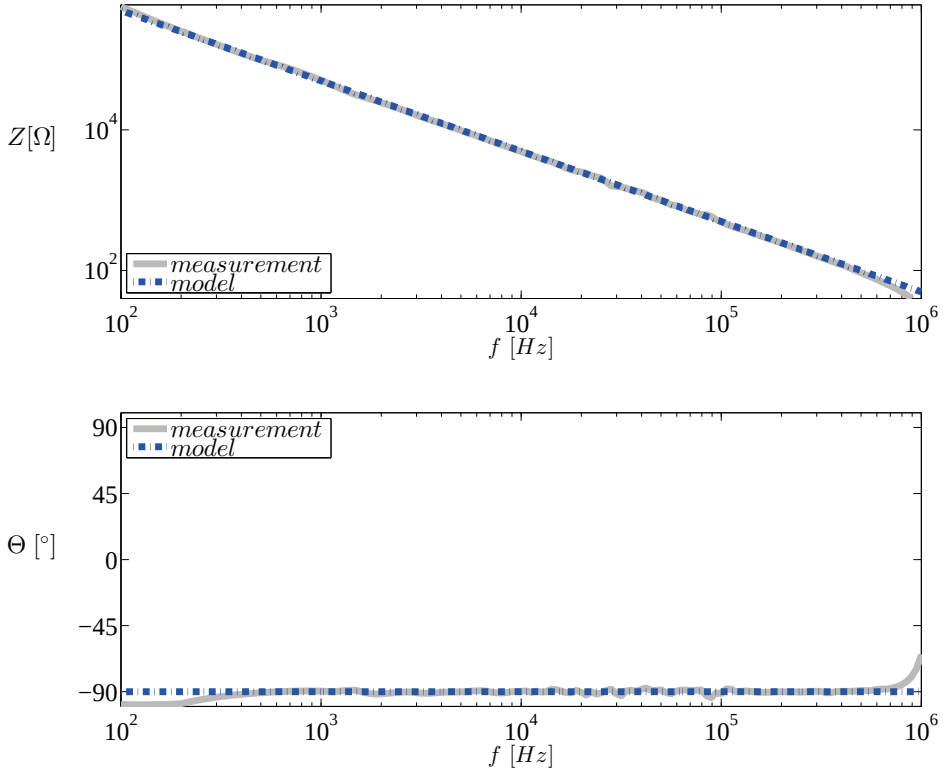

(a) Parasitic motor capacitance $C_{par,mot}$ per phase

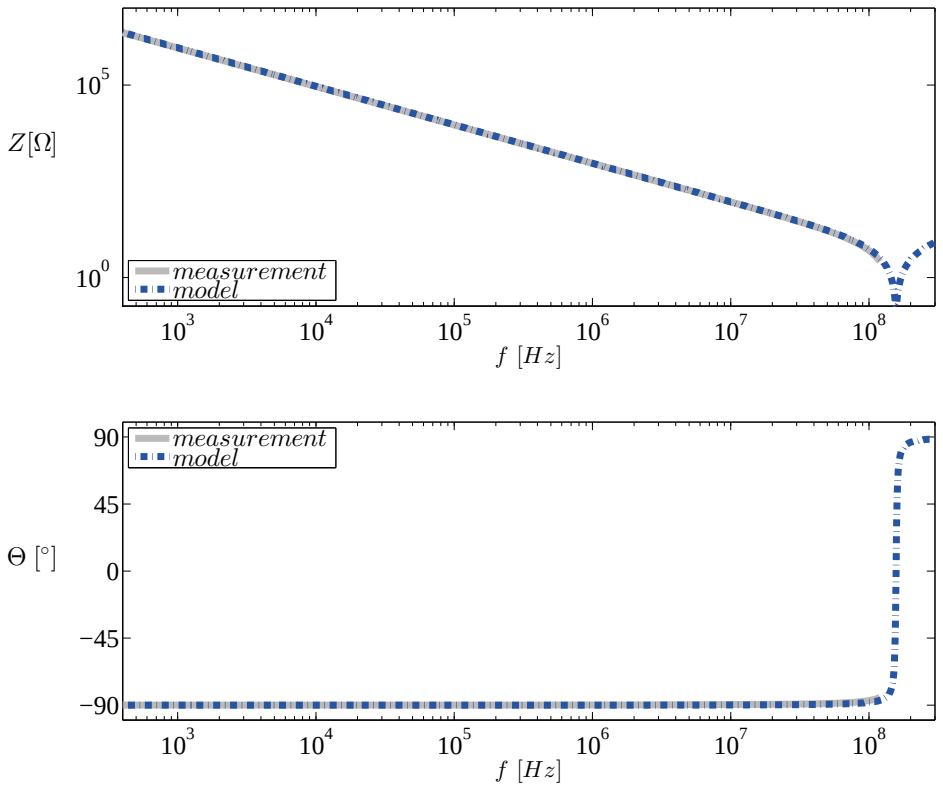

(b) Parasitic inverter capacitance $C_{par,inv}$ per phase

Figure 5.11: Measured and simulated impedance characteristics of the parasitic capacitances

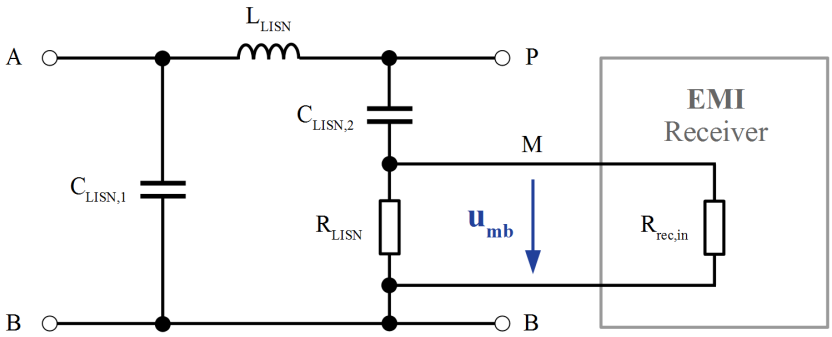

Figure 5.12: Impedance model of the LISN according to CISPR25 [1]

5.1.5 Model of the Artificial Network (LISN)

For the measurement of conducted emissions an artificial network (AN) is inserted between the power source and the EUT that emulates the DC network in a vehicle. The AN defines the impedance for the RF currents on the one hand and acts as a filter for emissions coming from the power source on the other hand. Therefore, it is also referred to as line impedance stabilization network (LISN). Principially, the LISN consists of an inductance L_{LISN} and a capacitance $C_{LISN,1}$, where the inductor is realized by an air coil to prevent saturation. In order to couple the *RF* signal on the respective supply line into the EMI measuring receiver, a passive high pass filter is used.

The model of the LISN according to CISPR25 can be found in [1] and is shown in figure 5.12.

5.2 Modeling of the EMI Measuring Receiver

Unfortunately, the spectral analysis methods presented in chapter 3.2 are not valid or sufficient for the evaluation of electromagnetic emission since they do not provide information about the spectral energy in a certain bandwidth. In order to ensure a simulation model conforming to CISPR16-1-1 [1] and CISPR25 [1], two different modeling approaches for emulating an EMI measuring receiver are presented in this section. In order to understand the background of these approaches the operating principle used in swept-tuned EMI receivers as well as the most important detectors are briefly explained first.

5.2.1 Operating Principle of Swept EMI Receivers

The classical swept EMI receiver utilizes the superheterodyne operating principle to obtain the emission spectrum from the input signal u_{mb}, where a simplified block diagram is depicted in 5.13. A very good and detailed description of this procedure can be found in [21].

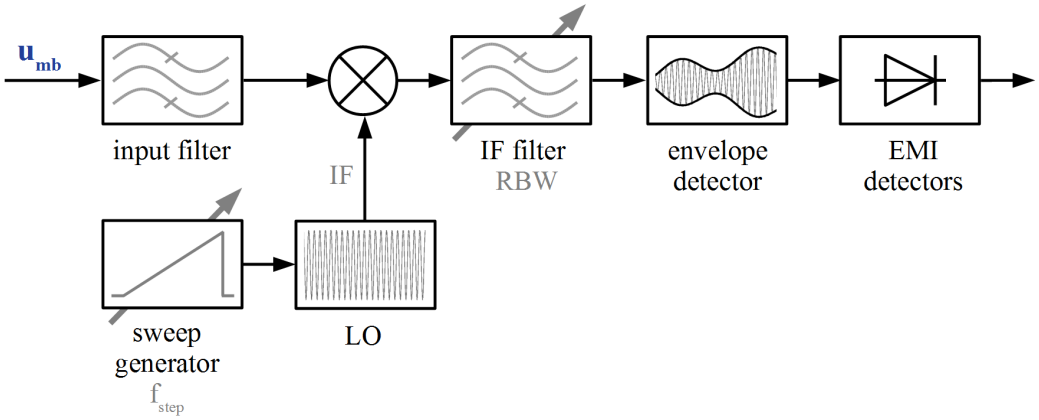

Figure 5.13: Simplified block diagram of a swept EMI receiver

In the first stage the signal to be analyzed (u_{mb} in figure 5.12) is limited to the bandwidth of interest by an input filter. The second stage comprises a mixer and a local oscillator (LO) whose instanteneous frequency is derived from a sweep generator that steps through the measurement bandwidth. Thus, the (band limited) input signals frequency spectrum is shifted to an intermediate frequency (IF). Togehter with the use of a band pass- or IF-filter with a specified resolution bandwidth (RBW) [2] at a fixed center frequency, the input frequency spectrum seems to slide through the frequency response of the IF-filter. The characteristics of the IF-filter is implemented as a tuneable filter, as the required RBW depends on the frequency range (table 5.1). An envelope detector recovers the mixed signal's envelope at the considered bandwidth at the IF which is fed into the EMI detector(s) afterwards. The most important detectors are the peak-, the quasi-peak and the average detector. The peak detector evaluates the peak value of the envelope. Therefore, it returns the highest value. The average detector forms the arithmetic mean of the envelope. The quasi-peak detector evaluates the appearance rate of peak value whereby its value lies in between the peak- and the average value in general. For this reason, only the average- and the peak value are of interest in this thesis.

5.2.2 Modeling Approach by Windowing in the Frequency Domain

The fundamental idea of the first approach emulating an EMI measuring receiver is the direct application of the resolution bandwidth (RBW) of the intermediate frequency (IF) bandpass filter (figure 5.13) on the input signal's frequency spectrum $U(f)$. It is equal to windowing in the frequency domain. A block diagram of the executed postprocessing steps is depicted figure 5.14.

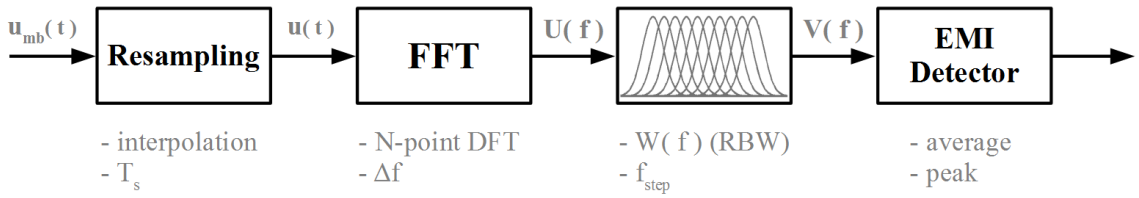

Figure 5.14: Post processing steps of the first EMI receiver model approach

Resampling

As the solvers in transient circuit simulations generally operate with variable time steps, the input signal u_{mb} has to be resampled to a signal with fixed time steps at first to allow the subsequent computation of the N-point DFT with an FFT algorithm. This is done by linear interpolation with a resampling time T_s which must be sufficiently small to image the desired frequency range, according to the Nyquist-Shannon theorem. For example, to ensure a maximum frequency of 250MHz, a minimum sampling time of $T_s = 2ns$ is necessary.

FFT

The frequency spectrum of the resampled input signal is then computed by the DFT with a rectangular window of the length N that corresponds to the measurement- or scanning time t_{scan} of the EMI receiver. However, there will be states of operation in which the longest period appearing in the system will be smaller than the required scanning time t_{scan} for the respective EMI detector. This will either be the fundamental frequency f_{el} of the space vector modulation or the modulation frequency f_m of the used spread spectrum technique. For this reason, the highest appearing period is chosen as DFT observation time to reduce simulation time.

Windowing in the Frequency Domain

In order to consider the resolution bandwidth (RBW) of the IF bandpass filter of the swept EMI receiver, the RBW according to CISPR16-1-1 [2] is applied to the spectrum $U(f)$ by a multiplication with the filter's frequency response $W(f)$.

Thereby, the sweep of the intermediate frequency IF is achieved by successively shifting $W(f)$ over the considered frequency range with the frequency step size f_{step} which must be less than or equal to $\frac{RBW}{2}$ [2]. This results in a series of overlapping frequency spectra $V_i(f)$ which are then processed to

the desired EMI detector values later (see equation 5.4).

$$V_i(f) = U(f) \cdot W_i(f) \tag{5.4}$$

Table 5.1 shows the essential parameters RBW and f_{step} for the modeling approach as well as the required minimum scanning time t_{scan} [1] for the peak- and the average detector depending on the investigated frequency range.

Frequency Range		RBW at -6dB	$f_{step,min}$	$t_{scan,avg}$	$t_{scan,peak}$
Band A	9 kHz – 150 kHz	200 Hz	100 Hz	-	-
Band B	150 kHz – 30 MHz	9 kHz	4.5 kHz	50 ms	50 ms
Band C	30 MHz – 300 MHz	120 kHz	60 kHz	5 ms	5 ms

Table 5.1: Required resolution bandwidth RBW at $-6dB$, maximum frequency stepsize f_{step} and minimum scan time t_{scan} according to CISPR16-1-1 [2] and CISPR25 [1]

Figure 5.15 depicts the boundaries within which the IF filter's frequency response may be located and the designed filter W_f that fulfills these requirements for the frequency bands A, B and C, where a Gaussian window function was used (see equation 5.5 [22]). Thereby, the center frequency of $W(f)$ was always chosen to be $f_c = 0Hz$ with the standard deviations $\sigma_A = 1.87 \cdot 10^{-3}$, $\sigma_B = 4.16 \cdot 10^{-5}$ and $\sigma_C = 3.12 \cdot 10^{-6}$ for the three CISPR bands A, B and C.

$$W_i(f) = e^{-2\,\pi^2\,\sigma^2\,(f-f_{c,i})^2} \tag{5.5}$$

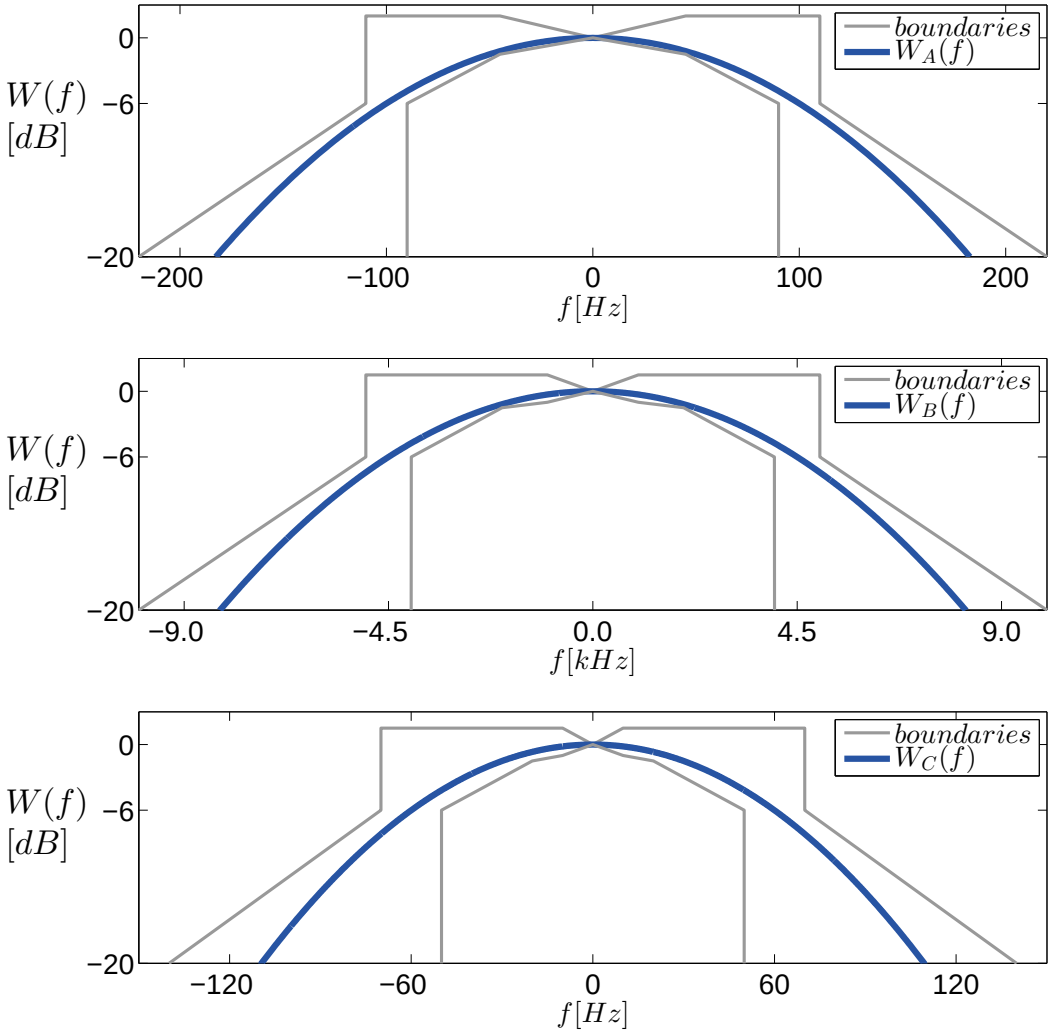

Figure 5.15: Required RBW according to [2] for the frequency bands A, B and C

Figure 5.16 illustrates the windowing principle for four frequency stepping cycles in the CISPR band B where the minimum required frequency step size was chosen to $f_{step} = \frac{RBW}{2}$. The analyzed test signal u_{mb} was adduced from a measurement on the LISN on KL41 as depicted in figure 5.1 which was also used for the model validation.

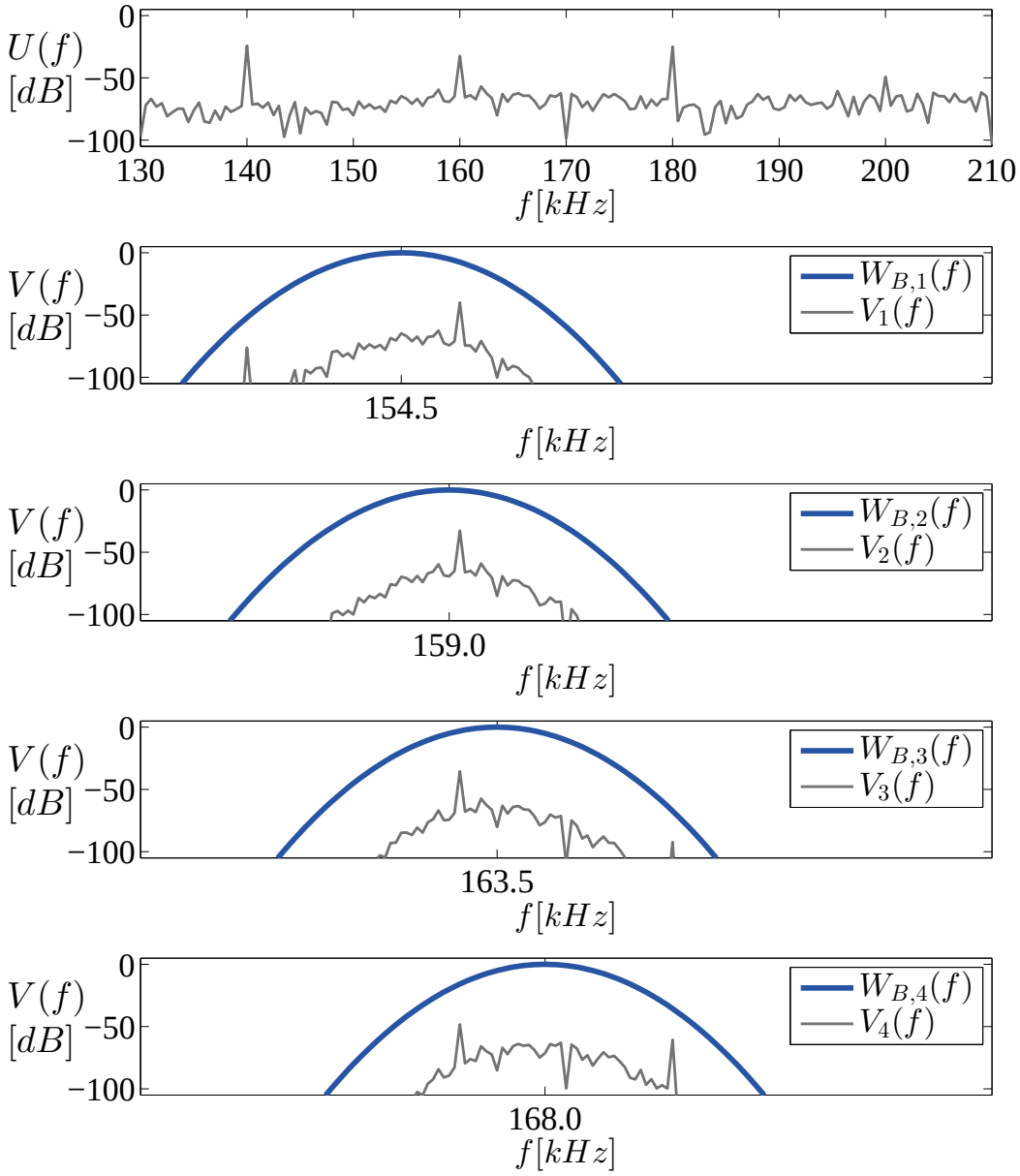

Figure 5.16: Computation steps of applying the window function $W(f)$ on the signal spectrum $U(f)$ in the CISPR band B (RBW=9 kHz, f_{step} = 4.5 kHz)

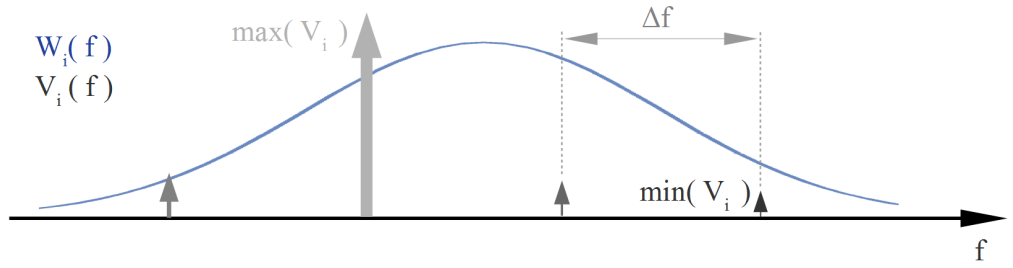

(a) Input signal spectrum $U(f)$ and windowed signal spectrum $V(f)$

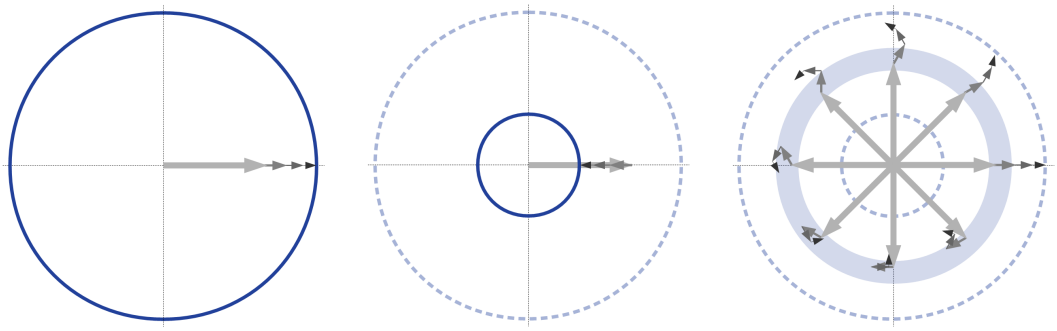

(b) Peak detector (c) Minimum envelope (d) Average detector

Figure 5.17: EMI detector value computation concept by evaluating the spectral components within the RBW

EMI Detector Value Computation

The concept of obtaining the EMI detector values utilizes the frequency spectral components that fall into the RBW in the windowed signal spectra $V_i(f)$. Figure 5.17 illustrates the calculation of the peak- and average detector values by an appropriate composition of the frequency spectral components.

Thereby, the peak value can be computed by summing up all spectral magnitudes that fall into the considered bandwidth, which can be interpreted as the coinciding of the vectors' phases. This case can be observed in figure 5.17(b) where the radius of the continuous blue circle corresponds the peak value. For this reason, the peak value can be understood as a snapshot where the composition of the spectral components achieves the highest resulting magnitude. Similar to that strategy, the lower boundary is attained in 5.17(c).

Thus, the average value will fall in between the minimum and the peak value and represents the mean value of all possible compositions (see figure 5.17(d)). Therefore, the first model attempt for emulating the average detector value was the averaging of all frequency spectral components $V_i(f)$ within the corresponding bandwidth. However, the simulation showed that picking the highest occuring spectral component in $V_i(f)$ for the average detector value leads to the best compliance with the measurement results. A plausible explanation for this phenomenon is the small RBW utilized relative to the considered frequency range. For example, the occurrence of more than one frequency spectral components within the RBW implies that their corresponding frequency values are in the same scale which leads to beats in the time domain signal. Thus, the mean amplitude value averaged over one beat period will be equal to the highest frequency spectral amplitude $max(V_i)$ appearing in

$V_i(f)$.

EMI measuring receivers generally return the RMS value, since they are intended to evaluate the signal power within the RBW. The result of the FFT, however, delivers the magnitude of the spectral components. As a consequence, the calculated peak- and average values first have to be devided by the factor $\sqrt{2}$ to obtain the simulated peak- and the average detector values of the EMI receiver model (see equations 5.6 5.7).

$$PK(f_i) = \frac{1}{\sqrt{2}} \sum_{n=1}^{M} V_i(f_n) \tag{5.6}$$

$$AVG(f_i) = \frac{1}{\sqrt{2}} max(V_i) \tag{5.7}$$

The main issue of this model approach is to choose the three crucial design parameters correctly: the frequency resolution Δf that results from the FFT observation length (see 3.2.2 and figure 5.17(a)) and the bandwidths BW_{avg} and BW_{pk} used for the detector value calculation. For example, higher values of Δf result in a higher number of frequency spectral components within a certain bandwidth. Equally, considering a wider frequency range also leads to the evaluation of a higher number of spectral components. It became apparent that the summation of a high number of low magnitude values leads to greater deviations between measurement and simulation, which is suspected to result from a numerical problem.

In terms of a model validation, the time domain signal u_{mb} was measured by an oscilloscope on the LISN on KL41, as depicted in figure 5.1, and was then fed into the EMI receiver model. Afterwards, the model parameters were tuned until an acceptable compliance between the model and the EMI receiver measurement result was attained. The tuned parameter set for the bands A, B and C are shown in table 5.2. Figure 5.18 depicts the comparison between measurement and simulation for the CISPR bands A,B and C in the frequency range between $9kHz$ and $100MHz$. At this point, it has to be mentioned that the validation of the model in band C turned out to be problematic, either because of the limited time resolution of the measured time sample, or the properties of the used oscilloscope (e.g. the limited dynamic range) itself (see 5.2.4). Therefore, the parameter set for band C was attained by scaling down the one of band A as a first attempt.

Frequency Range		RBW_{-6dB}	BW_{avg}	BW_{peak}	Δf	σ
Band A	$9\ kHz - 150\ kHz$	$200\ Hz$	$200\ Hz$	$100\ Hz$	$50\ Hz$	$1.87 \cdot 10^{-3}$
Band B	$150\ kHz - 30\ MHz$	$9\ kHz$	$50\ kHz$	$25\ kHz$	$1.5\ kHz$	$4.16 \cdot 10^{-5}$
Band C	$30\ MHz - 300\ MHz$	$120\ kHz$	$120\ kHz$	$60\ kHz$	$20\ kHz$	$3.12 \cdot 10^{-6}$

Table 5.2: Tuned EMI receiver model parameters for an acceptable compliance between model and measurement

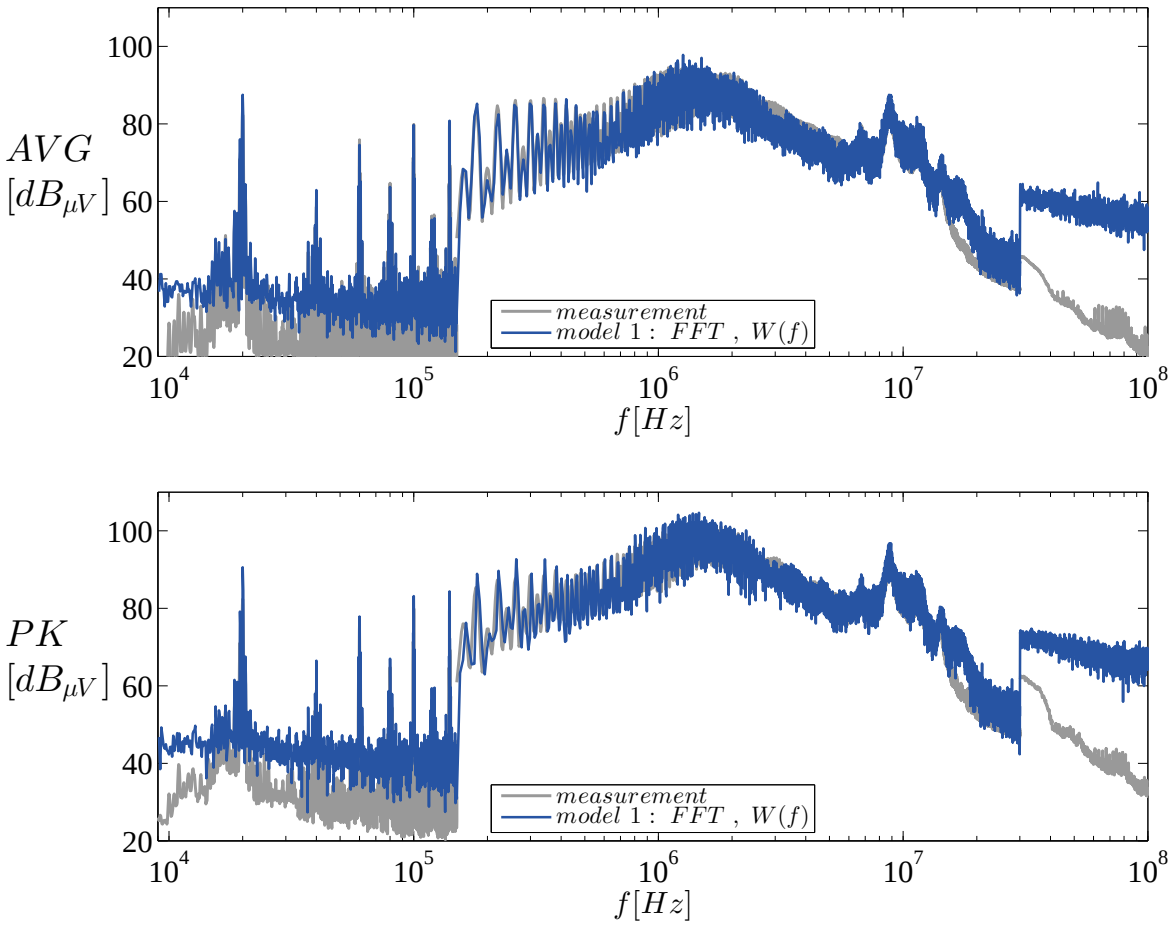

Figure 5.18: Comparision of the measured and the simulated average- and peak detector values of the first approach modeling an EMI receiver

5.2.3 Modeling Approach by Windowing in the Time Domain

Another approach to model an EMI measuring receiver resembles with the Short Time Discrete Fourier Transform (STDFT) presented in 3.2.2. The latest generation of EMI test receivers, also referred to as *Time Domain EMI receivers*, utilize the STDFT as well, as its theory most likely matches with that of swept-tuned EMI receivers or spectrum analyzers [25], [26]. A series of DFT spectra is computed by using short overlapping window functions $w_i[n]$ on the resampled signal $u[n]$ in the time domain as illustrated in the block diagram in figure 5.19. The *Resampling* block is the same as explained in 5.2.2.

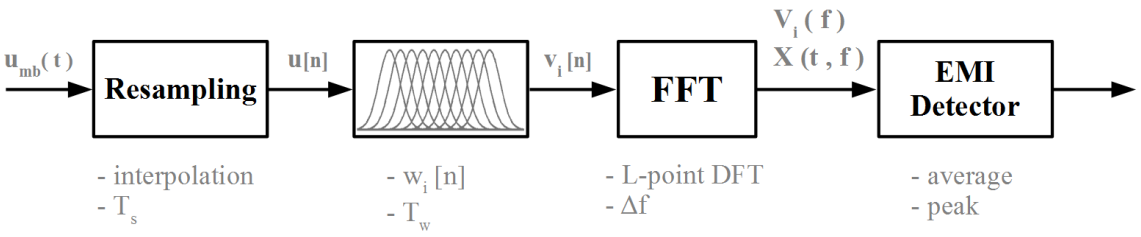

Figure 5.19: Post processing steps of the second EMI receiver model approach

Windowing in the Time Domain

The relation of the window function $w[n]$ that corresponds to the window function in the frequency domain $W(f)$ derived in 5.2.2 is shown in equation 5.8 [22]. Thereby, the standard deviations σ stay unchanged and are listed in table table 5.2. The window length $L = \frac{T_w}{T_s}$ was chosen to $T_w = \frac{4}{RBW}$ that results in a frequency resolution of $\Delta f = \frac{1}{T_w}$.

$$w[n] = \frac{T_s\,(L-1)}{\sigma\,\sqrt{2\pi}} \cdot e^{-\frac{1}{2}\left(\frac{n\,T_s}{\sigma}\right)^2} \tag{5.8}$$

In order to ensure a seamless evaluation of the analyzed signal $u(t)$ an overlap factor OVL is utilized by sequentially shifting the temporal window function $w_i[n]$ by N_{sh} samples in (discrete) time n as in equation 5.9. According to the considered standard [2], an overlap of more than 0.75 has to be used in FFT based EMI measuring receivers.

$$OVL = \frac{L - N_{sh}}{L} \tag{5.9}$$

Figure 5.20 depicts the procedure of attaining the windowed functions $v_i(t)$ from the signal $u(t)$ in the CISPR band B where an overlap of $OVL = 0.9$ was chosen.

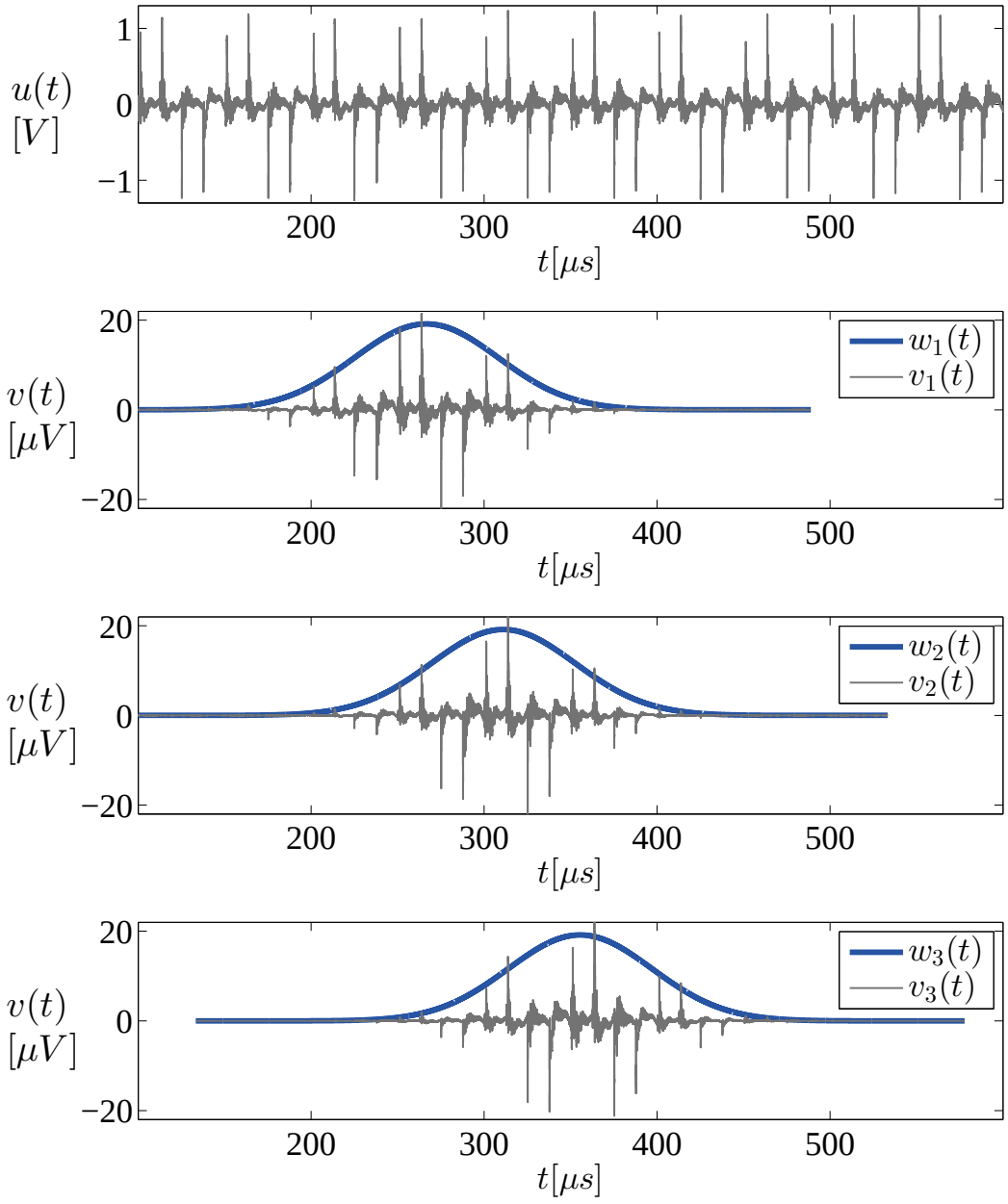

Figure 5.20: Application of overlapping window functions $w_i(t)$ on the input signal $u(t)$

FFT

Afterwards, the spectra $V_i(f)$ corresponding to the windowed signals $w_i(t)$ are computed by an L-point FFT resulting in a time dependent spectrum $X(t, f)$ which form the basis for the subsequent detector value calculation. The related theory has already been presented in 3.2.2.

Figure 5.21 shows the calculated spectrogram $X(t, f)$ from the measured time-domain signal $u_{mb}(t)$ in the CISPR band B.

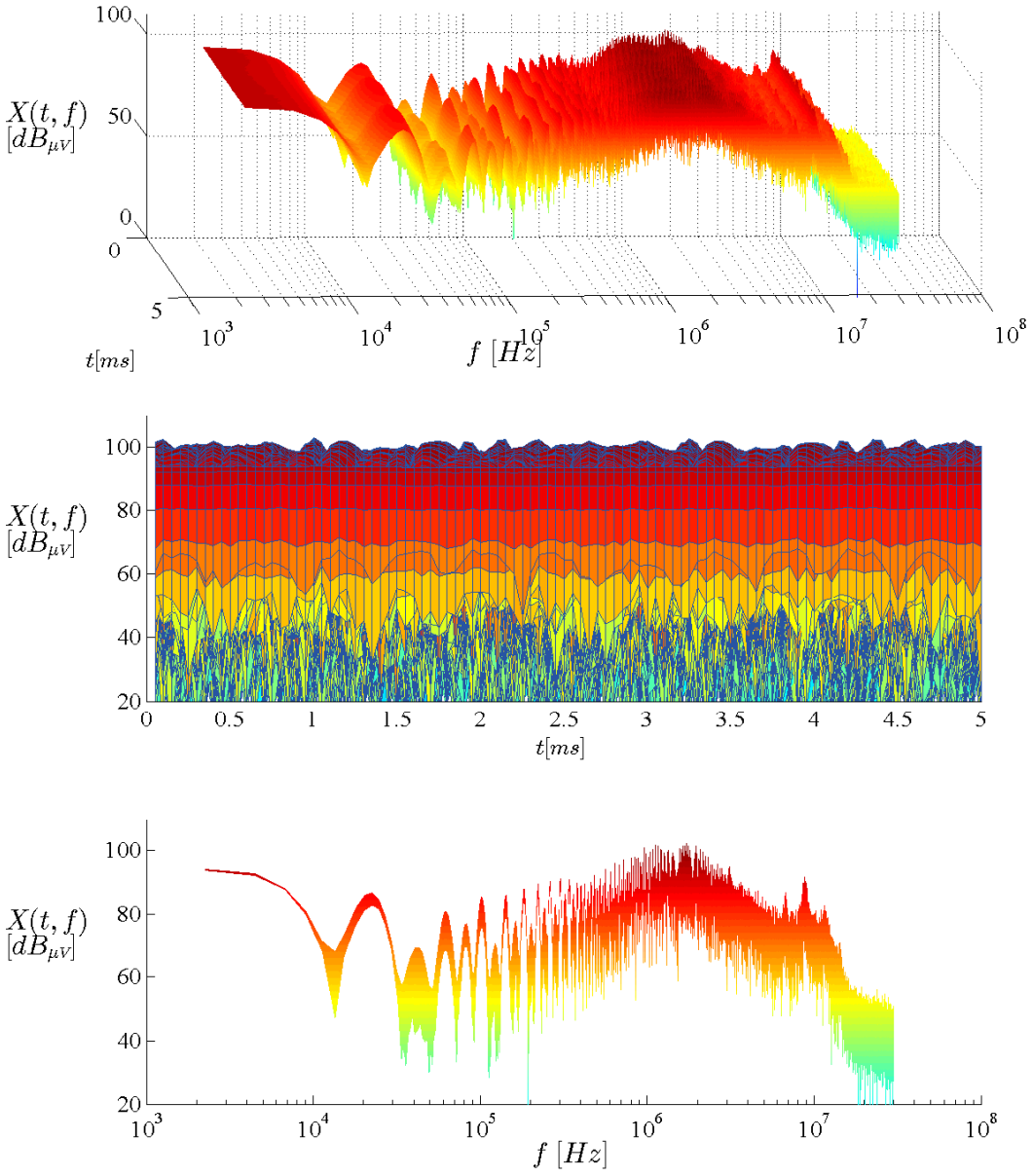

Figure 5.21: Spectrogram X(t,f) of the analyzed signal u(t) in the CISPR band B (RBW=9kHz)

EMI Detector Value Computation

Different to the previous modeling approach, the calculation of the detectors values is more comprehensible in the mathematical sense. Considering the spectrum $X(t, f)$, the peak value can be obtained

by choosing the highest value along the time axis for each frequency bin where M is the number of the calculated spectra (see equation 5.10). The average value can then be determined by calculating the mean value along the time axis for each frequency bin (see equation 5.11). Again, the peak- and the average value have to be divided by the factor $\sqrt{2}$ since the used FFT algorithm returns the magnitude values of the spectrum.

$$PK(f_i) = max\ X(t, f_i) \tag{5.10}$$

$$AVG(f_i) = \frac{1}{M}\sum_{j=1}^{M} X(t_j, f_i) \tag{5.11}$$

Figure 5.22 shows the calculated peak- and average detector values from the analyzed signal $u(t)$ for the CISPR band B.

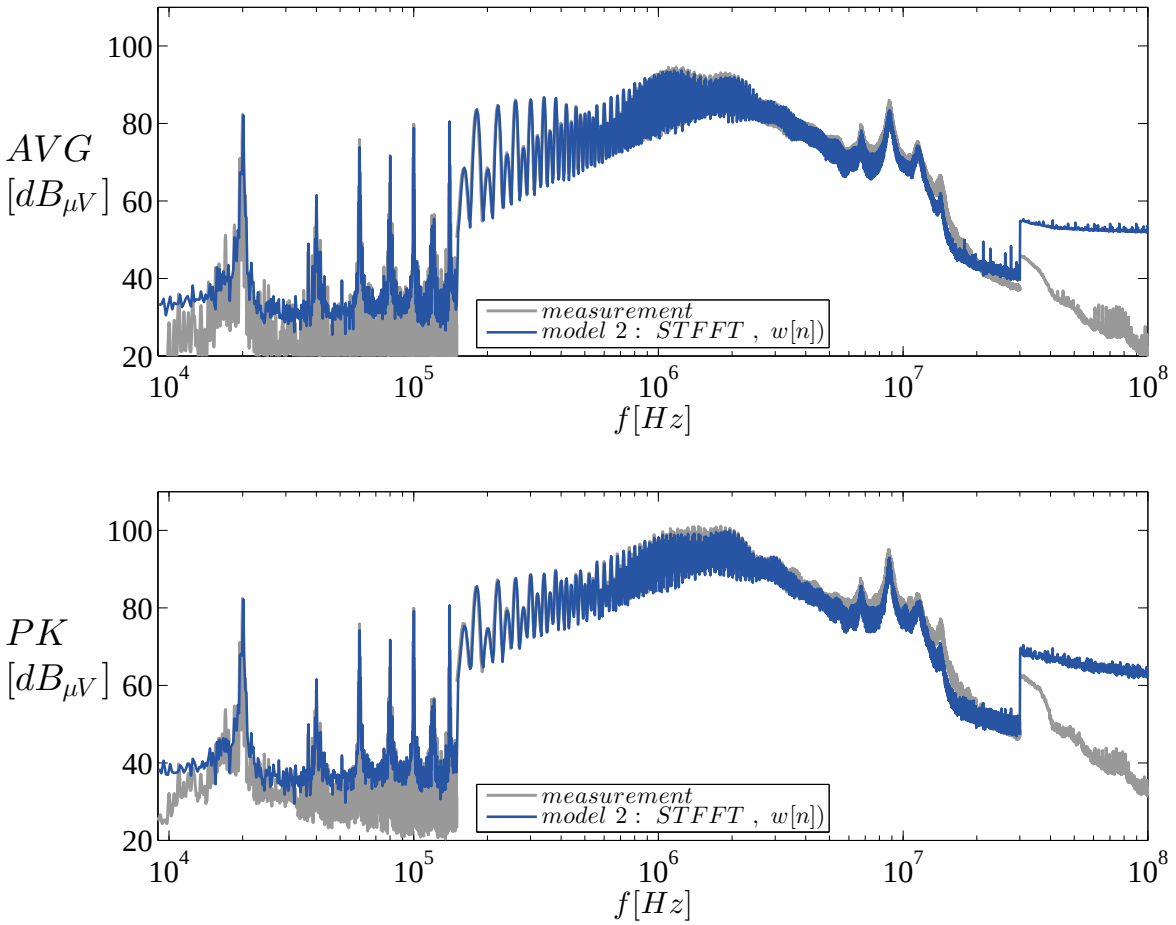

Figure 5.22: Comparison of the measured and the simulated average- and peak detector values of the second approach modeling an EMI receiver

5.2.4 Validation and Comparison of the Derived Models

Considering the simulated detector values of both models, the models show a good accuracy to the real measurement with an EMI measuring receiver in the CISPR bands A and B. However, they greatly deviate in band C. The reason for this effect might be the recorded time sample, as the computation of the detector values in the considered CISPR bands requires both a sufficiently long time sample in band A as well as a good time resolution in band C. Thus, it is a challenge for the available oscillosope. Therefore, a compromise was made which focused on the bands A and B since the derived circuit model reaches its limits in the higher frequency range anyway. Ultimately, the selected record length was chosen to be 20ms with a sampling rate of 500MHz. Another reason which might increase this effect could also be the limited performance of the used oscilloscope in this frequency range itself. Regarding this problem, a further measurement with a focus on the band C with a higher time resolution is adviseable in order to validate the model in the band C as well.

Nevertheless, the STDFT based EMI receiver model shows the best congruency with the measurement result, especially for the peak detector value, of the real EMI receiver. As the mathematical correctness of the detector value calculation in the first modeling approach is difficult to comprehend, this method is outperformed by the STDFT based EMI receiver model. Therefore, the latter is used for all subsequent simulations.

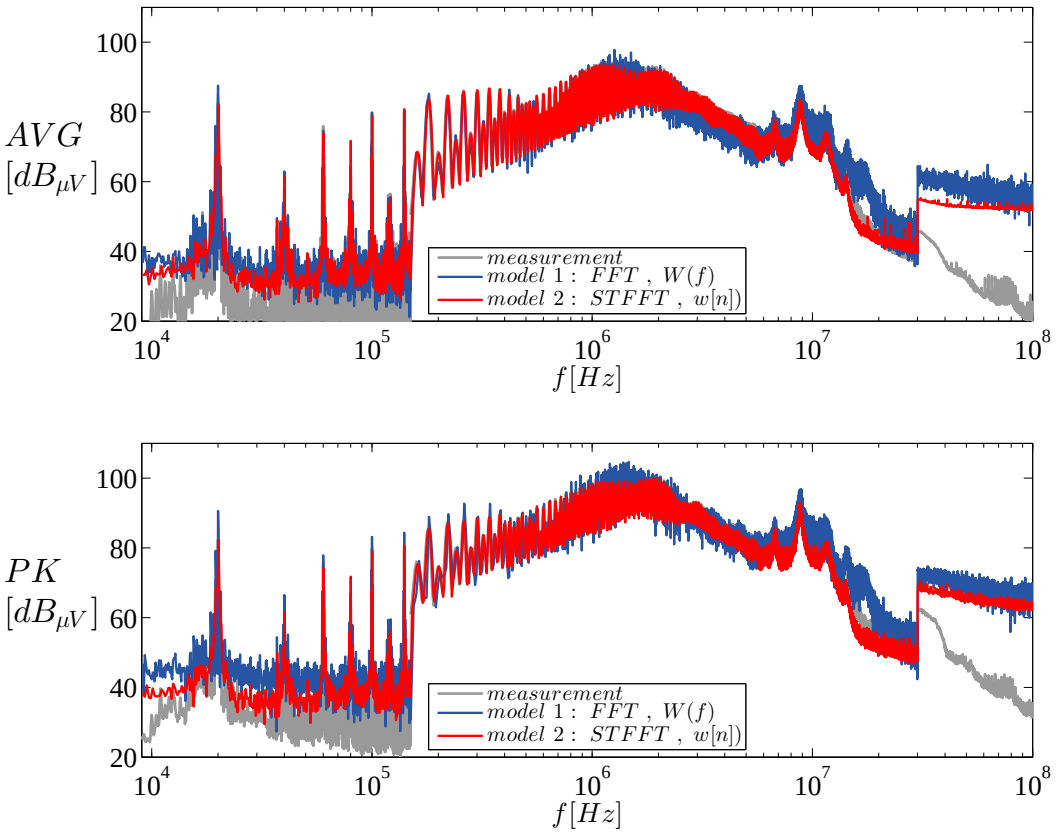

Figure 5.23: Comparison of the derived EMI receiver models (model1: windowing in the frequency domain, model2: windowing in the time domain by the STDFT)

5.3 Overall Sytem Model Validation

The model developed was validated by choosing a certain operating point in which the EUT could be run without an active external cooling system. This should prevent further unintended electromagnetic emissions. Thus, a phase current of $I_{p,set} = 50A$ (RMS) was selected as setpoint for the current control in the EUT.

As the simulation model operates with a constant voltage space vector to save simulation time, the modulation index was chosen to $m_i = 0.105$ that leads to a phase current of 50A (RMS) as well.

Table 5.3 lists the parameter set which was used for the measurement and the simulation.

Figure 5.24 depicts the direct comparison between simulation and measurement in the frequency range between $150kHz$ and $100MHz$ where the CISPR bands A, B and C are involved, while a more detailed overview is provided in figures 5.25, 5.26 and 5.27.

In figures 5.24 - 5.27 some deviations occur between the simulated- and the measured emissions.

The first deviation occurs at the second harmonic of the PWM frequency at $40kHz$. As a center aligned PWM strategy is used in the system one would not assume a significant spectral component at exactly $40kHz$ but only at their side band harmonics around $40kHz$ as the simulation shows (compare figure 3.8).

The greatest deviation, however, appears in a frequency range between $6MHz$ and $15MHz$ and obviously shows an effect which stems from a part of the system which was not taken into account in the simulation model. This effect could be localized by a simple variation of the cable length of the phase connections between inverter and motor. The result was a significant shift of the corresponding resonant frequencies. A satisfactory explanation for that is the very simplified modeling of the PMSM by lumped parameters consisting of the motor inductance and the parasitic capacitances between the motor windings and the motor housing, where an appropriate distribution of theses parameters seems to make sense.

Apart from that, the model is sufficiently accurate in order to be used for the simulation-based analysis of different spread spectrum techniques in chapter 6.

Set Parameters		EUT	Model
DC Link Voltage	U_{DC}	50 V	50 V
PWM Frequency	f_{pwm}	20 kHz	20 kHz
Interlock Time	T_{lock}	2 μs	2 μs
Speed of the Rotating magnetic Field	n_{mot}	10000 rpm	10000 rpm
Fundamental Frequency	f_{el}	500 Hz	500 Hz
Phase Current Setpoint (RMS)	$I_{p,set}$	50 A	-
Modulation Index	m_i	-	0.105

Table 5.3: Parameter set used for the overall model validation

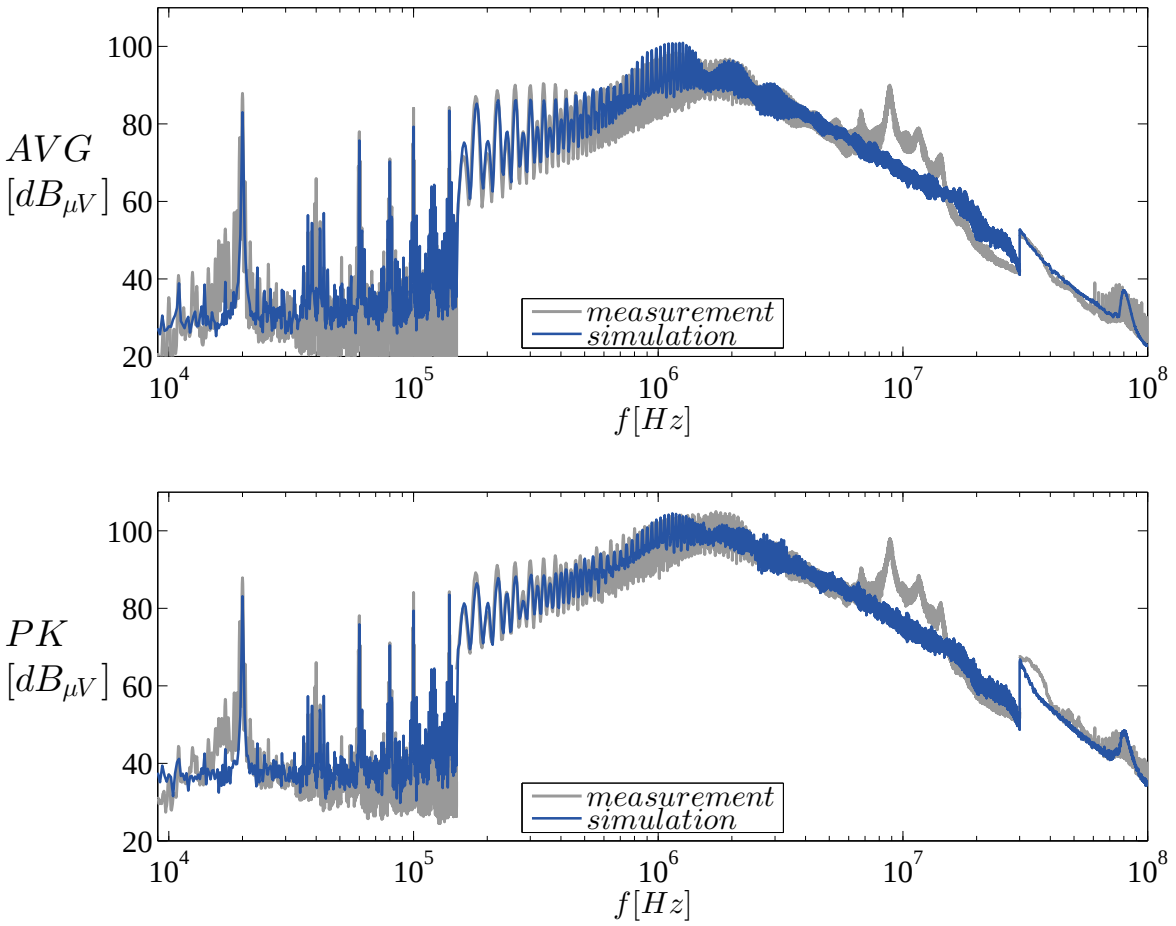

Figure 5.24: Comparison between simulation and measurement of the overall simulation model in the CISPR bands A, B and C

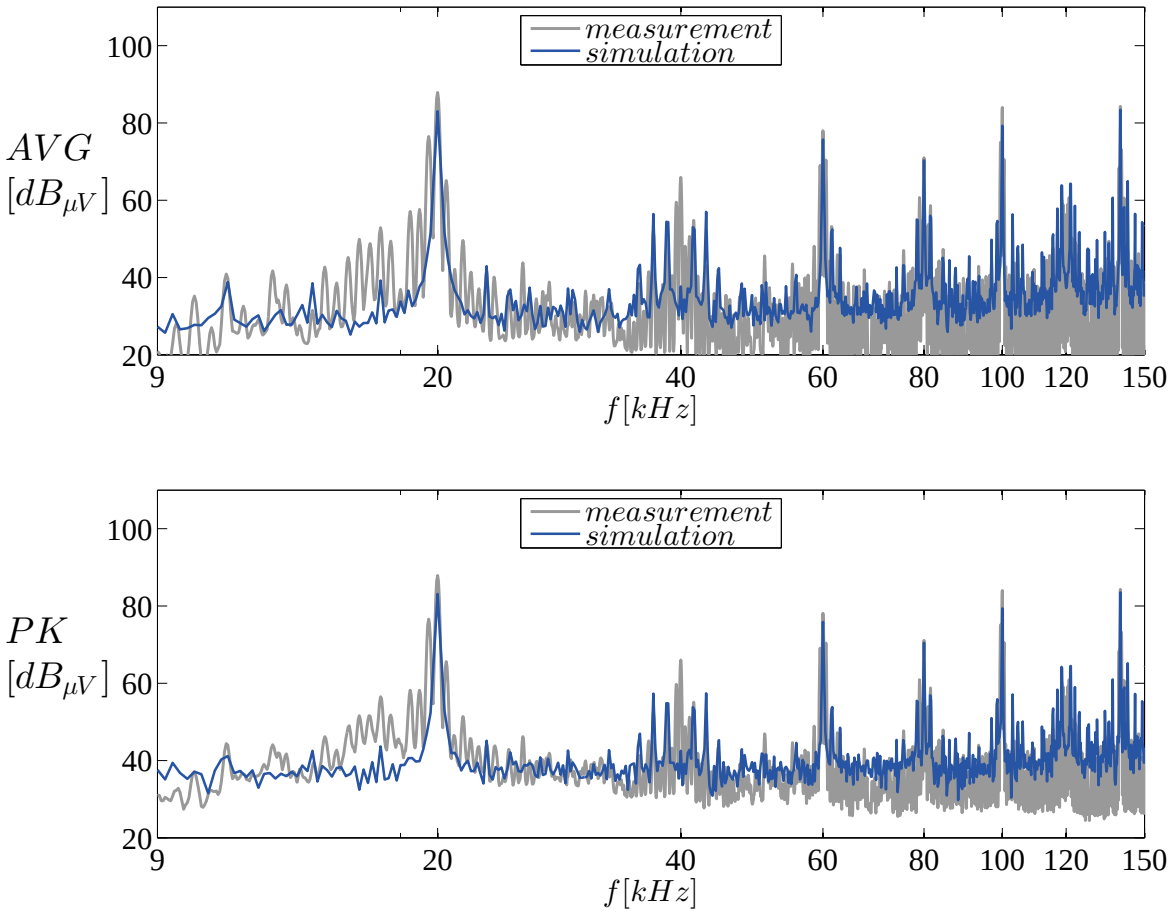

Figure 5.25: Comparison between simulation and measurement of the overall simulation model in the CISPR band A ($RBW = 200Hz$)

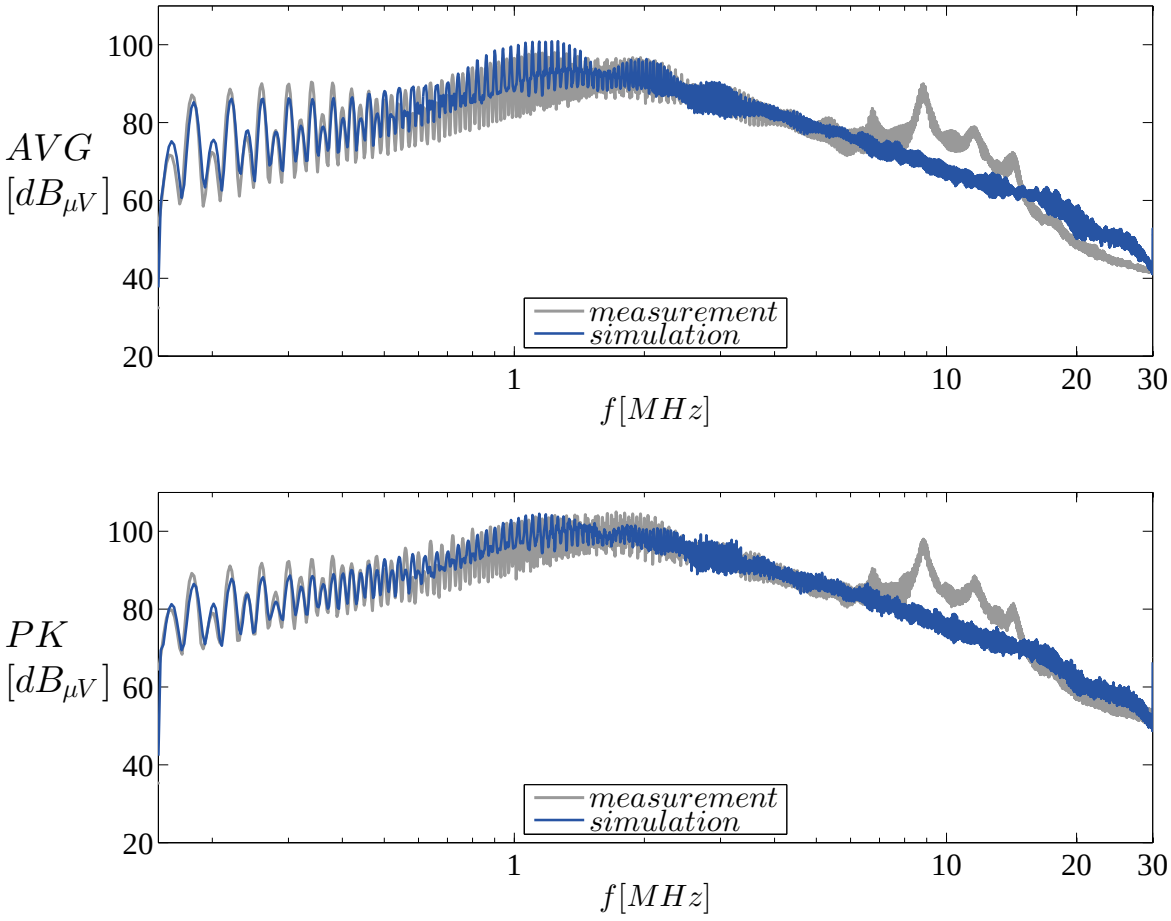

Figure 5.26: Comparison between simulation and measurement of the overall simulation model in the CISPR band B ($RBW = 9kHz$)

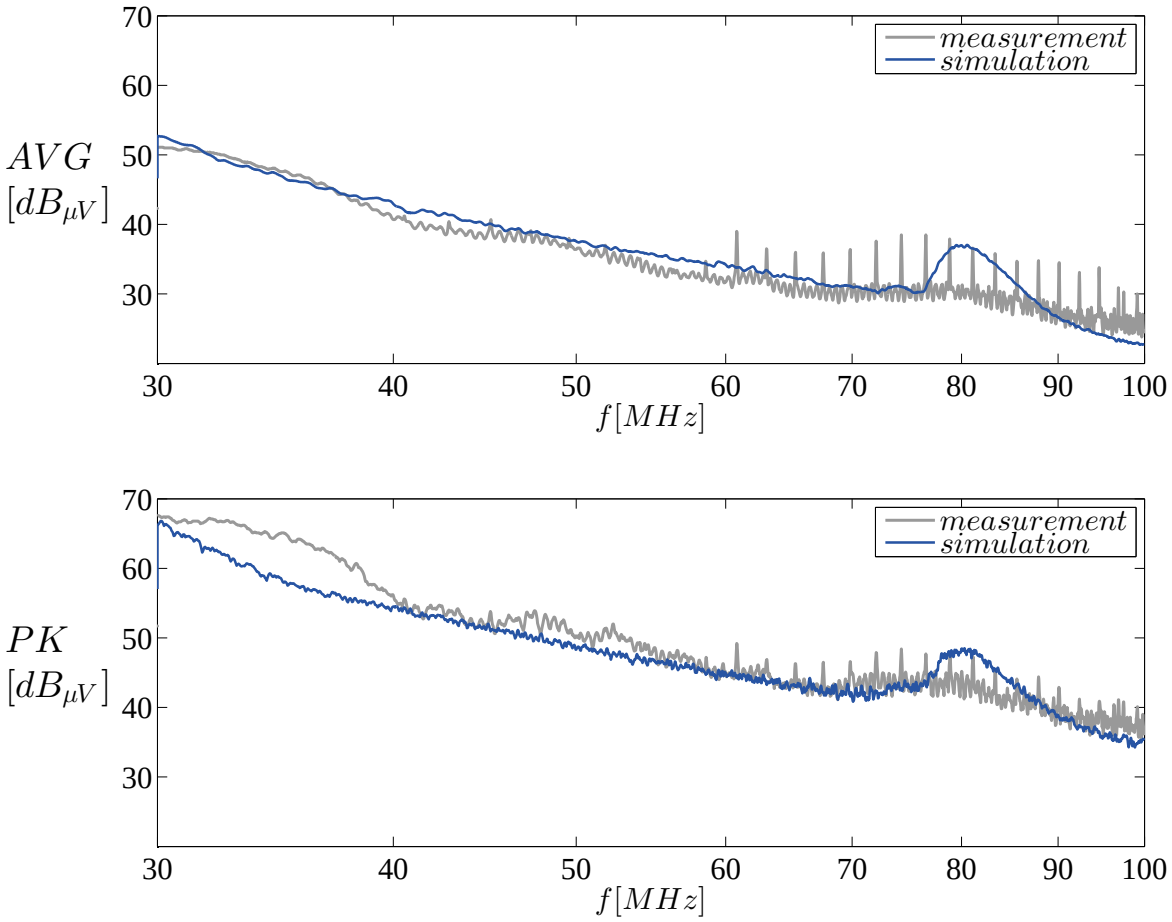

Figure 5.27: Comparison between simulation and measurement of the overall simulation model in the CISPR band C ($RBW = 120kHz$)

Chapter 6

Model Based Analysis of Different Spread Spectrum Techniques

The objective of this chapter is to find out which of the spread spectrum techniques presented in chapter 4 is best suited for minimizing electromagnetic emissions. Consequently, the effect of different techniques on conducted emissions are analyzed by utilizing the simulation model deduced in chapter 5. Therefore, the simulated detector values of both the non-deterministic techniques RPP and RCF as well as the deterministic frequency modulation spread spectrum are compared to each other. In the end, the method which shows the best overall performance regarding average- and peak detector level redcution will be implemented in software as follows in the next chapter 7.

The following simulations were performed by the use of the parameter set in table 5.3. At the same time, the instantaneous spread spectrum parameter is updated each PWM period.

6.1 Non-deterministic Spread Spectrum

In this section, the influence on CE of the key parameters β and Δf_c which correspond to the non-deterministic spread spectrum schemes RPP (randomized pulse position) and RCF (randomized carrier frequency) is demonstrated by varying different parameter values in the simulation.

6.1.1 Randomized Pulse Position Spread Spectrum

Figure 6.1 shows the simulated results for the conducted emission on KL41 by using the parameters $\Delta\beta = 0.05, 0.25$ and 0.4 that define the variance of the pulse position from the pulse center at $\beta = 0.5$ within the PWM cycle.

Considering the lower frequency range in the CISPR band A, there is hardly any improvement visible according to the emission suppression at the fundamental frequency at $20kHz$ even for high values of $\Delta\beta$. From the 3rd harmonic on, however, a good rejection becomes apparent which reaches values of up to $15dB\mu V$ at the 4th, 5th and 6th harmonic for the average detector- and up to $12dB\mu V$ for the peak detector value. Furthermore, the spreading effect becomes clearly evident around the fundamental frequency and their harmonics. There, emissions appear that attain higher values than without the use of spread spectrum.

In the CISPR band B, the suppression of the average detector level only reaches values of about $7dB\mu V$ for frequencies up to approximately $3MHz$ and values of about $2dB\mu V$ in the remaining frequency range up to $30MHz$, where the suppression effect ends in the CISPR band C. Unfortunately, the peak detector values stay almost unchanged or even become slightly higher in the frequency range between $150kHz$ and around $1MHz$.

6.1.2 Randomized Carrier Frequency Spread Spectrum

Figure 6.2 shows the simulated results for the conducted emission on KL41 by using maximum frequency deviations in the range of $\Delta f_c = 1kHz, 2kHz$ and $3kHz$ around the PWM center of $20kHz$.

Considering the emission spectrum, the overall performance of the RCF spread spectrum techique seems to be better than the RPP spread spectrum technique in the entire frequency range.

In the CISPR band A, the emission suppression is already starting at the fundamental frequency and achieves values of around $10dB\mu V$ and $5dB\mu V$ for the average- and the peak detector level. The maximum suppression is attained at the 4th, 5th and 6th harmonic with values up to $19dB\mu V$ and $14dB\mu V$ for the average- and the peak detector value.

Also in the CISPR band B, the average detector's emission reduction attains values of up to $9dB\mu V$ in the frequency range between $150kHz$ and slightly over $1MHz$. In the frequency range between $3MHz$ and $30MHz$, however, the RCF and the RPP spread spectrum techniques show a similar behavior with a suppression of around $2dB\mu V$, where the suppression effect also ends in the CISPR band C. Similar to the RPP spread spectrum technique no reduction of the peak detector emission is noticeable in band B, as the peak detector's envelope reaches equal values than without the use of spread spectrum.

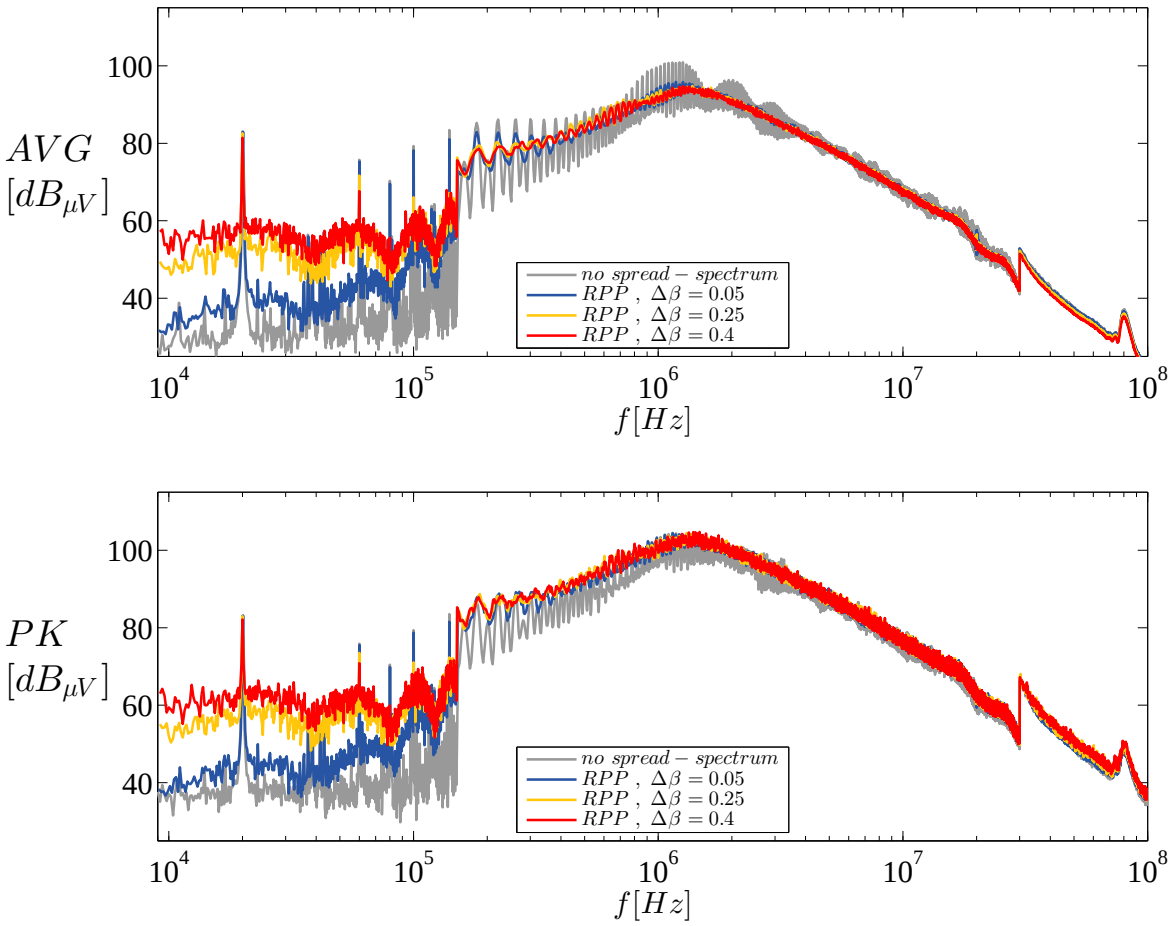

Figure 6.1: Simulation: Impact of pulse position variance $\Delta\beta$ used the RPP spread spectrum for different parameter values of $\Delta\beta$ in the CISPR bands A,B and C

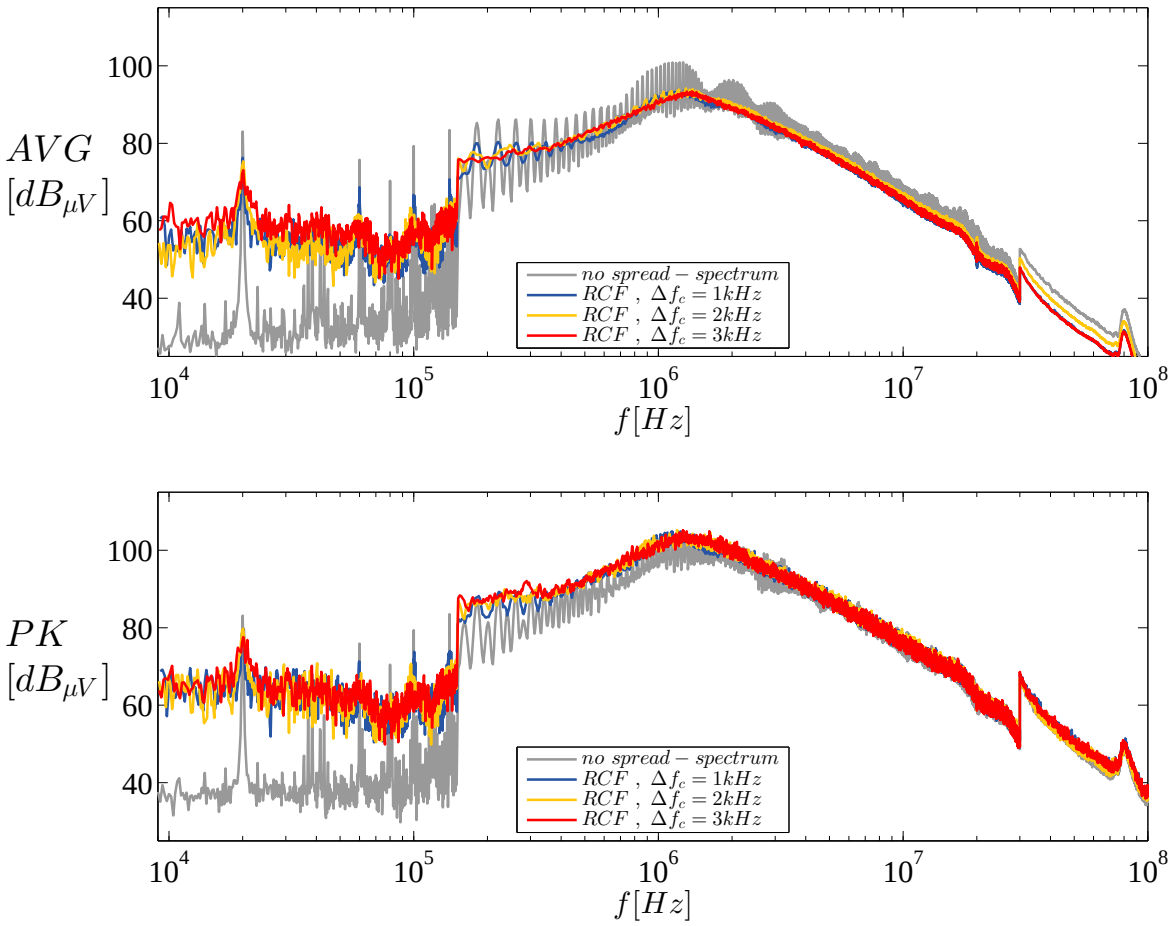

Figure 6.2: Simulation: Impact of the frequency deviation Δf_c used the RCF spread spectrum for different parameter values of Δf_c in the CISPR bands A,B and C

6.2 Deterministic Spread Spectrum

In this section the impact of the key parameters Δf_c (maximum frequency deviation), f_m (modulation frequency) and the modulation profile on the average- and the peak-detector values are shown by varying the parameters separately while the others are kept at selected and constant values. As stated in the conclusion in 4.3, the deterministic spread spectrum technique provides more possibilities when it comes to systematically affecting the average- and the peak detector value of an EMI receiver, which will be shown at the end of this section.

6.2.1 Influence of the Frequency Deviation Δf_c

In order to allow a good comparison with the non-deterministic RCF spread spectrum scheme with respect to their attained performance, the same frequency deviations of $\Delta f_c = 1kHz, 2kHz$ and $3kHz$ are chosen. Additionally, the modulation frequency was set to a constant value of $f_m = 50Hz$ while a triangular modulation shape was used in the simulation.

Considering the resulting simulated average- and peak emission spectra in figure 6.3 and figure 6.4, the analogy to the related RCF spread spectrum scheme becomes apparent since a similar behavior in the anaylzed frequency range is achieved.

It is clearly noticeable, that a very good distribution of the spectral energy is achieved in the CISPR band A. This results in a high suppression of the average emission which reaches values of around $20dB\mu V$ for the fundamental frequency and the 3rd, 4th, 5th and 6th harmonic. At the same time, the peak detector level can be reducted to approximately $9dB\mu V$.

In the CISPR band B, the average detector level reduction reaches values of up to $8dB\mu V$ in the frequency range between $150kHz$ and around $1MHz$. Even from $3MHz$ on to $30MHz$, a reduction of $2dB\mu V$ is noticeable. The spreading effect also ends in the CISPR band C, similar as in the previously discussed non-deterministic spread spectrum schemes.

However, the peak detector shows values that are equal or higher than without the use of spread spectrum. Especially for high frequency deviations, the peak emissions envelope can exceed the original values by even $5dB\mu V$. The reason for this phenomenon was already presented in 4.2.1 and is caused by the resulting overlap of the harmonics' envelope, depending on the frequency deviation used.

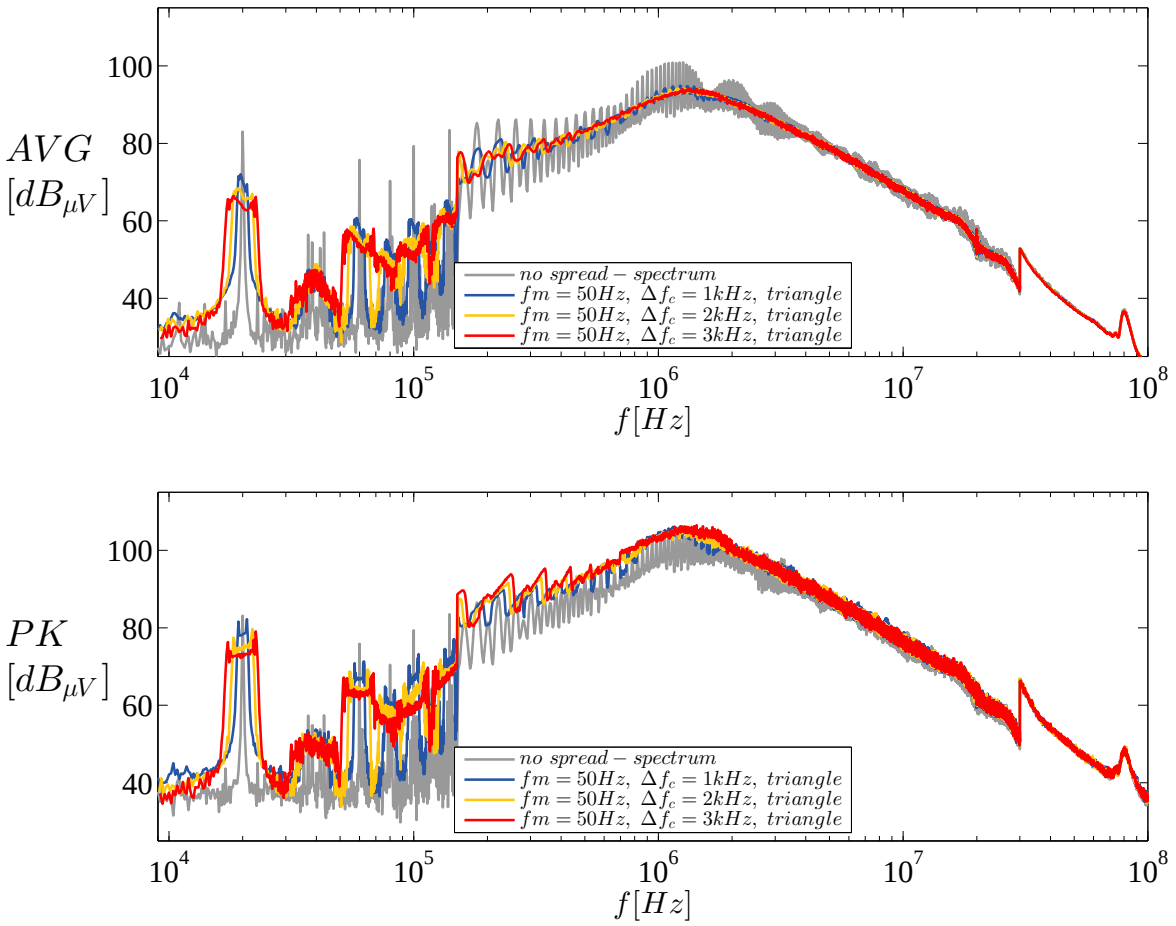

Figure 6.3: Simulation: Impact of the frequency deviation Δf_c used in deterministic spread spectrum techniques on the average- and peak- emission spectra in the CISPR bands A,B and C for a modulation frequency of $f_m = 50Hz$ and a triangular modulation profile

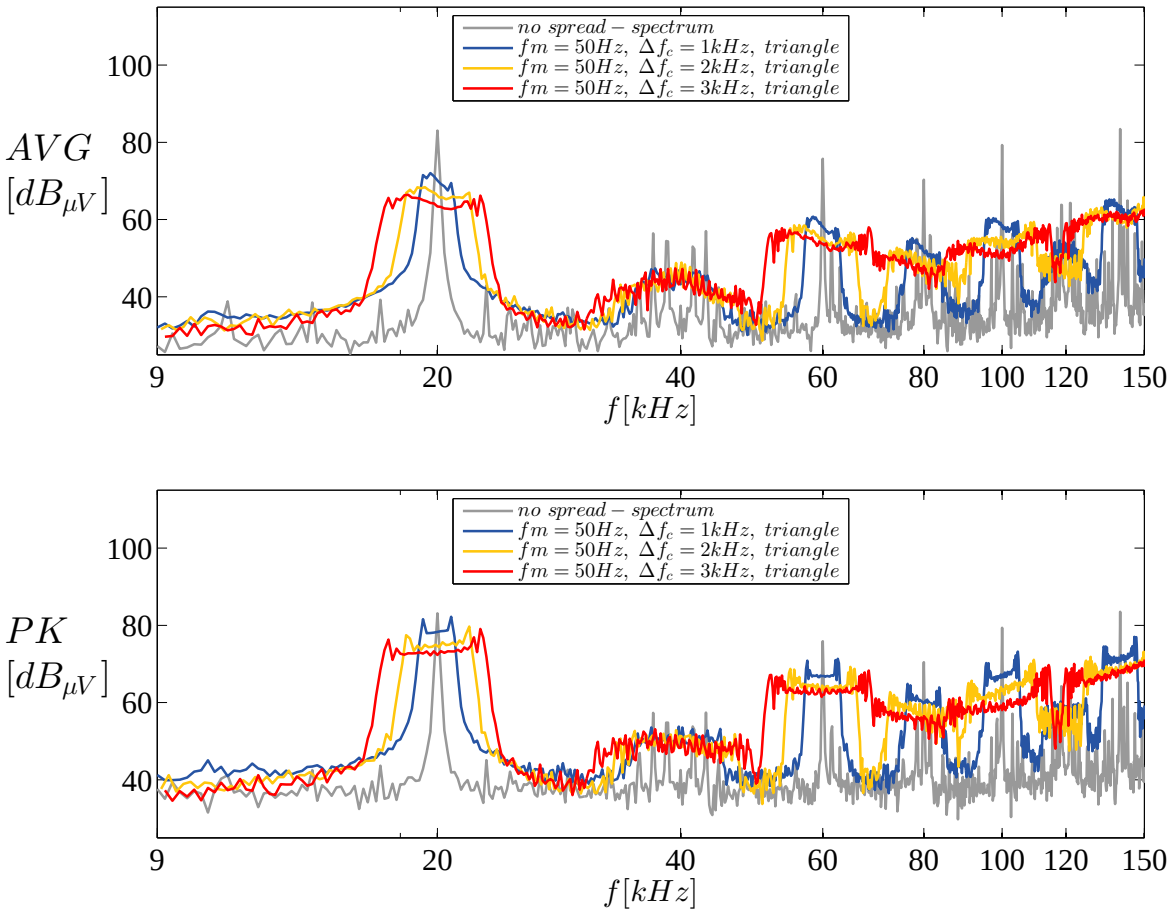

Figure 6.4: Simulation: Impact of the frequency deviation Δf_c used in deterministic spread spectrum techniques on the average- and peak- emission spectra in the CISPR band A

6.2.2 Influence of the Modulation Frequency f_m

In this section, the influence of the modulation frequency f_m on the average- and the peak detector values will be demonstrated by varying f_m between $50Hz$, $1kHz$ and $2kHz$ whereby the frequency deviation was set to a constant value of $\Delta f_c = 2kHz$ and a triangular modulation profile was applied.

Figure 6.5 shows the simulation results in the CISPR bands A, B and C while figures 6.6 and 6.7 provide a more detailed representation in the CISPR bands A and B.

Considering the CISPR Band A, the simulation for $f_m = 50Hz$ shows a continuous emission spectrum outline whereas the simulations with $f_m = 1kHz$ and $2kHz$ result in a discrete frequency spectrum. An explanation for this is the relation between f_m and the used resolution bandwidth RBW of the EMI measuring receiver. As the spacing between the spectral components is defined by the modulation frequency (see 4.2.2), always four spectral magnitude components will fall within the 6dB bandwidth of $RBW = 200Hz$ in the CISPR band A when a modulation frequency of $f_m = 50Hz$ is used. This leads to a smoothing of the spectrum outline. In contrast, modulation frequencies higher than the RBW yield discrete frequency spikes. Regarding the detector levels, a better emission reduction can be established by lower modulation frequencies, especially for the average detector.

In the CISPR band B, different parameters for f_m barely influence the average detector level and attain similar emission reductions. However, higher values of f_m lead to lower peak emission levels which more or less comply with those where no spread spectrum is applied.

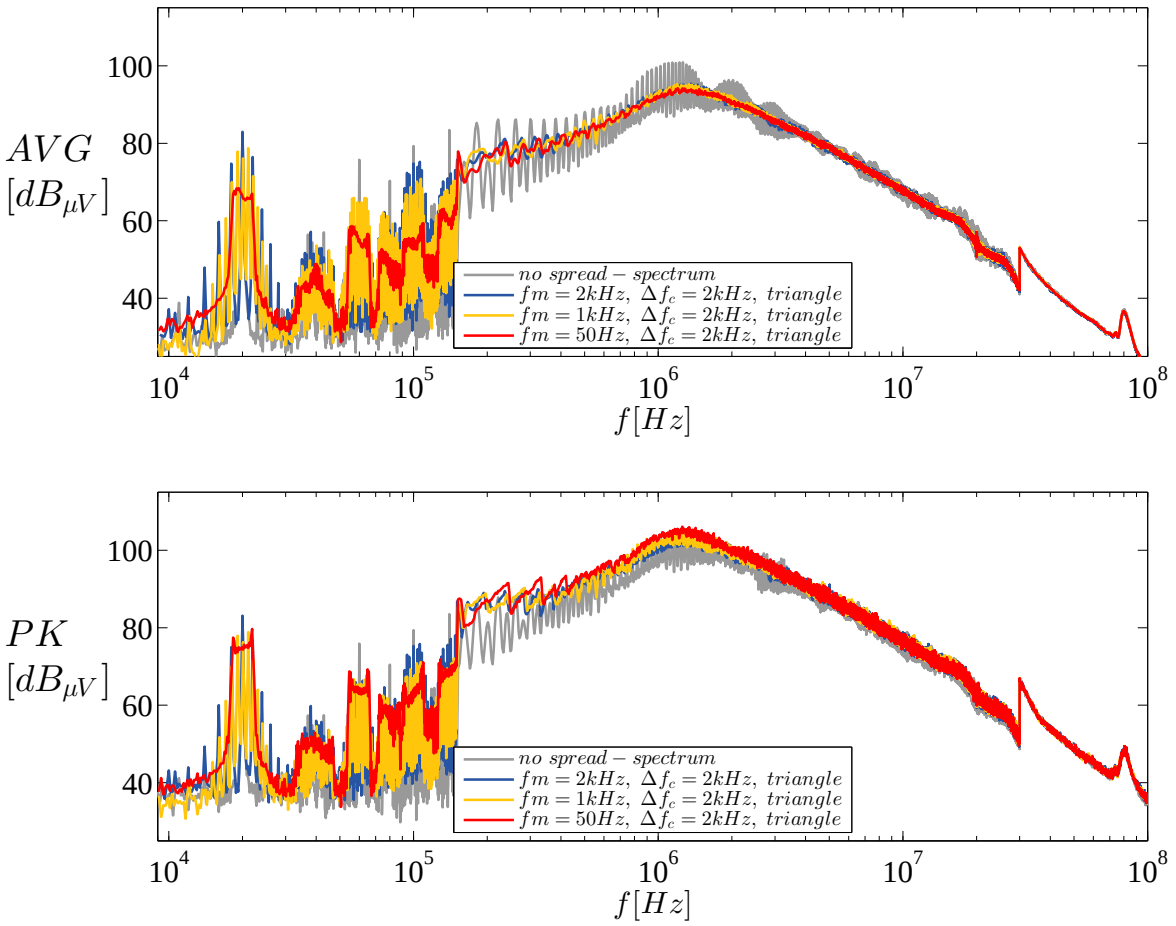

Figure 6.5: Simulation: Impact of the modulation frequency f_m used in deterministic spread spectrum techniques on the average- and peak- emission spectra in the CISPR bands A,B and C

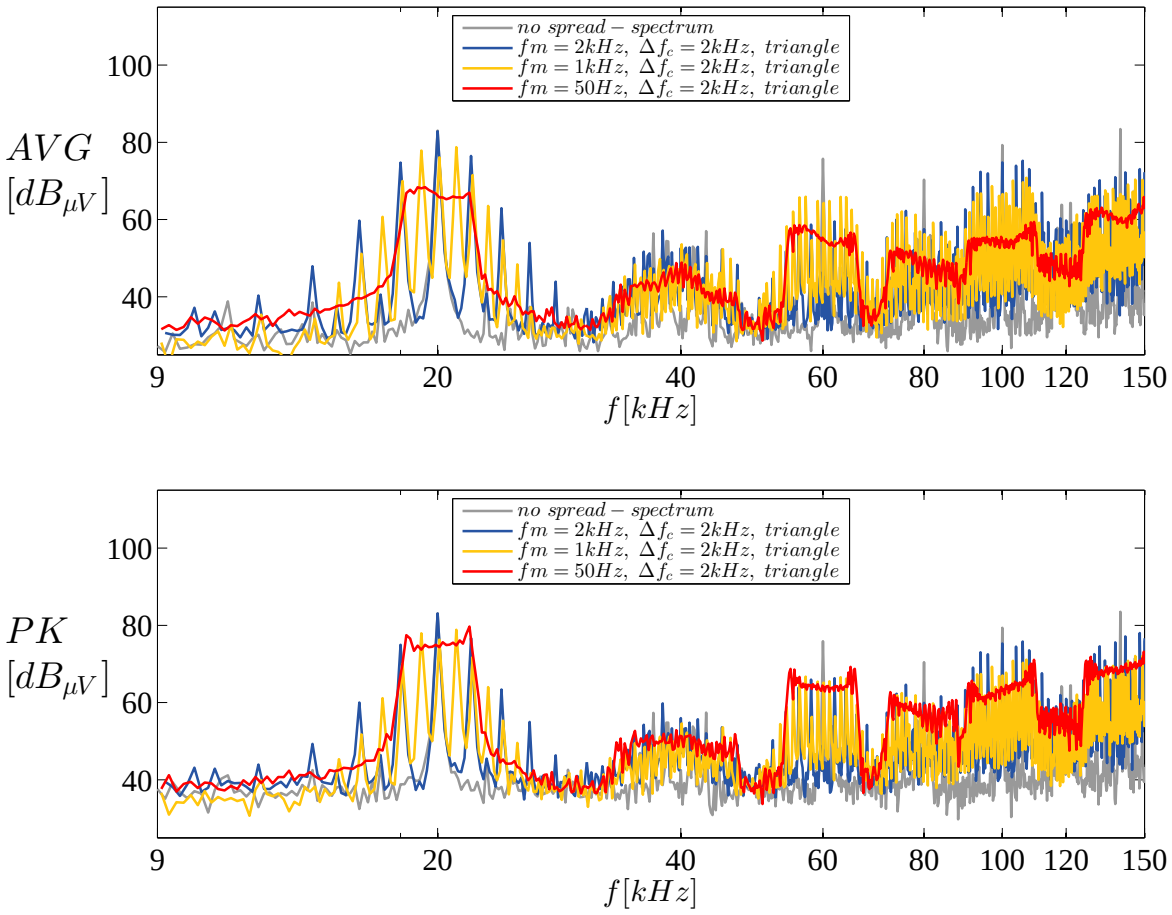

Figure 6.6: Simulation: impact of the modulation frequency f_m used in deterministic spread spectrum techniques on the average- and peak- emission spectra in the CISPR band A

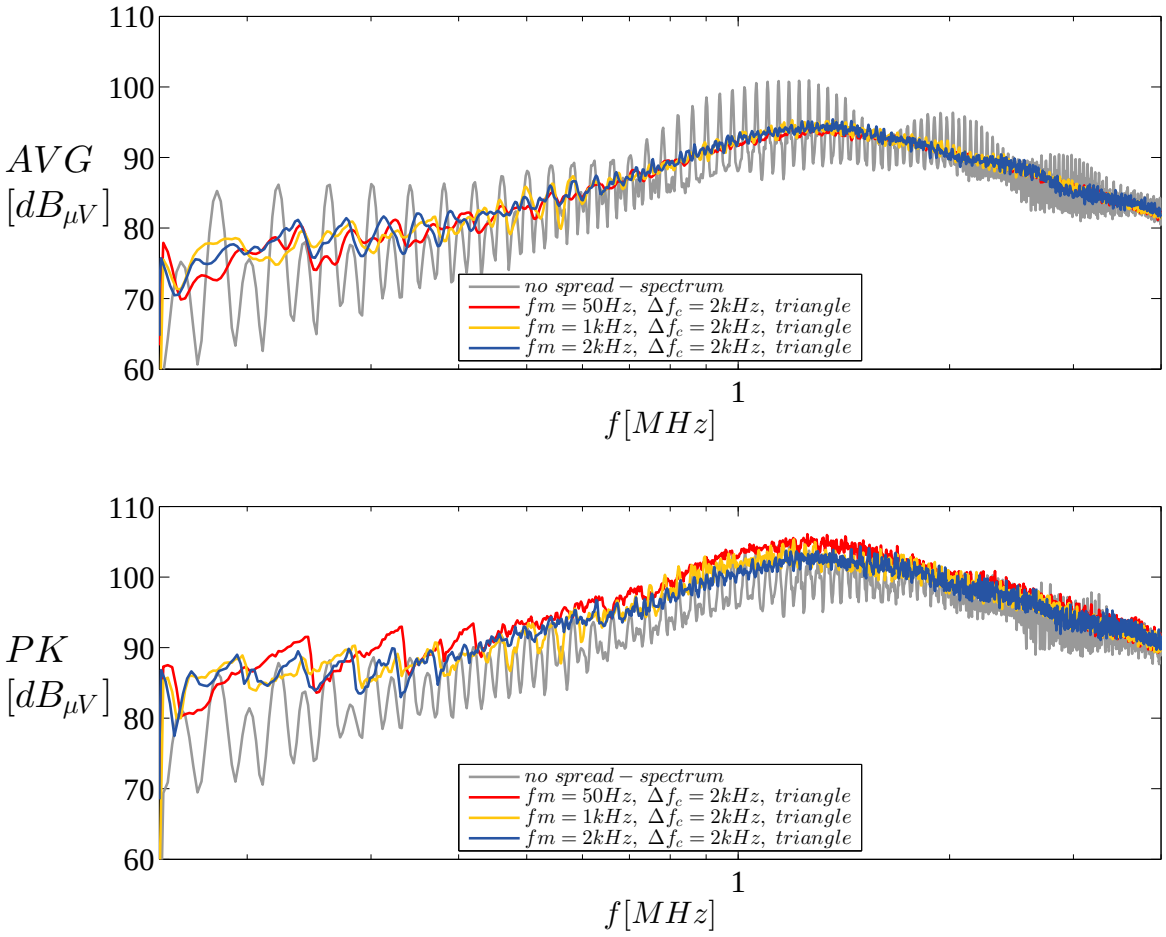

Figure 6.7: Simulation: Impact of the modulation frequency f_m used in deterministic spread spectrum techniques on the average- and peak- emission spectra in the CISPR band B and a frequency range between 150kHz and 4MHz

6.2.3 Influence of the Modulation Profile

To understand the effects of different modulation profiles on the emission spectra, the frequency deviation was set to $\Delta f_c = 2kHz$ and the modulation frequency to $f_m = 50Hz$. Consequently, a continuous spectrum outline and thus a better visualization of the obtained results as explained in section 6.2.2 is achieved.

Figure 6.8 shows the simulated emissions for the sine-, triangle-, sawtooth (up-ramp) and the Hershey-Kiss^{TM}modulation profile (Nr. 3 in figure 4.8) in the CISPR band A, B and C. Figure 6.9 provides a more detailed representation in the CISPR band A.

Considering the simulated emission spectra, the choice of the modulation profile obviously has a smaller impact on the emission level than the parameters Δf_c and f_m and reflects the findings already explained in 4.2.3.

In the CISPR band A, the sawtooth profile (up-ramp) attains the flattest top of the spectrum outline. Therefore, it leads to the best results regarding an emission reduction, especially for the average detector. On the contrary, the sinusoidal profile seems to be an unfavourable choice in the CISPR band A since the emission level at frequencies that correspond to the peak excursions of the PWM frequency reach the highest levels.

However, in the CISPR band B, there is hardly any noticeable difference between the different modulation profiles if only the spectrums' outlines are taken into account.

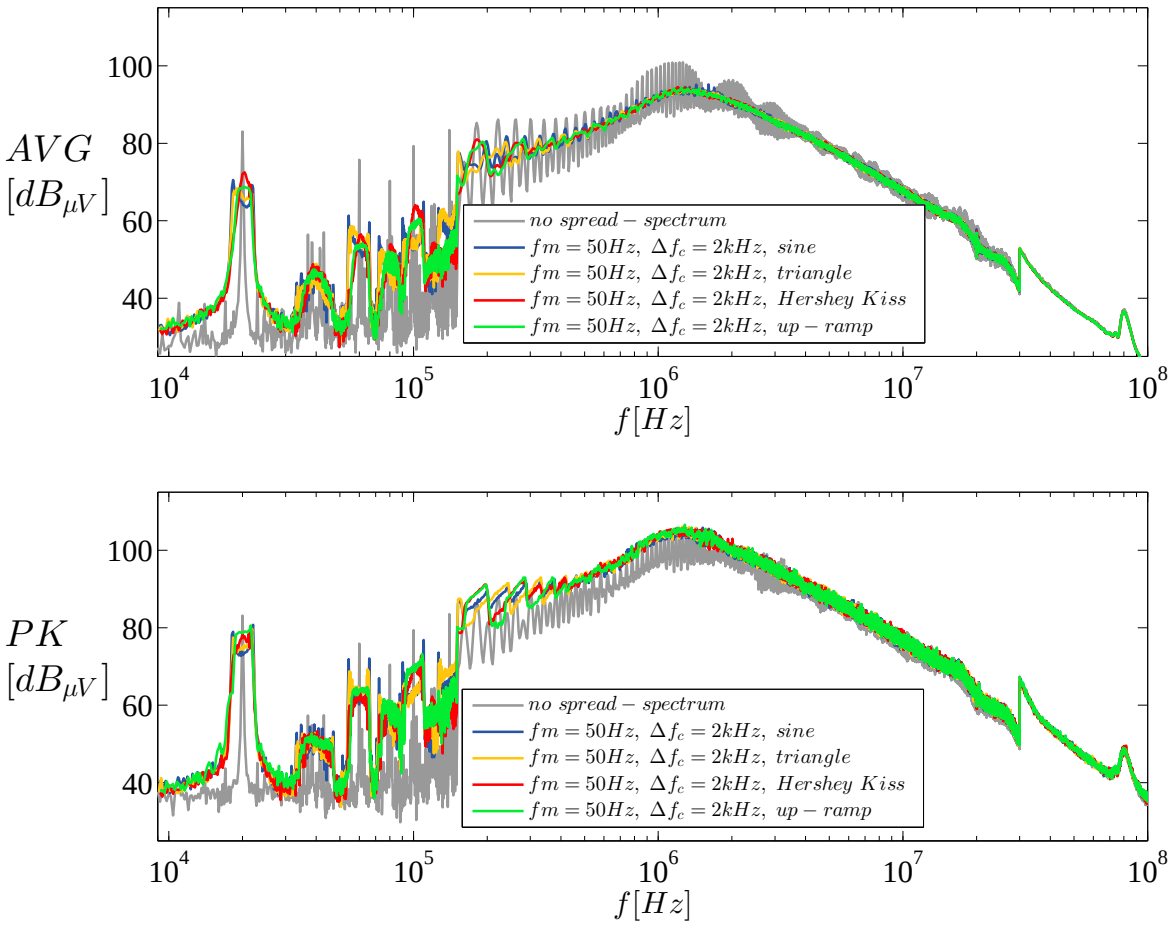

Figure 6.8: Simulation: Impact of the modulation frequency f_m used in deterministic spread spectrum techniques on the average- and peak- emission spectra in the CISPR bands A,B and C

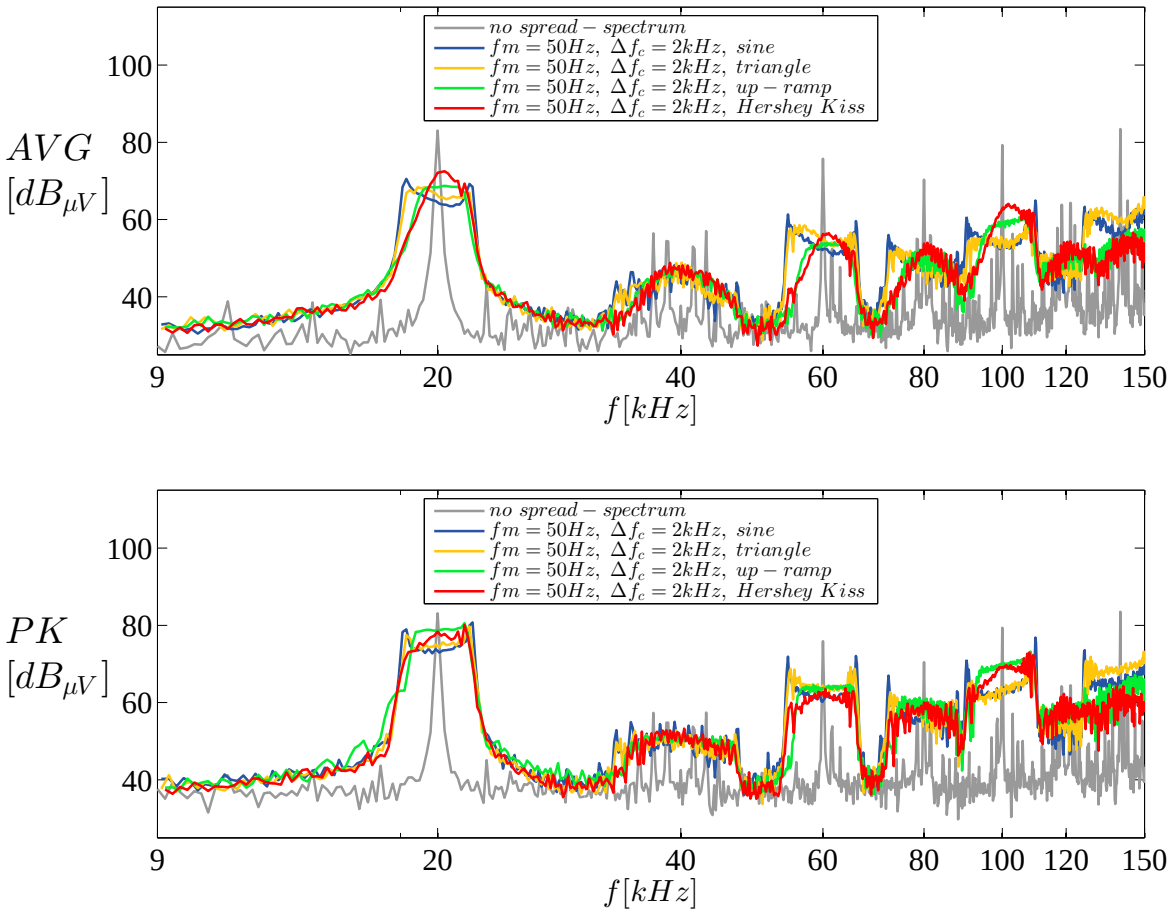

Figure 6.9: Simulation: Impact of the modulation frequency f_m used in deterministic spread spectrum techniques on the average- and peak- emission spectra in the CISPR band A

6.2.4 Systematic Reduction of the Detector Levels

As already demonstrated in the last chapters, an independent analysis of the presented parameters is not possible. This makes the determination of suitable parameters more difficult, in particular when different RBWs of the measuring receiver have to be considered at the same time.

In general, deeper knowledge about the theory of modulation as well as the presented operating principle of EMI measuring receivers is helpful in order to find a good parameter combination of Δf_c and f_m. Since most of the energy in frequency modulated signals is located in the so-called *Carson's bandwidth* ($CBR = 2(\Delta f_c + f_m)$, [20], [8]) the combination of f_m and Δf_c defines how much signal energy falls within the reception channel RBW of the measuring receiver. This fact can in turn be utilized for optimizing either the average- or the peak detector value for a certain RBW depending on the analyzed CISPR band.

For example, if the approach for the peak-detector calculation in section 5.2.2 (figure 5.17) is considered, a lower modulation frequency causes the summation of a higher number of spectral components and further results in higher peak detector readings.

On the contrary, the closer clustering of the frequency spectral components for lower modulation frequencies leads to the fact that more spectral components with lower magnitudes are included in the averaging as well. Hence, lower average detector readings will be the achieved.

For this reason, there are two basic design decisions in which both extremes are carried out in the simulation depicted in figure 6.10. The first parameter combination of $f_m = 50Hz$ and $\Delta f_c = 2kHz$ aims at the reduction of the average detector levels in the bands A and B by using a modulation frequency significantly lower than the resolutions bandwidths $RBW_A = 200Hz$ and $RBW_B = 9kHz$. Additionally, a good reduction of the peak emission in band A can be achieved with the problem that the peak detector unfortunately attains a higher level than without using spread spectrum.

Therefore, the second parameter combination of $f_m = 5kHz$ and $\Delta f_c = 2kHz$ tends to limiting the peak detector emission in the band B by selecting a modulation frequency that is in the same range as the resolution bandwidth of $RBW_B = 9kHz$. In general, an ideal modulation frequency suppressing the peak detector level would be higher than the used resolution bandwidth. However, the simulations have shown that a modulation frequency of, for example, $f_m = 11kHz$ does not lead to a further improvement. This can be explained by the nominal PWM frequency that is also located in the same range at $20kHz$ that would more or less result in toggling between two frequencies.

A higher value for f_m may also lead to a good average detector level reduction in band B as well, but significantly reduces the emission reduction in band A. Hence, the actual parameter combination has to be tuned according to the point where most problems occur in the system regarding EME.

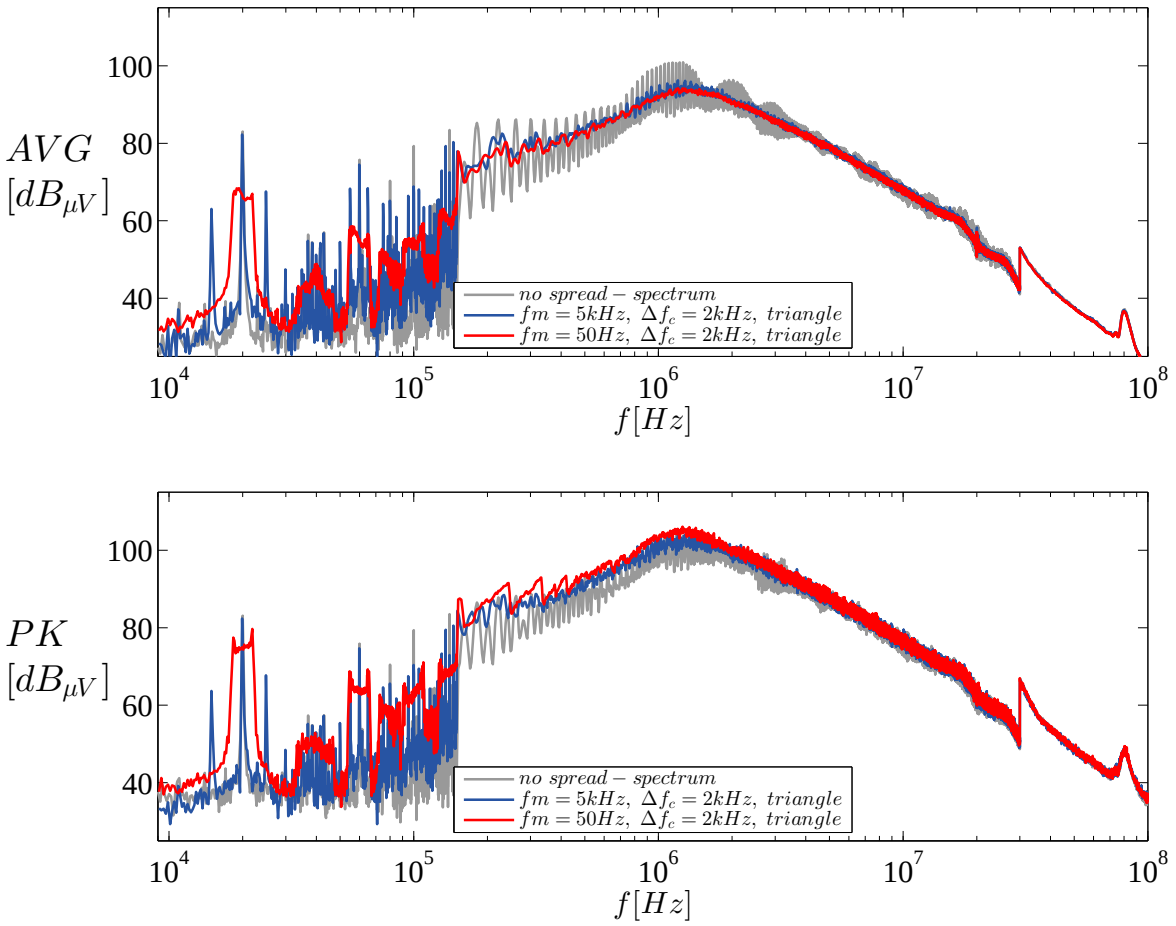

Figure 6.10: Simulation: Systematic reduction of the average- and the peak detector levels by the utilization of different parameter configurations of f_m and Δf_c

Chapter 7

Implemenation, Measurement and Validation of Selected Spread Spectrum Techniques

As the simulation results showed in the last chapter, the non-deterministic randomized carrier frequency spread spectrum (RCF) and the deterministic frequency modulation spread spectrum scheme seem to be the most effective and promising approaches for an emission reduction in a wide frequency range. Since both schemes underlie the same spreading mechanism by varying the the PWM frequency in each PWM cycle, the implementation was narrowed to these two techniques. In order to subsequently validate the obtained simulation results by a conducted emission measurement at the real EUT, all techniques (except the RPP scheme) were carried out and measured by the use of the same spread spectrum parameters presented in chapter 6 and the system parameters in table 5.3.

Because the influences of the different spread spectrum techniques and their parameters have already been explained in detail in the simulative part in chapter 6, the explainings in this chapter will be limited to only a few statements about where deviations between the simulated and the measured emissions are noticeable and/or notable.

A direct comparison between simulations performed and the corresponding measurements is provided in appendix B.

7.1 Non-deterministic / Randomized Carrier Frequency Spread Spectrum

Figure 7.1 shows the measured results for the conducted emission on KL41 by allowing maximum frequency deviations in the range of $\Delta f_c = \pm 1kHz, 2kHz$ and $3kHz$ around the nominal PWM frequency of $20kHz$. (see corresponding simulation results in figure 6.2)

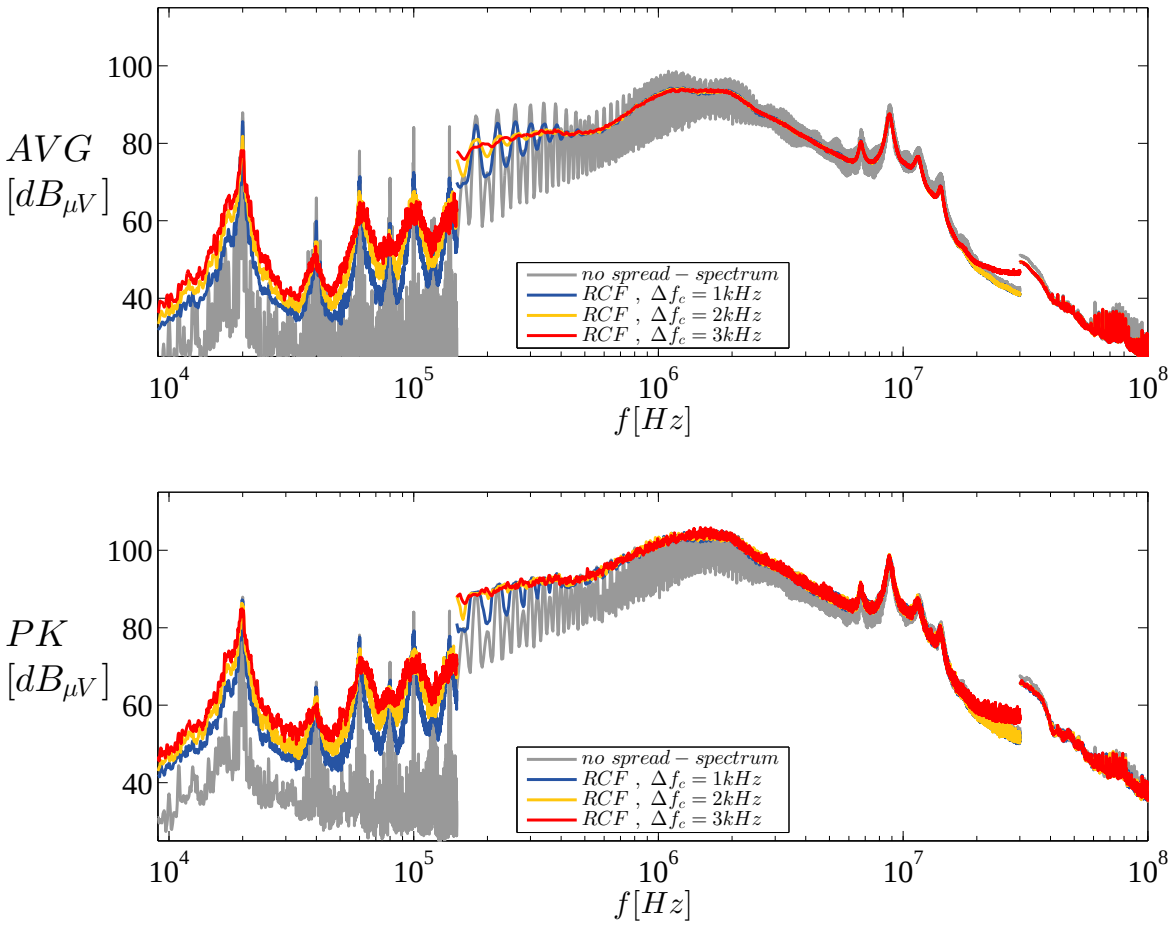

Figure 7.1: Measurement: Impact of the frequency deviation Δf_c used the RCF spread spectrum for different parameter values of Δf_c in the CISPR bands A,B and C

7.2 Deterministic Spread Spectrum

The following sections comprise the individual observation of the spread spectrum parameters Δf_c, f_m and the modulation profile used in deterministic spread spectrum techniques.

7.2.1 Influence of the Frequency Deviation Δf_c

Figures 7.2 and 7.3 show the measured results for the conducted emission on KL41 in the CISPR band A,B and C by using the frequency deviations $\Delta f_c = 1kHz, 2kHz$ and $3kHz$, while the modulation frequency was set to a constant value of $f_m = 50Hz$ and a triangular modulation profile was applied. (see corresponding simulation results in figures 6.3 and 6.4)

7.2.2 Influence of the Modulation Frequency f_m

Figures 7.4, 7.6 and 7.5 show the measured results for the conducted emission on KL41 in the CISPR bands A,B and C by varying f_m between $50Hz$, $1kHz$ and $2kHz$, while the frequency deviation was set to a constant value of $\Delta f_c = 2kHz$ and a triangular modulation profile was applied. (see corresponding simulation results in figures 6.5, 6.6 and 6.7)

7.2.3 Influence of the Modulation Profile

Figure 7.7 shows the measured emissions for the sine-, triangle-, sawtooth (up-ramp) and the Hershey-Kiss^{TM}modulation profile (Nr. 3 in figure 4.8) in the CISPR band A, B and C, while figure 7.8 provides a more detailed representation in the CISPR band A. (see corresponding simulation results in figures 6.8 and 6.9)

7.2.4 Systematic Reduction of the Detector Levels

Figure 7.9 illustrates the systematic reduction of the average detector level in the CISPR bands A and B by using a modulation frequency of $f_m = 50Hz$ and the systematic reduction of the peak detector level in the CISPR band B by using a modulation frequency of $f_m = 5kHz$. In both cases a frequency deviation of $\Delta f_c = 2kHz$ and a triangular modulation profile was used. (see corresponding simulation results in figure 6.10)

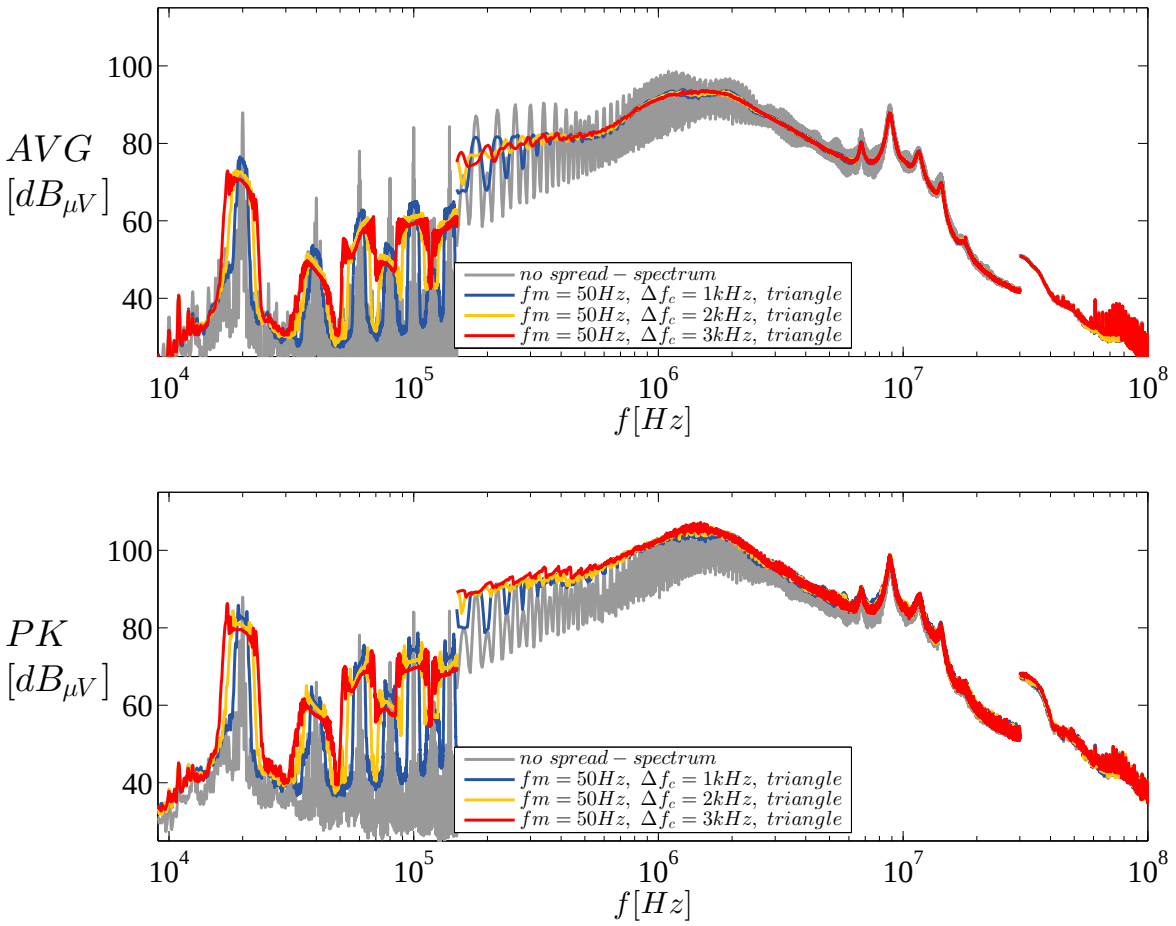

Figure 7.2: Measurement: Impact of the frequency deviation Δf_c in deterministic spread spectrum techniques on the average- and peak-emission spectra in the CISPR bands A,B and C for a modulation frequency of $f_m = 50Hz$ and a triangular modulation profile

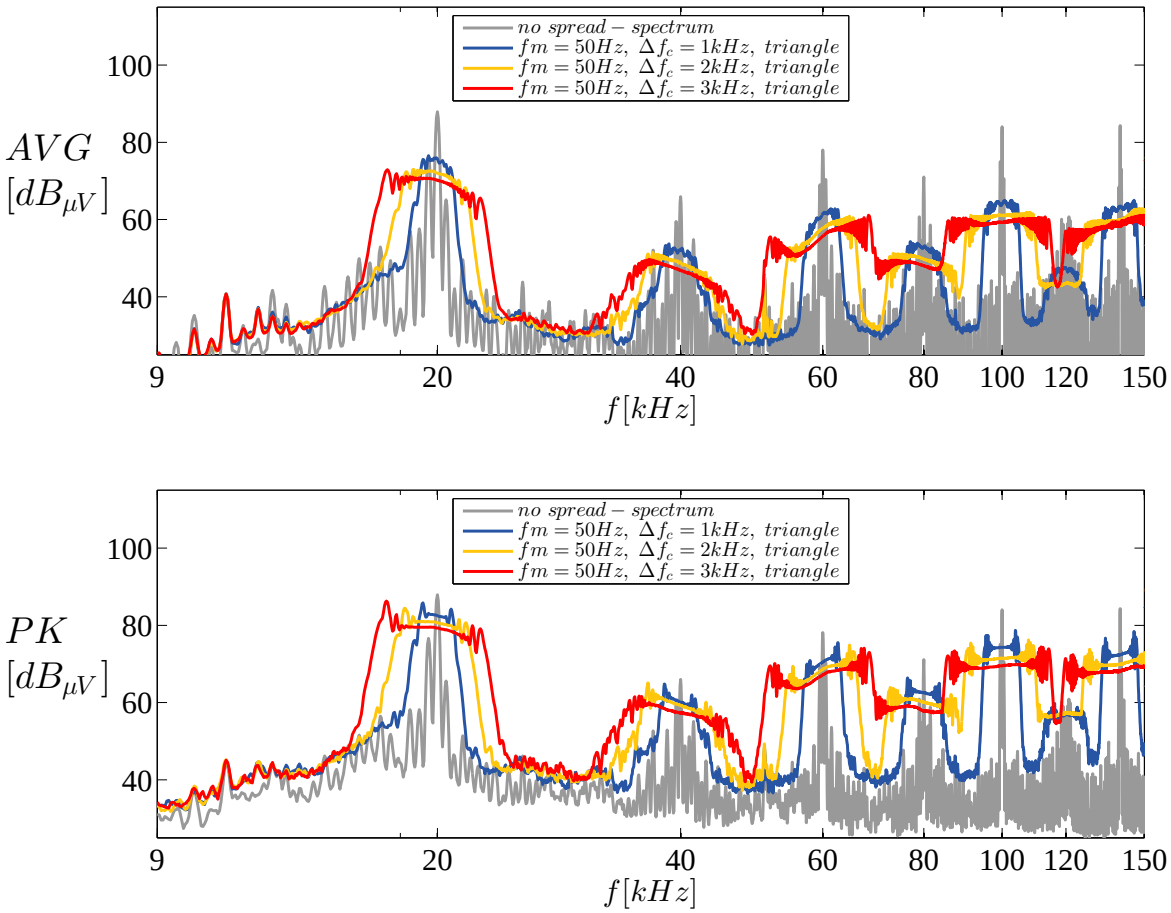

Figure 7.3: Measurement: Impact of the frequency deviation Δf_c used in deterministic spread spectrum techniques on the average- and peak-emission spectra in the CISPR band A

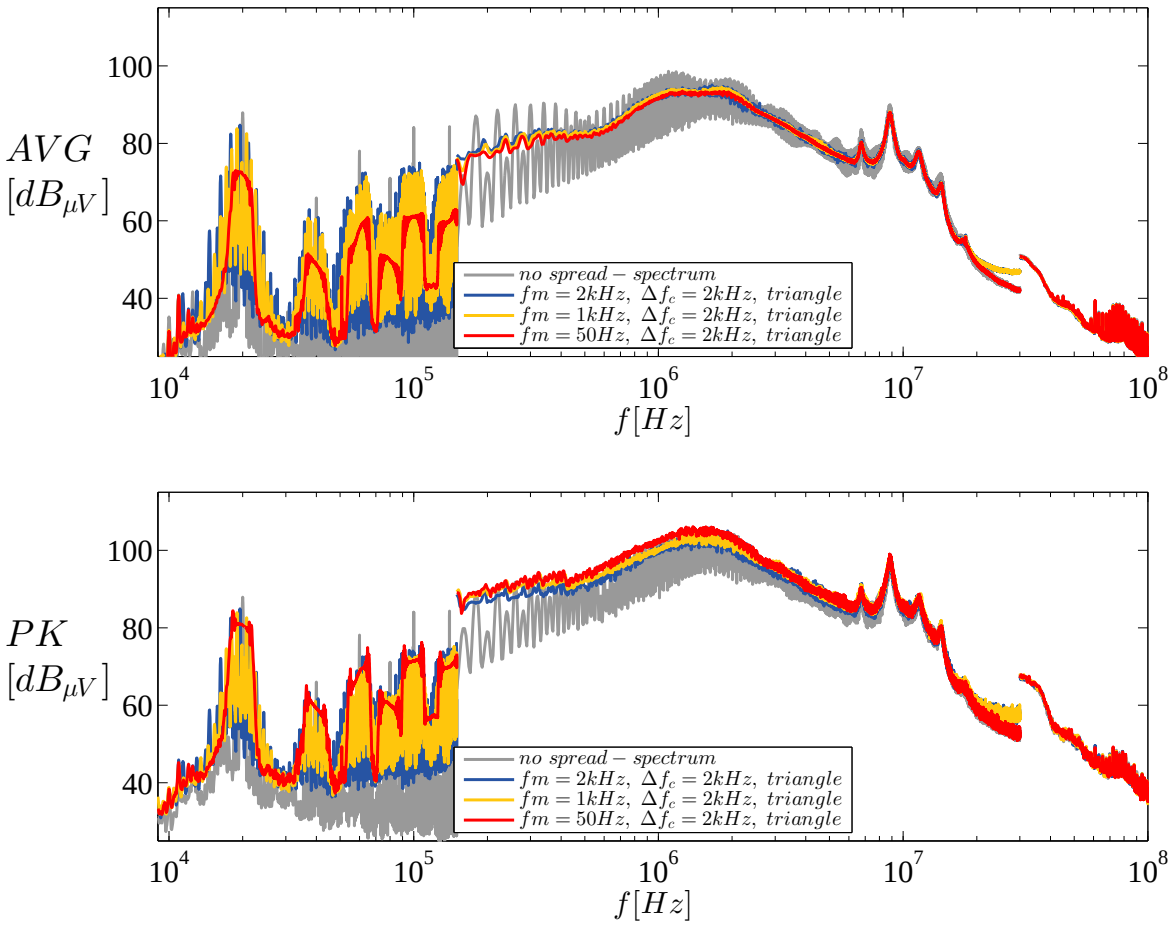

Figure 7.4: Measurement: Impact of the modulation frequency f_m used in deterministic spread spectrum techniques on the average- and peak-emission spectra in the CISPR bands A,B and C

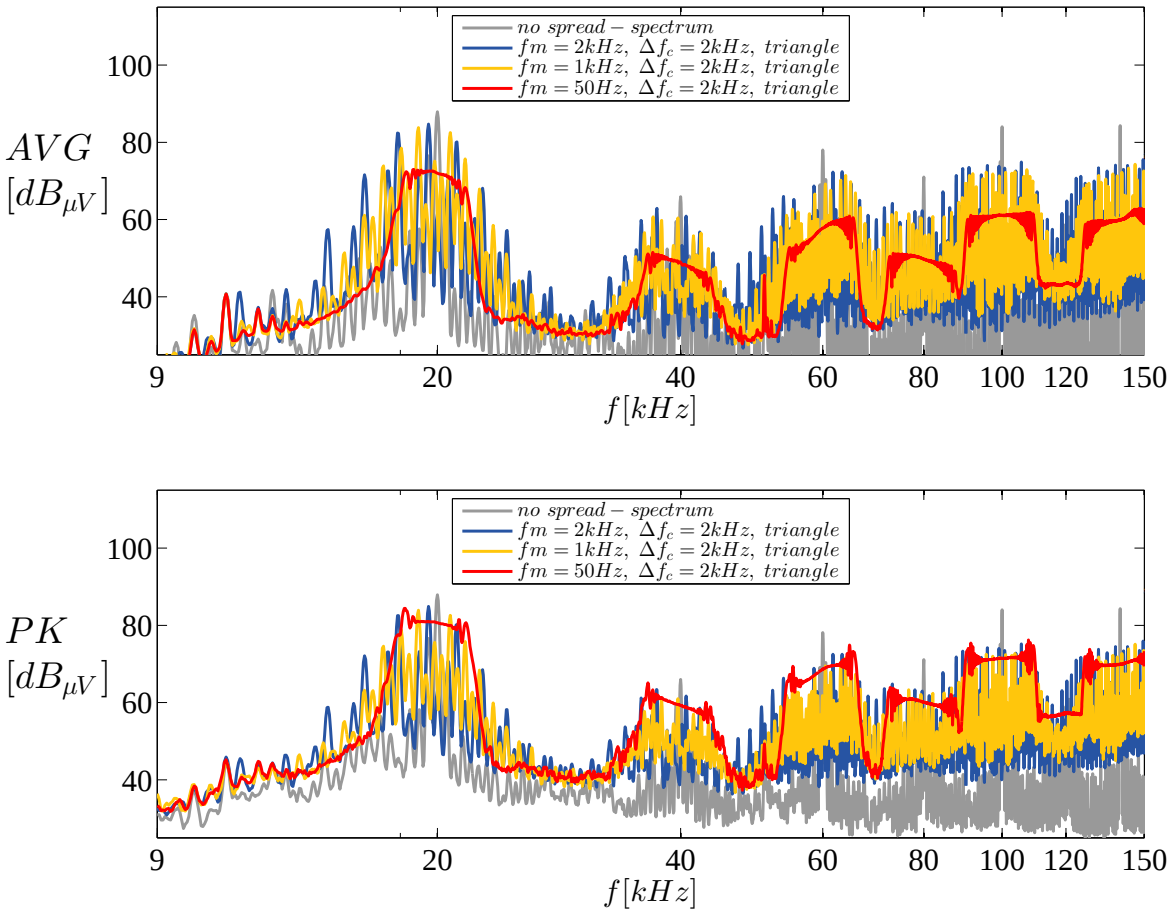

Figure 7.5: Measurement: Impact of the modulation frequency f_m used in deterministic spread spectrum techniques on the average- and peak-emission spectra in the CISPR band A

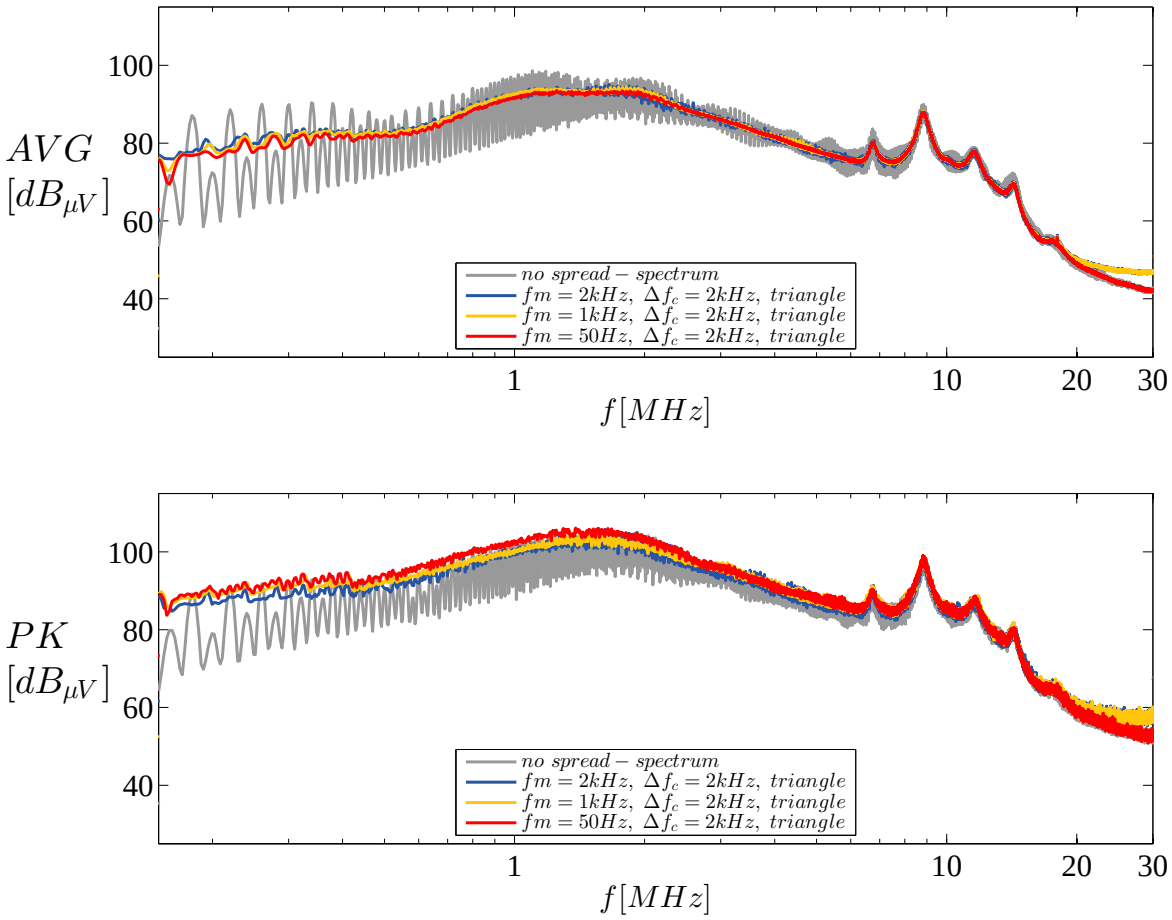

Figure 7.6: Measurement: Impact of the modulation frequency f_m used in deterministic spread spectrum techniques on the average- and peak-emission spectra in the CISPR band B and a frequency range between 150kHz and 4MHz

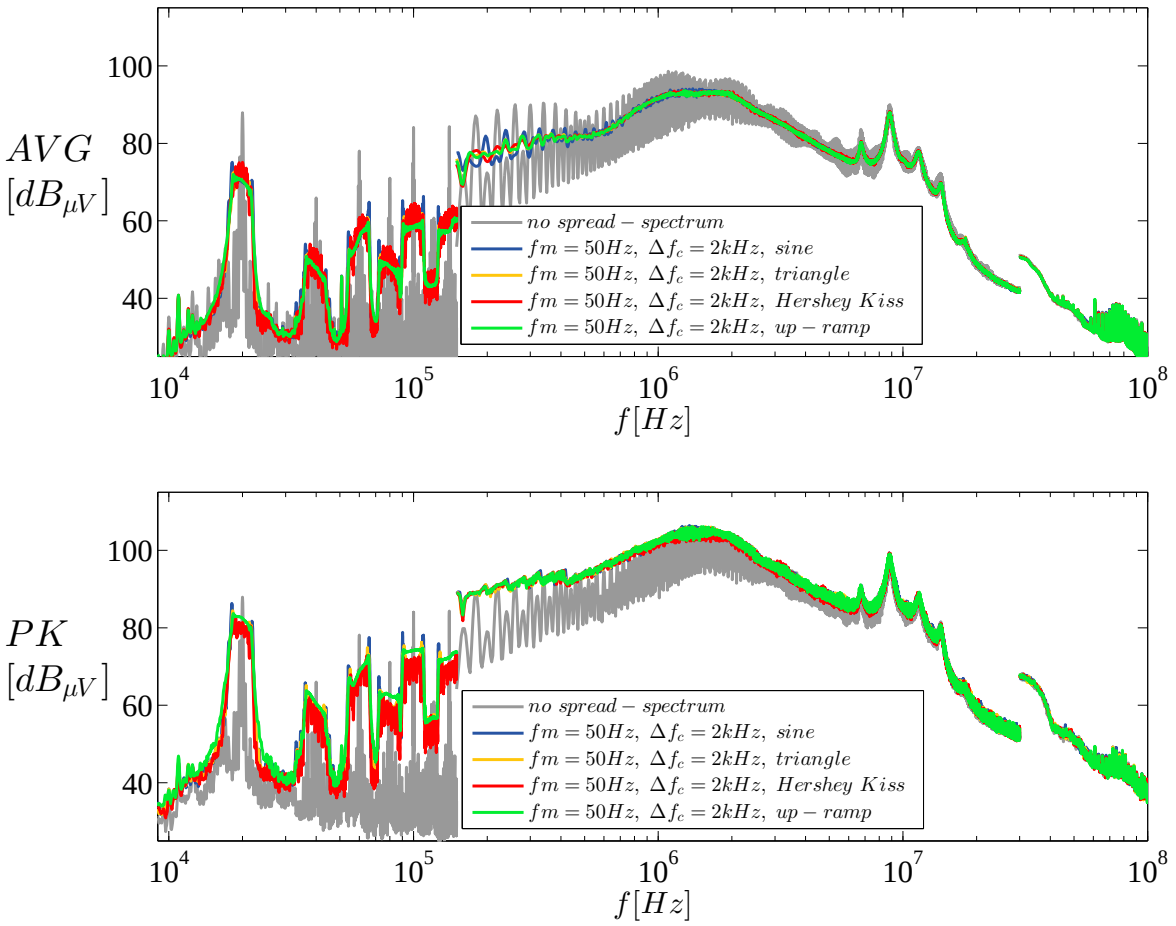

Figure 7.7: Measurement: Impact of the modulation frequency f_m used in deterministic spread spectrum techniques on the average- and peak-emission spectra in the CISPR bands A,B and C

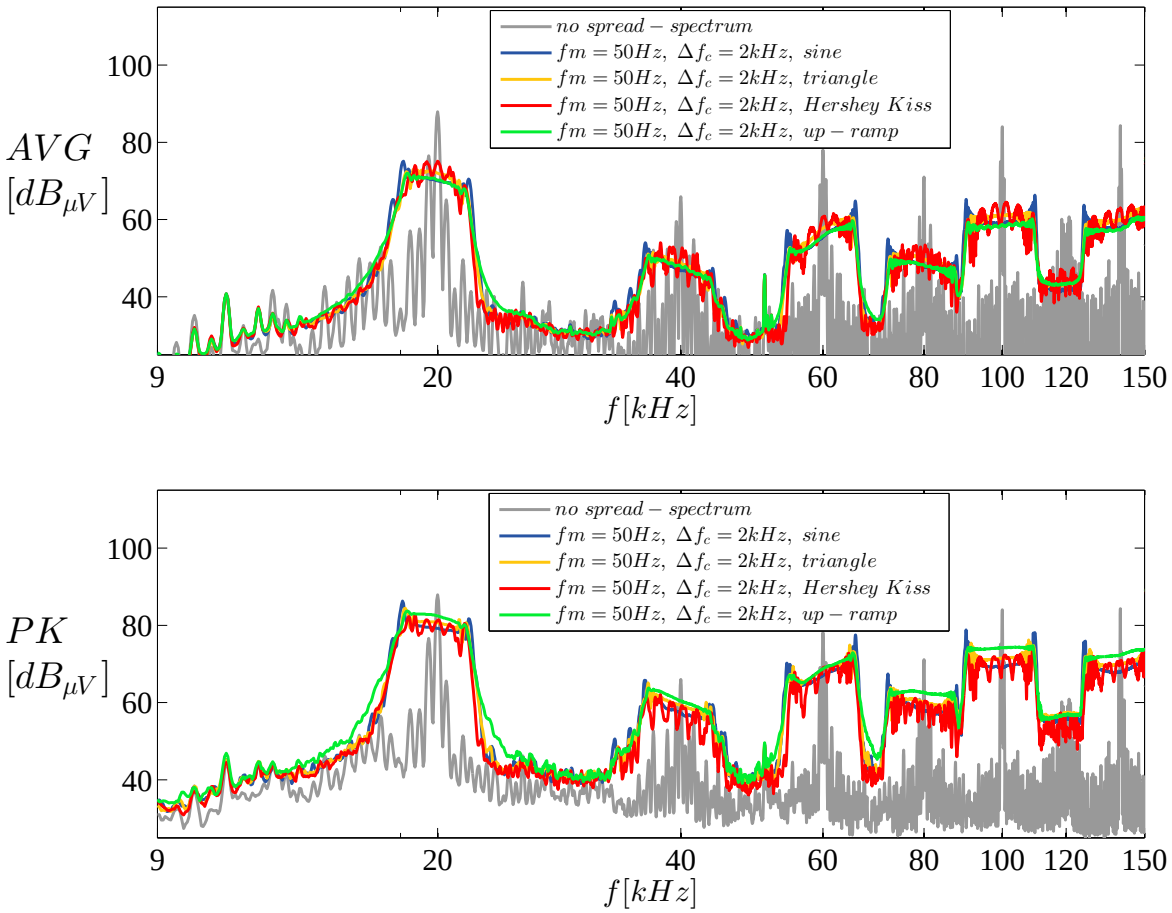

Figure 7.8: Measurement: Impact of the modulation frequency f_m used in deterministic spread spectrum techniques on the average- and peak-emission spectra in the CISPR band A

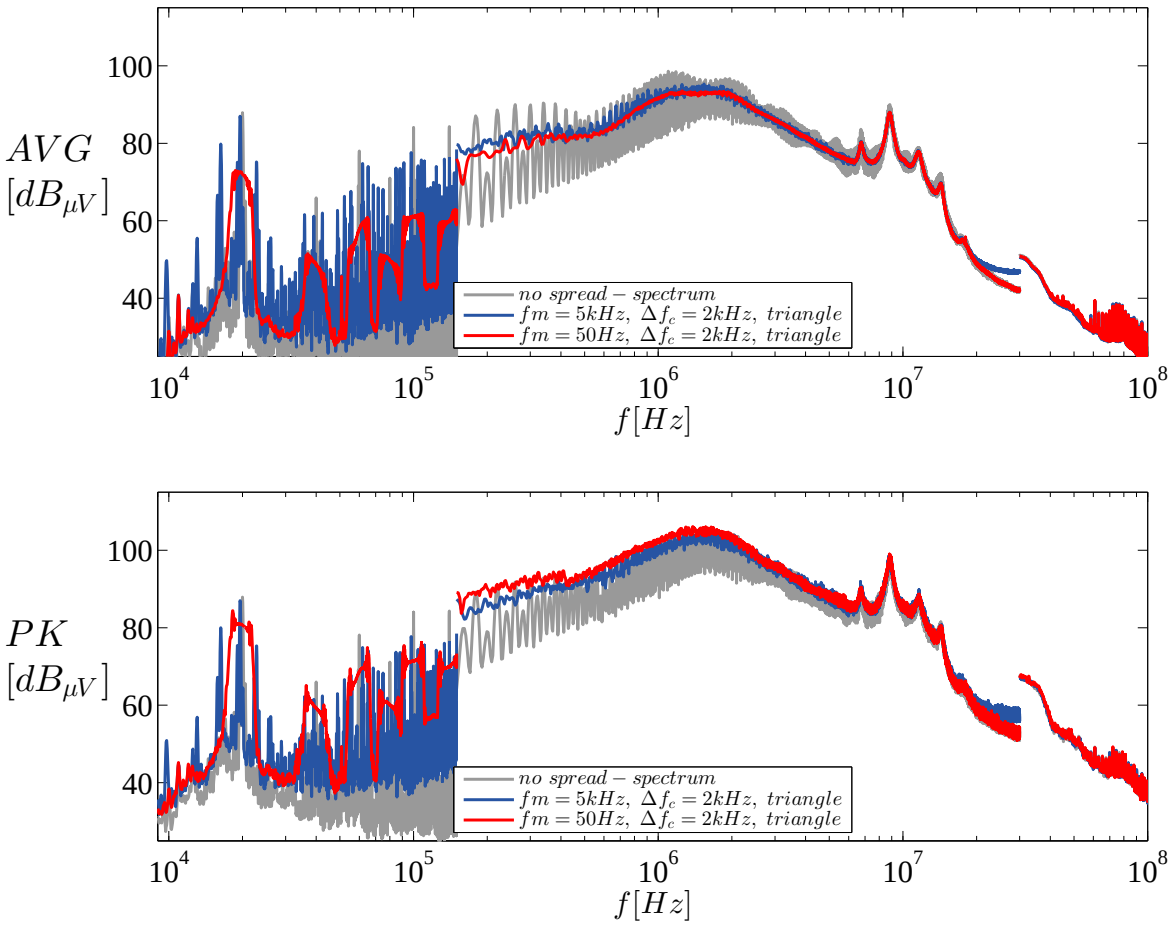

Figure 7.9: Measurement: Systematic reduction of the average- and the peak-detector levels by the utilization of different parameter configurations of f_m and Δf_c

7.3 Conclusion and Design Recommendations

To clarify the question which spread spectrum technique leads to the best overall performance according to an emission reduction of both detector levels, selected spread spectrum techniques are compared to each other in figure 7.10.

In the CISPR band A, the deterministic spread spectrum technique with $f_m = 50Hz$ clearly provides the best reduction of both the average- and the peak detector level, especially at the fundamental frequency of $20kHz$.

In the CISPR band B, all considered schemes lead to similar average detector levels. Concerning the peak detector level, the deterministic schemes lead to the highest values for $f_m = 50Hz$ and to the lowest values for $f_m = 2kHz$, where the level of the RCF scheme lies in between.

Involving the CISPR25 standard [1] in the selection process of a suitable spread spectrum technique, the deterministic spread spectrum scheme with the parameters $\Delta f_c = 2kHz$ and $f_m = 2kHz$ seems to be a good trade-off between the possible average- and peak detetor emission reduction since there is no compulsory limitation currently valid in the CISPR band A. However, there are certain manufacturer standards which prescribe a limitation even in band A. A deterministic scheme with low modulation frequencies (e.g. $f_m = 50Hz$) might be the better choice there.

For this reason, it is difficult, or not possible at all, to make a concrete statement regarding which spread spectrum scheme may be the best in the considered system.

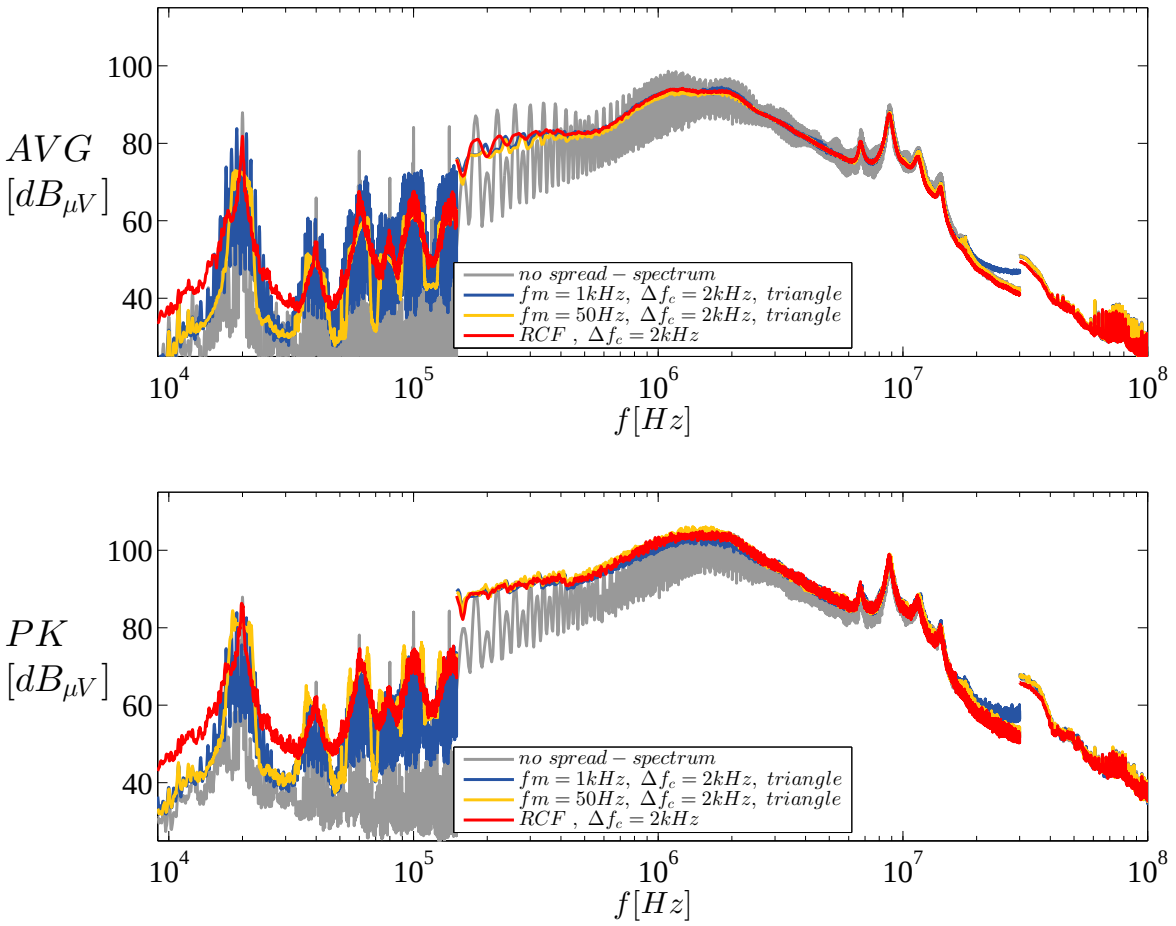

Figure 7.10: Measurement: Comparison of selected spread spectrum techniques which achieve a good overall performance

Chapter 8

Summary and Outlook for Future Work

In this thesis, the applicability and the effect of spread spectrum was investigated in order to reduce electromagnetic emissions in a 6-phase voltage source DC to AC converter. To get familiar with the characteristic behavior of spread spectrum, different techniques were applied and analyzed by evaluating the Fourier spectrum of space vector PWM signals with finite rise and fall times at first. Since this kind of analysis does not allow a direct implication on the actual emissions or EMI detector values, a circuit based simulation model was derived. The modeling was mainly performed by individual impedance measurements on the circuit components wherever possible in order to estimate the effectiveness of the developed spread spectrum techniques. Together with the developed EMI receiver model which is applied on the output signal of the transient circuit simulation by a post processing step, a remarkable accuracy between the model and the measurement could be achieved. Hence, the advantages and disadvantages of both the randomized and the deterministic spread spectrum techniques could be validated by simulations in advance followed by a subsequent verification by the corresponding measurements. By using spread spectrum in the considered system, the emission reduction could be established from the fundamental frequency on up to a frequency of $30MHz$ and thus represents a software solution either to reduce the filter effort or gaining extra margin in an already compliant system without making any changes on its hardware.

Apart from the accumulated knowledge about the use of spread spectrum in order to reduce electromagnetic emissions, some topics were not sufficiently examined yet and thus should be further investigated.

In this thesis, the impact of spread spectrum could only be validated by excluding the rotor from the PMSM and thus only facilitated the operation with primarily reactive currents which often does not reflect reality. Another very important topic which is decisive if spread spectrum can be applied to a system or not is the analysis of the effect on the system stability since the variation of the PWM period can be assumed to be challenging for the current control loops. Here, it would be of great interest how the presented spread spectrum parameters can be set in a real application to guarantee an acceptable stability margin. At this point, the further developement of the derived model that allows the simulation of all modes of operation would be desirable.

Regarding the simulation model, the reason of the resonance effects occurring around $10MHz$ has not been clarified yet. These interferences could either be caused by the EUT itself or, for example, can have its reason in the greatly simplified modeling of the stator and its parasitic capacitances to the motor housing by lumped circuit parameters. Here, a more realistic approach that describes the stator and its parasitics by distributed parameters would seem reasonable. Another reason for this appearance could also be the development-related measurement which was not carried out in an anechoic chamber and so does not fully comply with the standard.

A fact which was not considered in the system model at all is the exclusion of inductive coupling paths as their evaluation turned out to be difficult or with great uncertainty only. This, for example, could apply to the stator windings as well as to the linkage between the DC supply line and the artificial network and the EUT, or to the linkage between the supply lines and the ground reference plane. It could then be imaginable that this also leads to a better representation at the first harmonic which vanishes in the simulation but not in the measurement at the real system.

When it comes to the addressed nonlinear effect induced by the interlock time in the halfbridges, a more sophisticated approach for its feed forward compensation is adviseable especially for low modulation indeces.

As final statement, there does not excist *the* spread spectrum scheme which achieves an improvement in all frequency ranges and for all detectors used in EMI measuring receivers. Unfortunately, the reduction of the peak detector level proved to be problematic or marginally at the best in the CISPR band B. This is due to the required resolution bandwidth that is in the same range as the PWM frequency itself and therefore cannot be selected arbitrarily high. In the CISPR band A, on the other hand, a very good suppression of both the average- and the peak detector is possible by using the non-deterministic RCF scheme and the deterministic frequency modulation spread spectrum technique. However, especially the deterministic frequency modulation spread spectrum provides the possibility of systematically optimizing a certain detector by an appropriate choice of the modulation frequency. Therefore, the latter might be the more flexible choice in general, since the randomized schemes only allow the adjustment of only one parameter.

List of figures

List of tables

Appendix A

Circuit Model Parameters

DC Link Capacitor	main capacitance	C_{DC}	1100	μF
	equivalent series resistance	ESR_{DC}	11	$m\Omega$
	equivalent series inductance	ESL_{DC}	6	nH
Full-Bridge Module	Drain-Source ON resistance	$R_{DS,ON}$	850	$\mu\Omega$
	Drain-Source OFF resistance	$R_{DS,OFF}$	11	$k\Omega$
	time constant for ideal switch control signal	t_{ON-OFF}	450	ns
	equivalent MOSFET output capacitance	C_{OSS}	8.5	nF
	ohmic serial resistance of C_{OSS}	$R_{s,Coss}$	165	$m\Omega$
	ohmic parallel resistance of C_{OSS}	$R_{p,Coss}$	25	$k\Omega$
	body diode forward threshold voltage	V_f	1	V
	body diode ohmic resistance	R_f	100	$m\Omega$
	ohmic resistance between bus bar and lead frame	R_{bb-lf}	20	$\mu\Omega$
	prop. inductance between bus bar and lead frame	L_{bb-lf}	20	$\mu\Omega$
	ohmic resistance between lead frame and die	R_{lf-die}	80	$\mu\Omega$
	prop. inductance between lead frame and die	L_{lf-die}	2	nF
	snubber resistance	$R_{s,snub}$	103	$m\Omega$
	snubber capacitance	C_{snub}	4	μF
	prop. snubber inductance	L_{snub}	3.5	nH
	parallel ohmic resistance of C_{snub}	$R_{p,snub}$	25	$k\Omega$
PMSM Stator	ohmic phase resistance	R_{ph}	1	$m\Omega$
	phase inductance	L_{ph}	24	μH
Ground Strap	serial resistance	$R_{s,gnd}$	1	$m\Omega$
	parallel resistance	$R_{p,gnd}$	1	$k\Omega$
	parallel capacitance	$C_{p,gnd}$	0.5	pF
	parallel inductance	$L_{p,gnd}$	58	nH
CM Coupling Path	parasitic motor capacitance per phase	$C_{par,mot}$	3.2	nF
	ohmic resistance of $C_{par,mot}$	$R_{par,mot}$	10	$\mu\Omega$
	prop. inductance of $C_{par,mot}$	$L_{par,mot}$	800	pH
	parasitic inverter capacitance per phase	$C_{par,inv}$	171	pF
	ohmic resistance of $C_{par,inv}$	$R_{par,inv}$	180	$m\Omega$
	prop. inductance of $C_{par,inv}$	$L_{par,inv}$	6	nH
Artificial Network [1]	air coil inductance	L_{LISN}	5	μH
	capacitance between A and B	$C_{LISN,1}$	1	μF
	high pass filter capacitance	$C_{LISN,2}$	100	nF
	high pass filter resistance	R_{LISN}	1	$k\Omega$
	EMI receiver input resistance	$R_{rec,in}$	50	Ω

Table A.1: Derived model parameters from the impedance measurements

Appendix B

System Model Verification

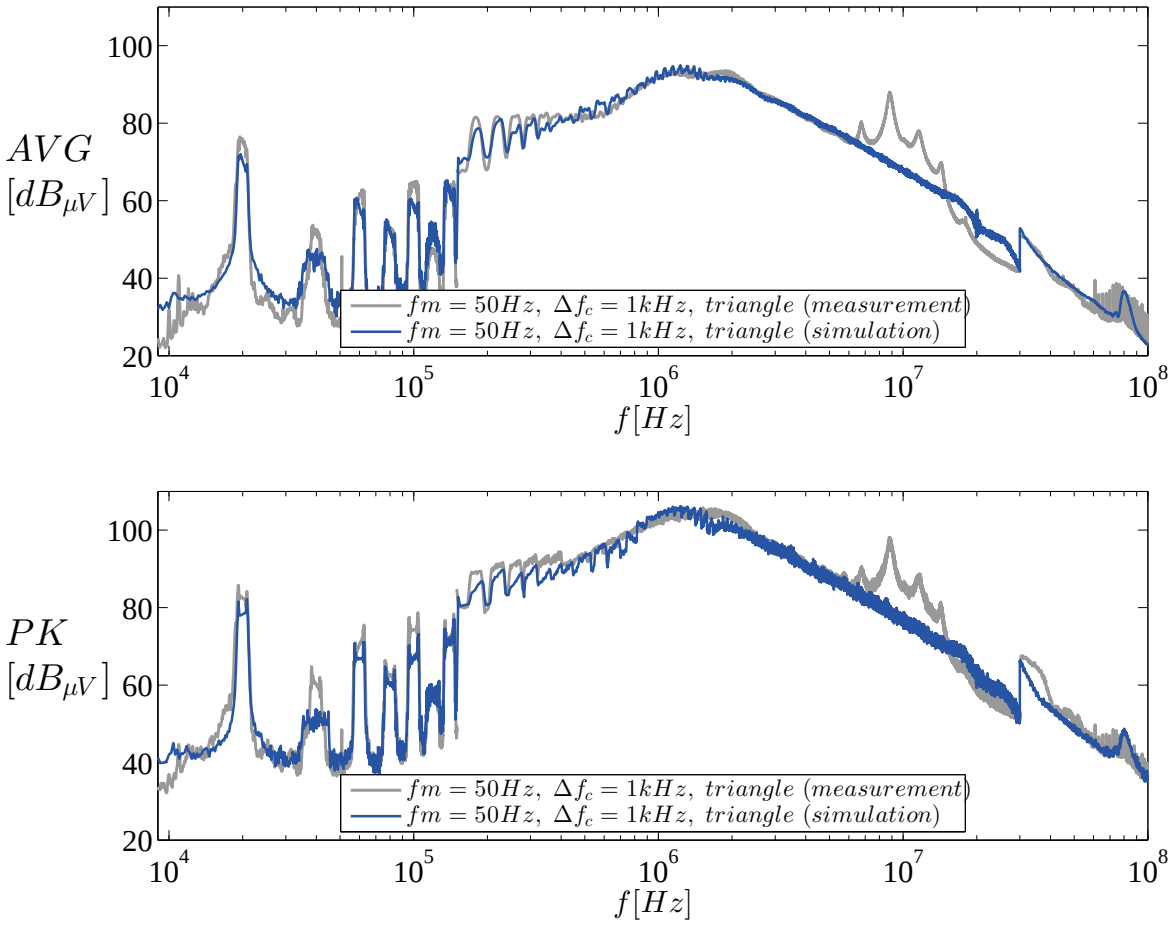

Figure B.1: Simulation vs. measurement: triangular FM, f_m = 50Hz, Δf_c = 1kHz

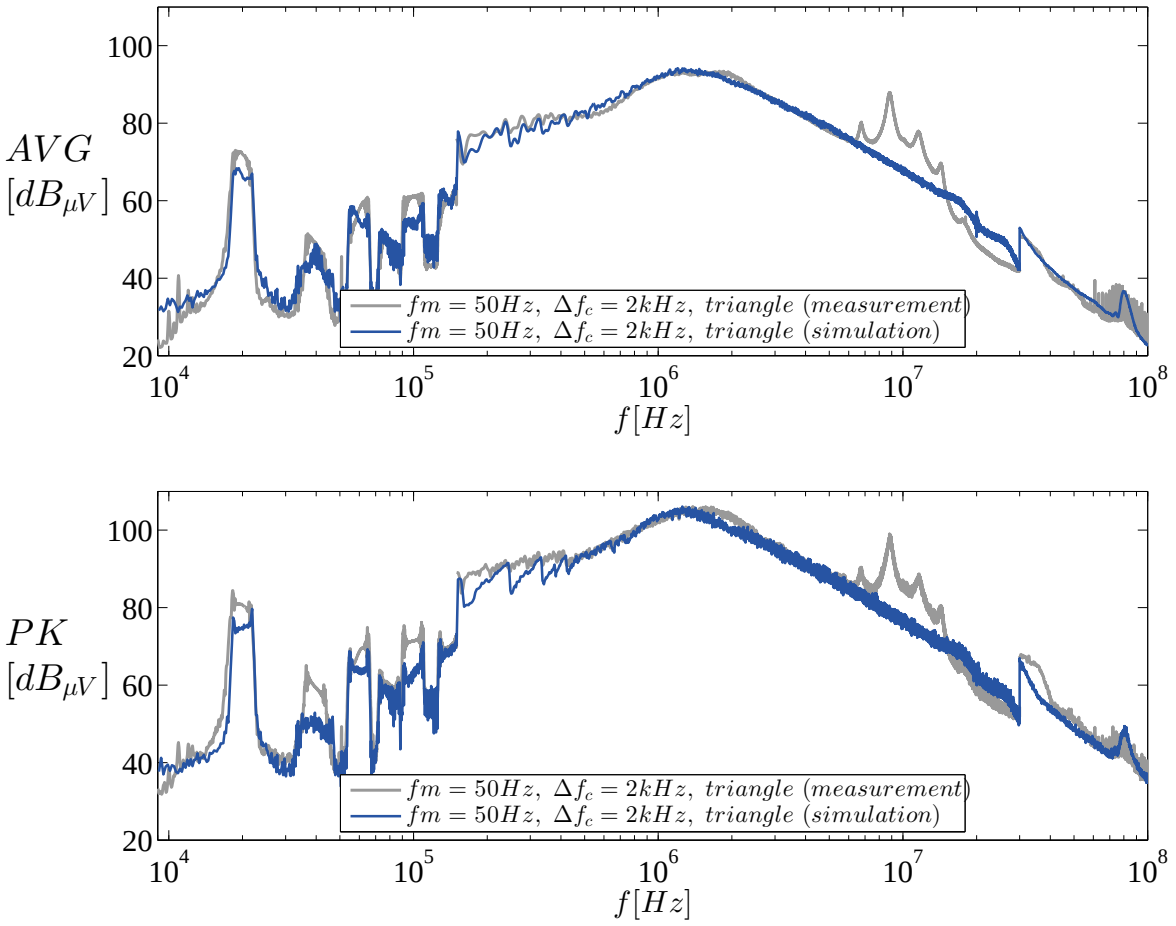

Figure B.2: Simulation vs. measurement: triangular FM, $f_m = 50Hz$, $\Delta f_c = 2kHz$

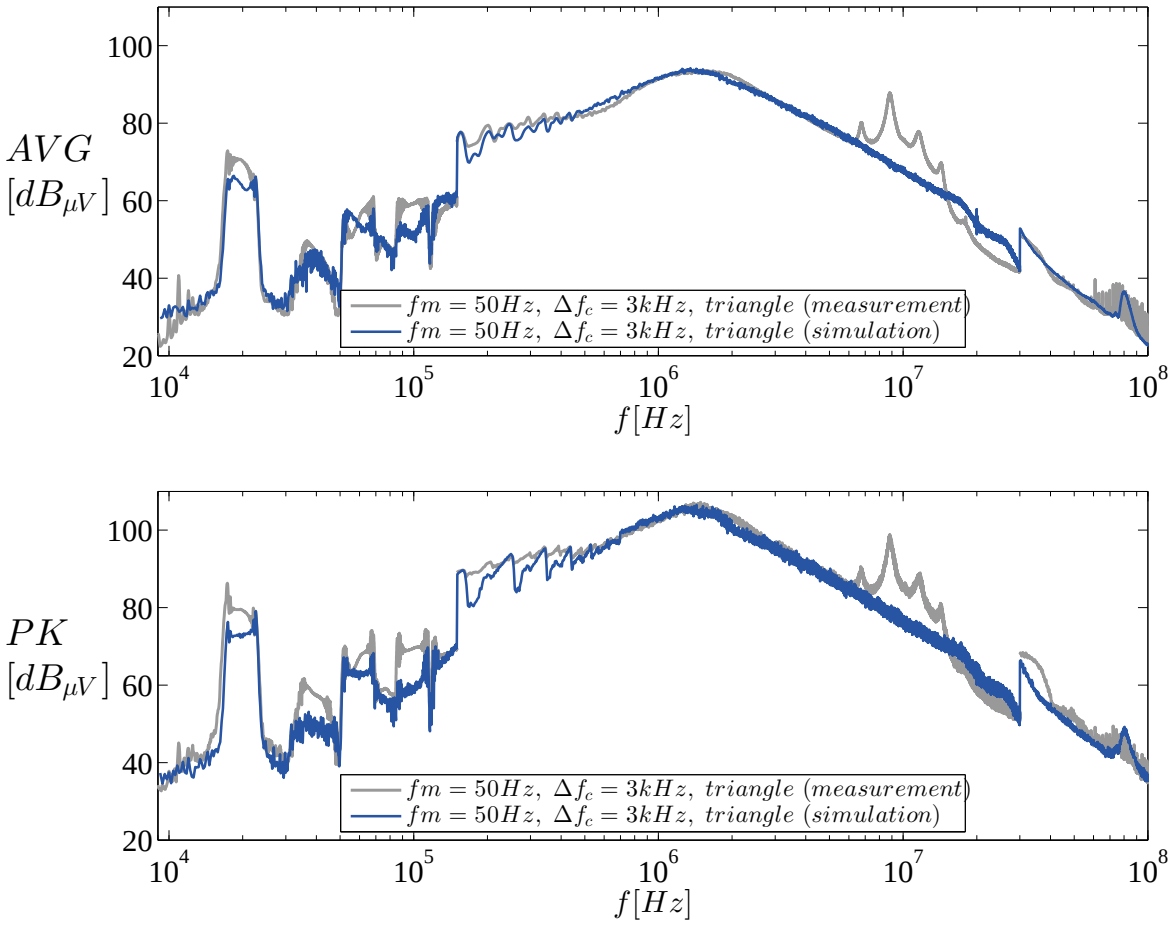

Figure B.3: Simulation vs. measurement: triangular FM, f_m = 50Hz, Δf_c = 3kHz

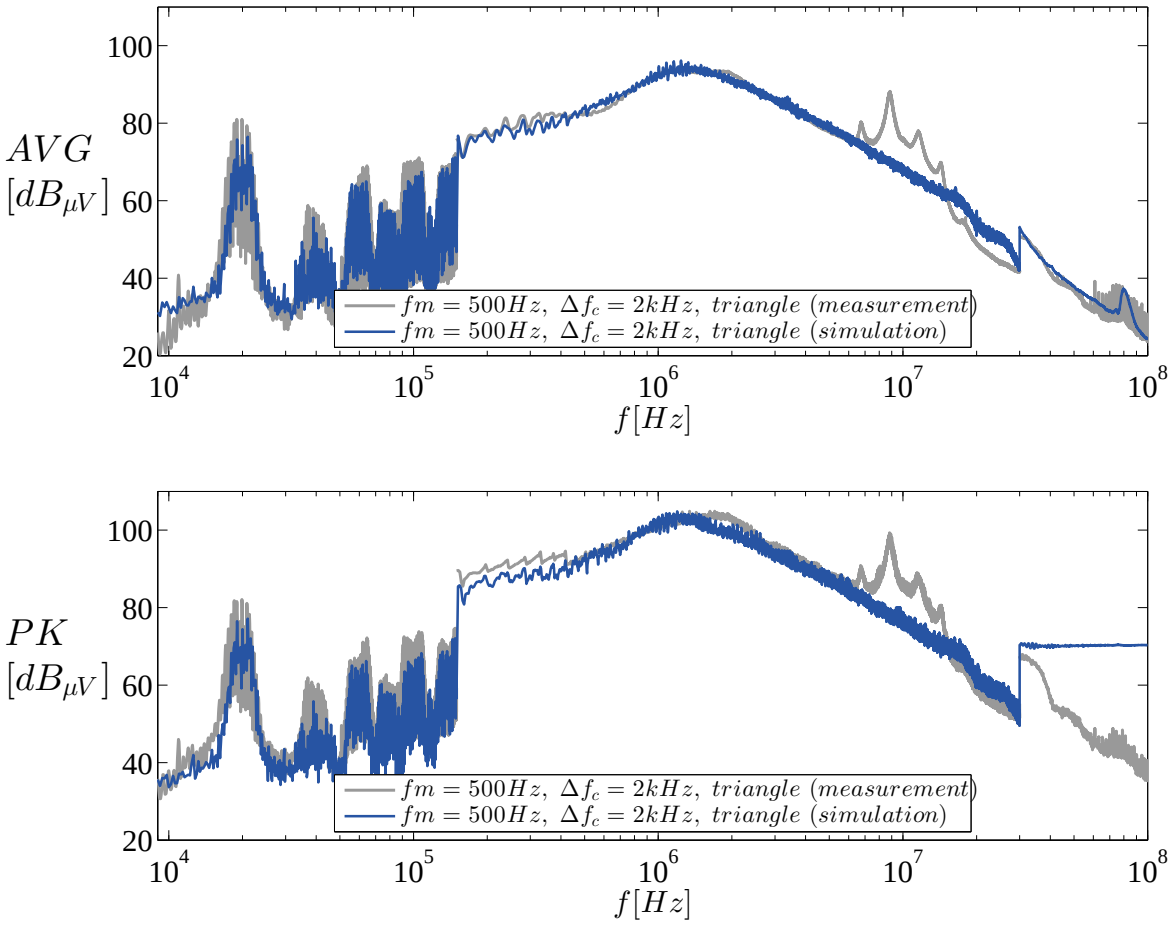

Figure B.4: Simulation vs. measurement: triangular FM, f_m = 500Hz, Δf_c = 2kHz

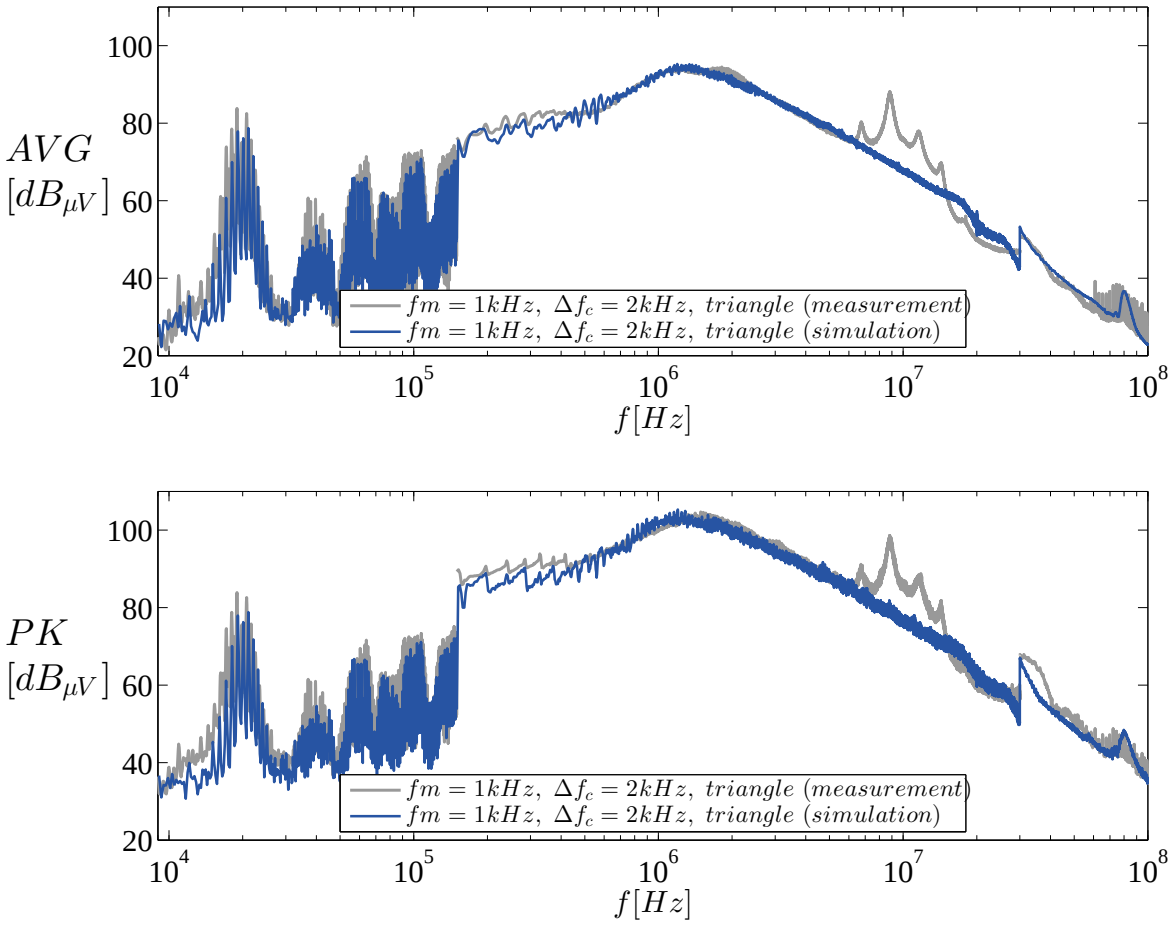

Figure B.5: Simulation vs. measurement: triangular FM, f_m = 1kHz, Δf_c = 2kHz

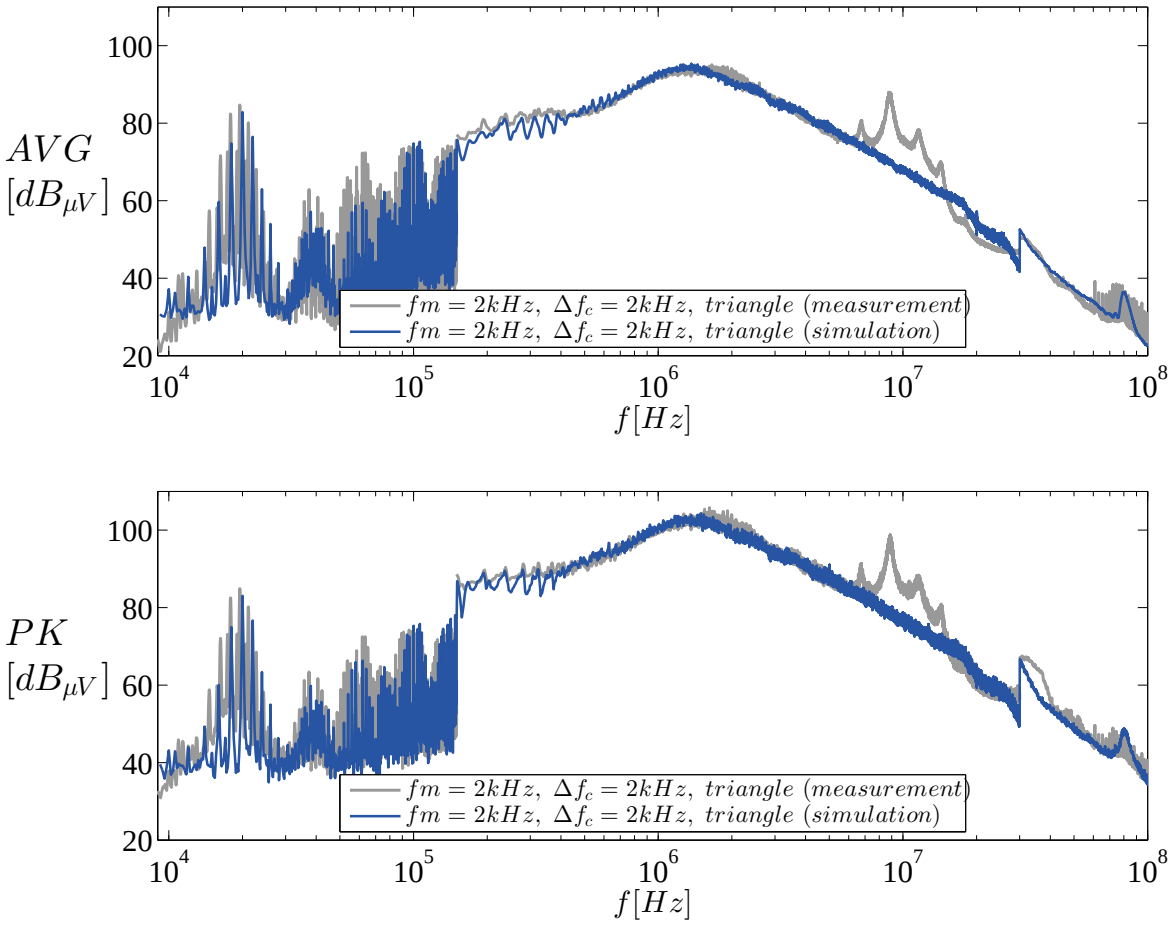

Figure B.6: Simulation vs. measurement: triangular FM, f_m = 2*kHz*, Δf_c = 2*kHz*

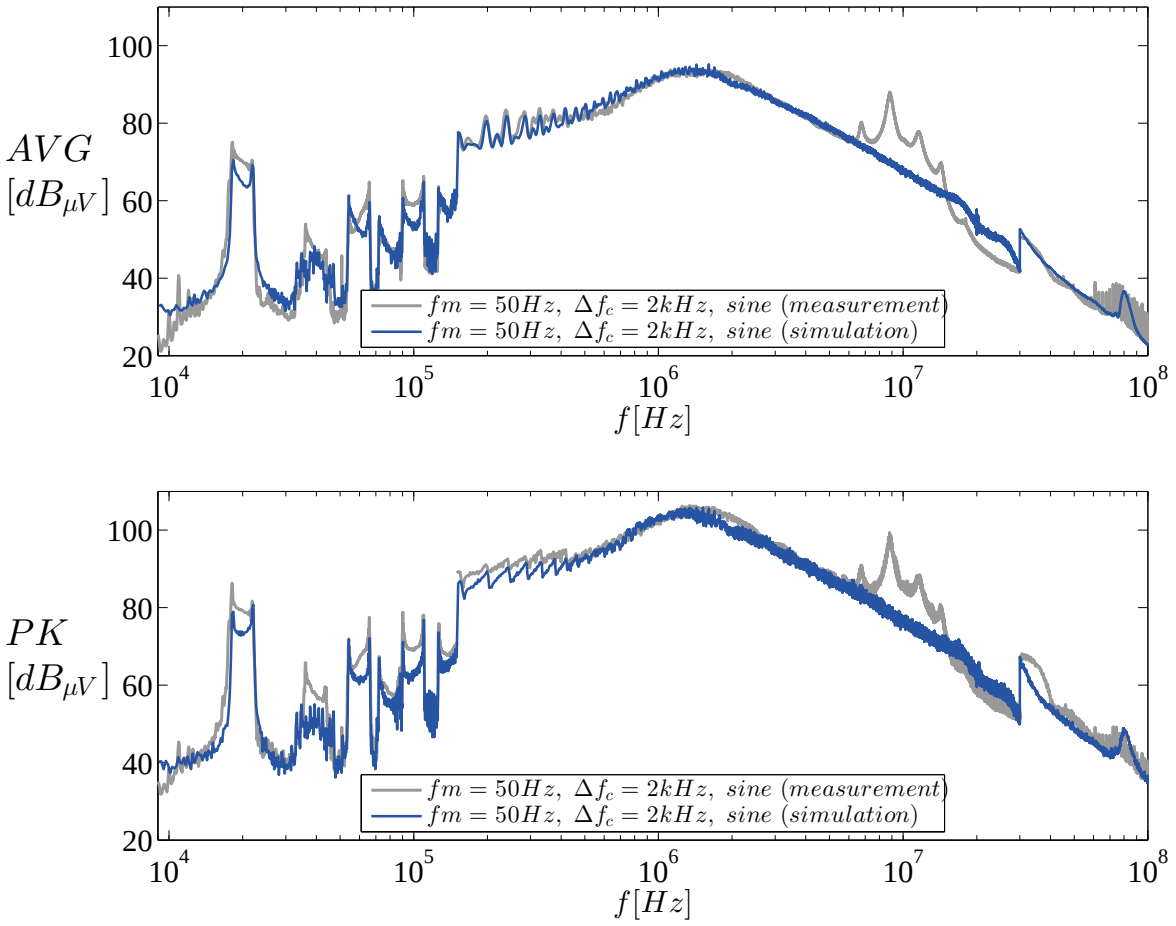

Figure B.7: Simulation vs. measurement: sinusoidal FM, f_m = 50Hz, Δf_c = 2kHz

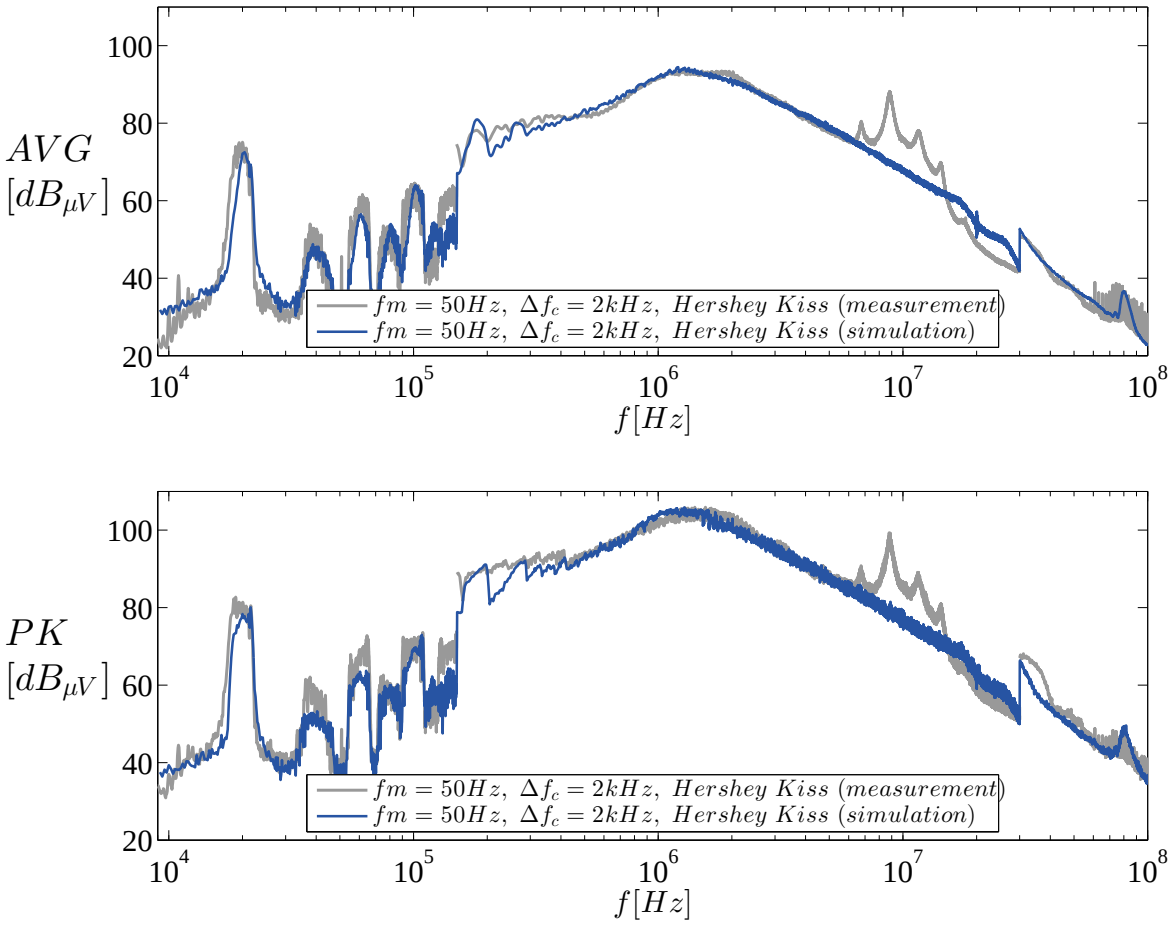

Figure B.8: Simulation vs. measurement: Hershey-Kiss FM, f_m = 50Hz, Δf_c = 2kHz

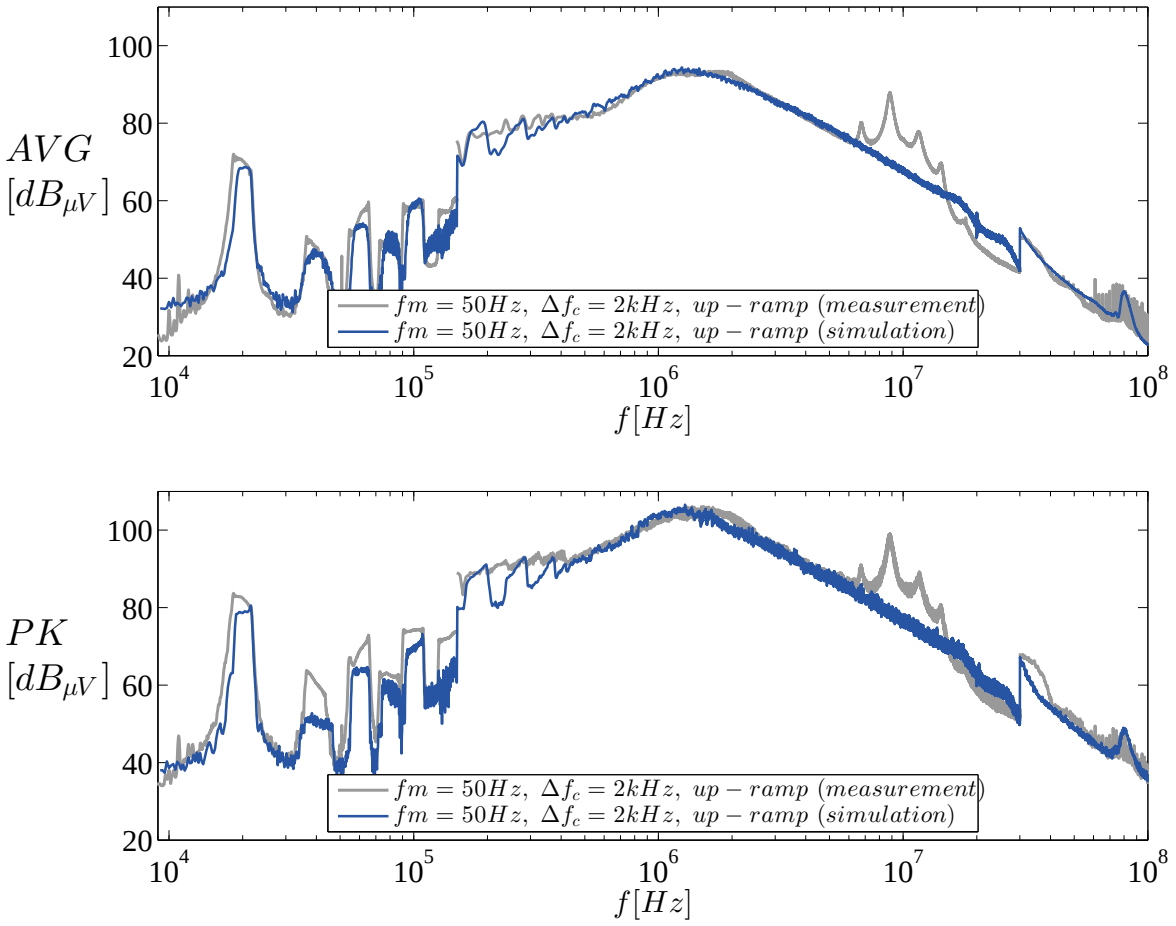

Figure B.9: Simulation vs. measurement: sawtooth FM (up-ramp), f_m = 50Hz, Δf_c = 2kHz

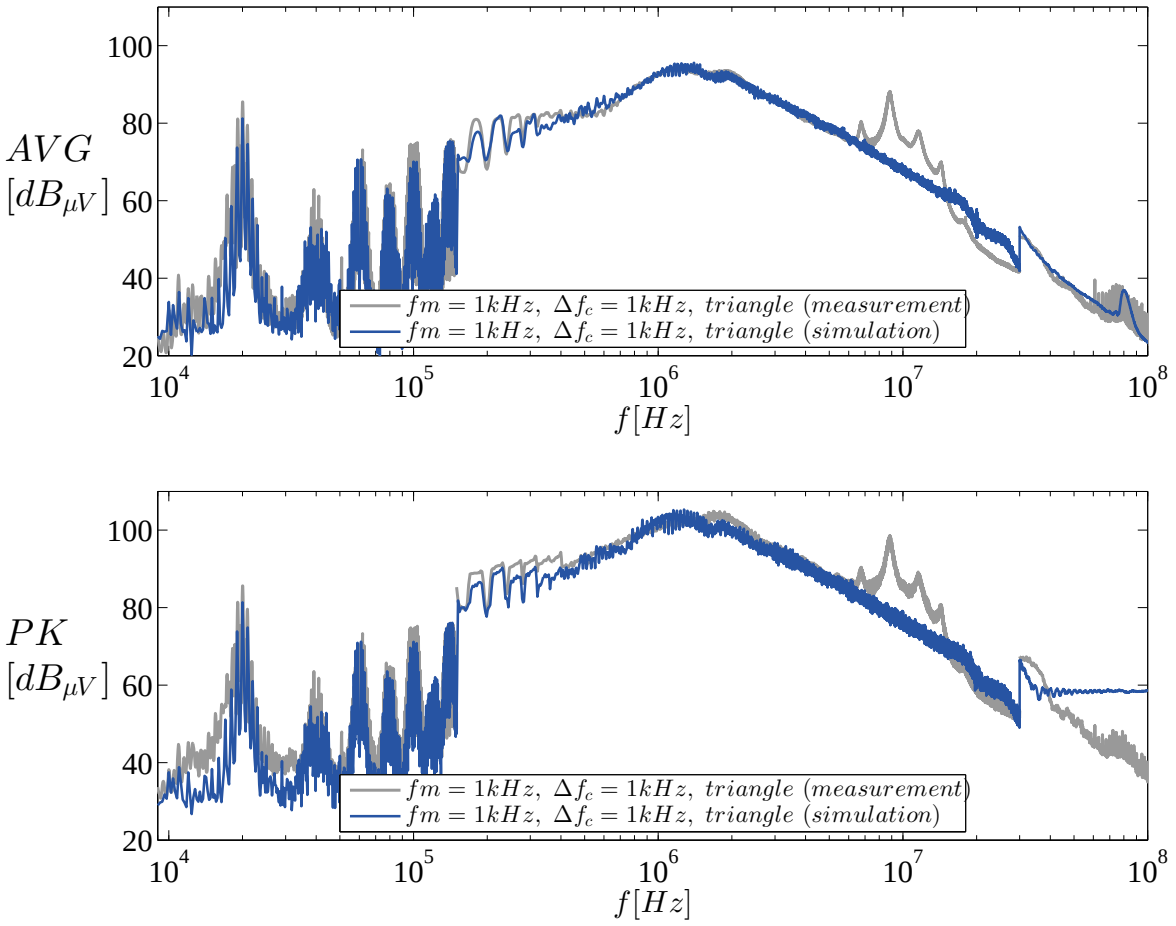

Figure B.10: Simulation vs. measurement: triangular FM, f_m = 1kHz, Δf_c = 2kHz

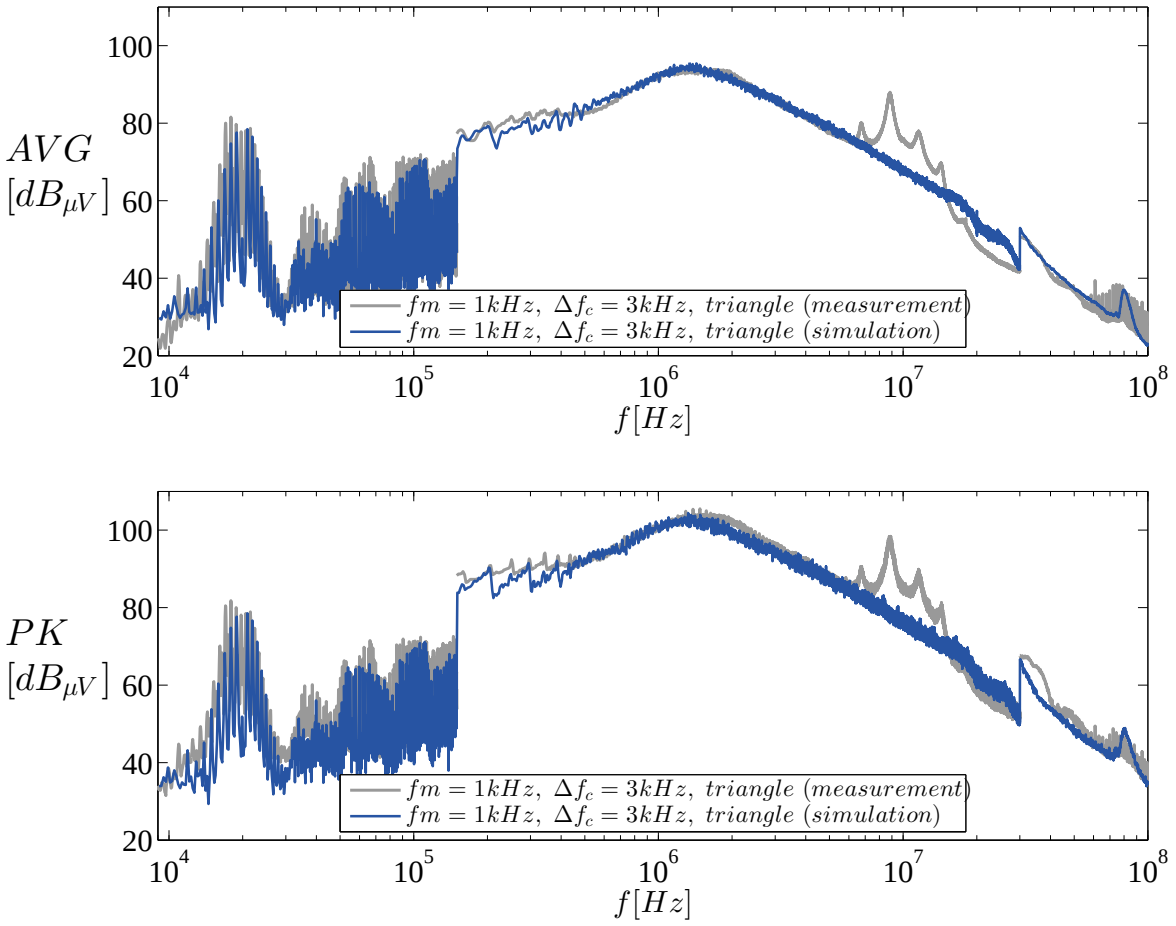

Figure B.11: Simulation vs. measurement: triangular FM, f_m = 1*kHz*, Δf_c = 3*kHz*

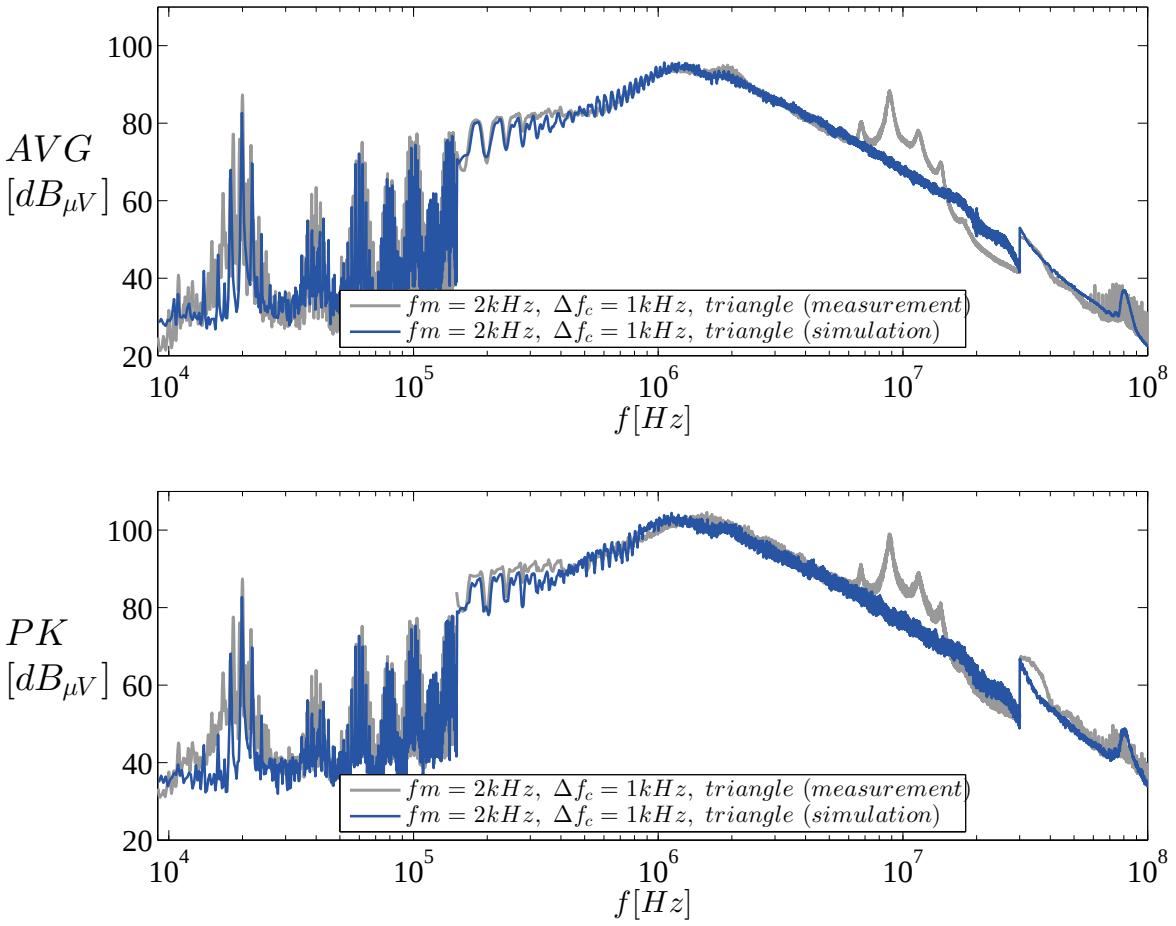

Figure B.12: Simulation vs. measurement: triangular FM, f_m = 2*kHz*, Δf_c = 1*kHz*

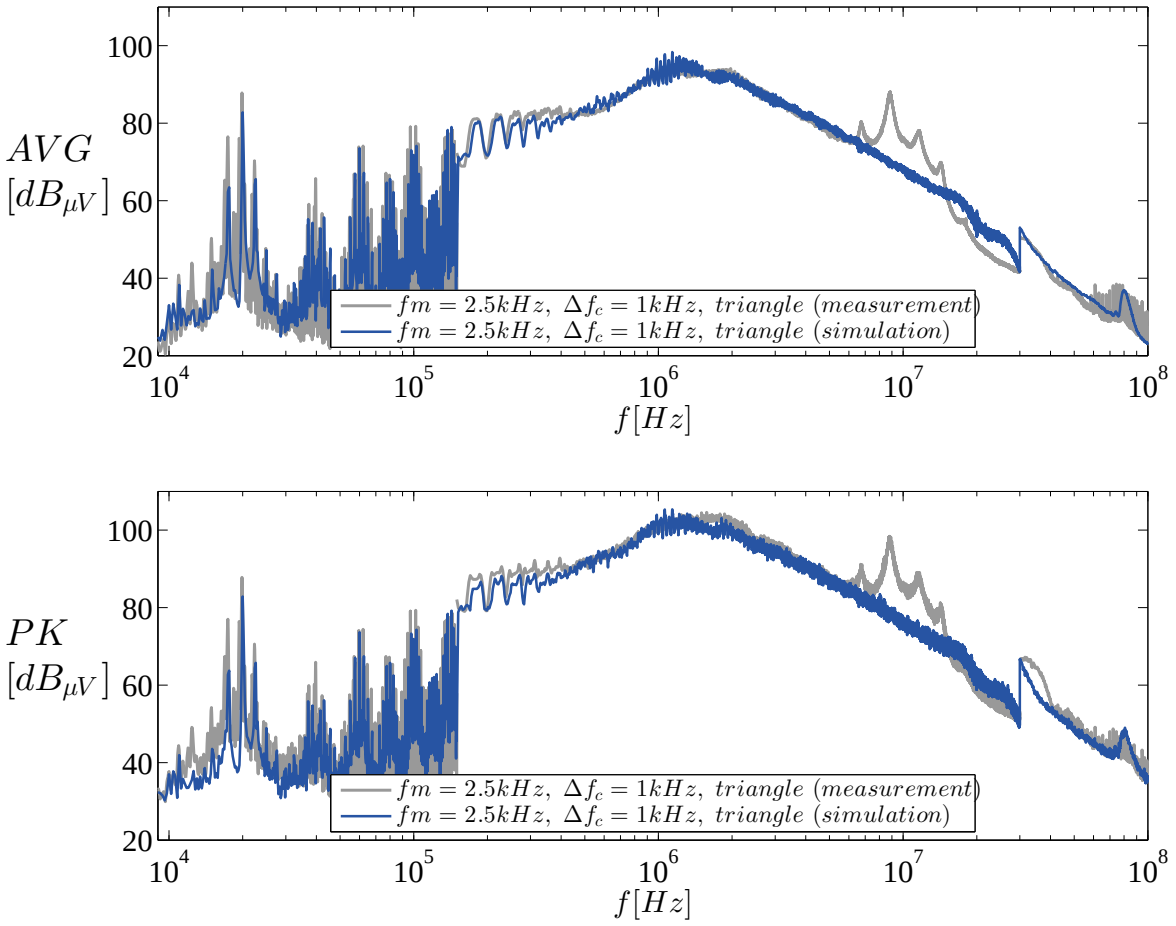

Figure B.13: Simulation vs. measurement: triangular FM, f_m = 2.5kHz, Δf_c = 1kHz

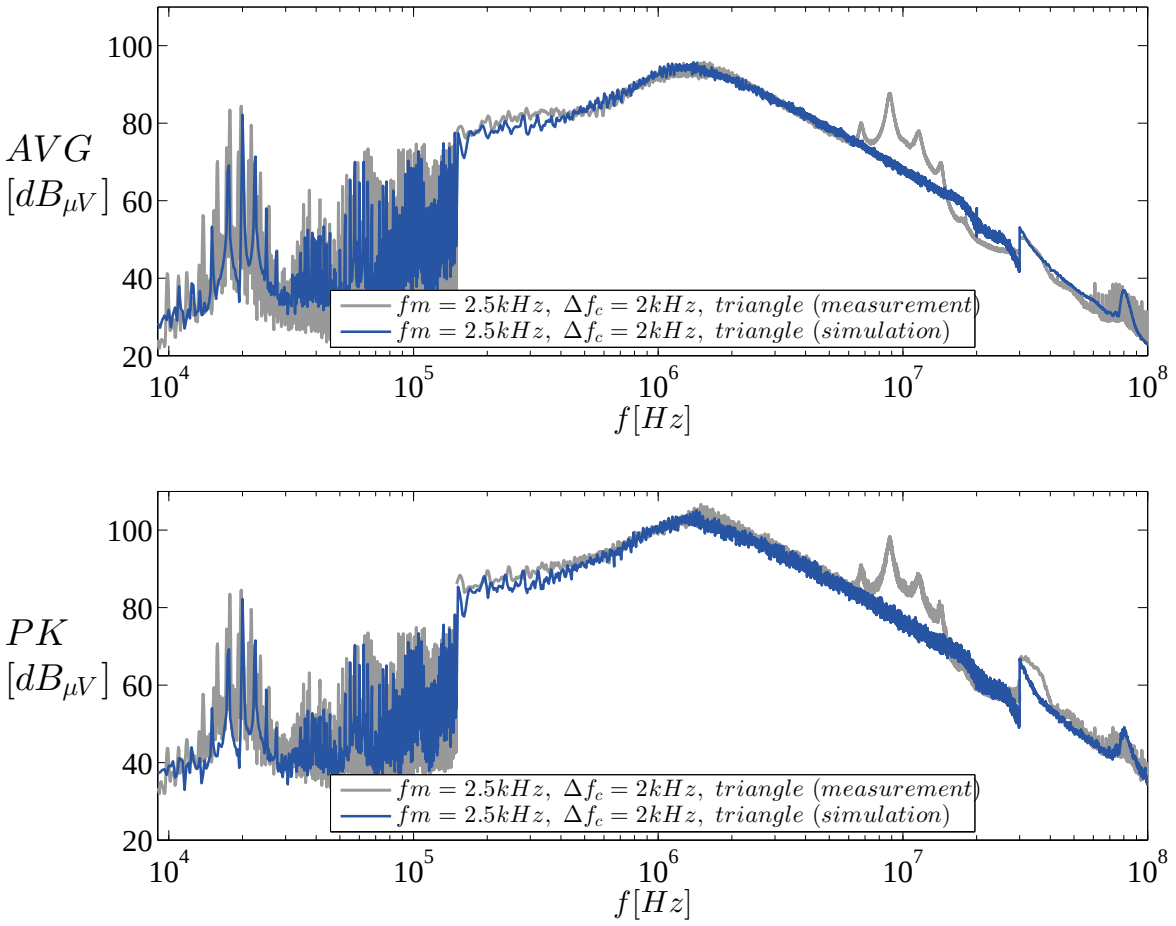

Figure B.14: Simulation vs. measurement: triangular FM, f_m = 2.5kHz, Δf_c = 2kHz

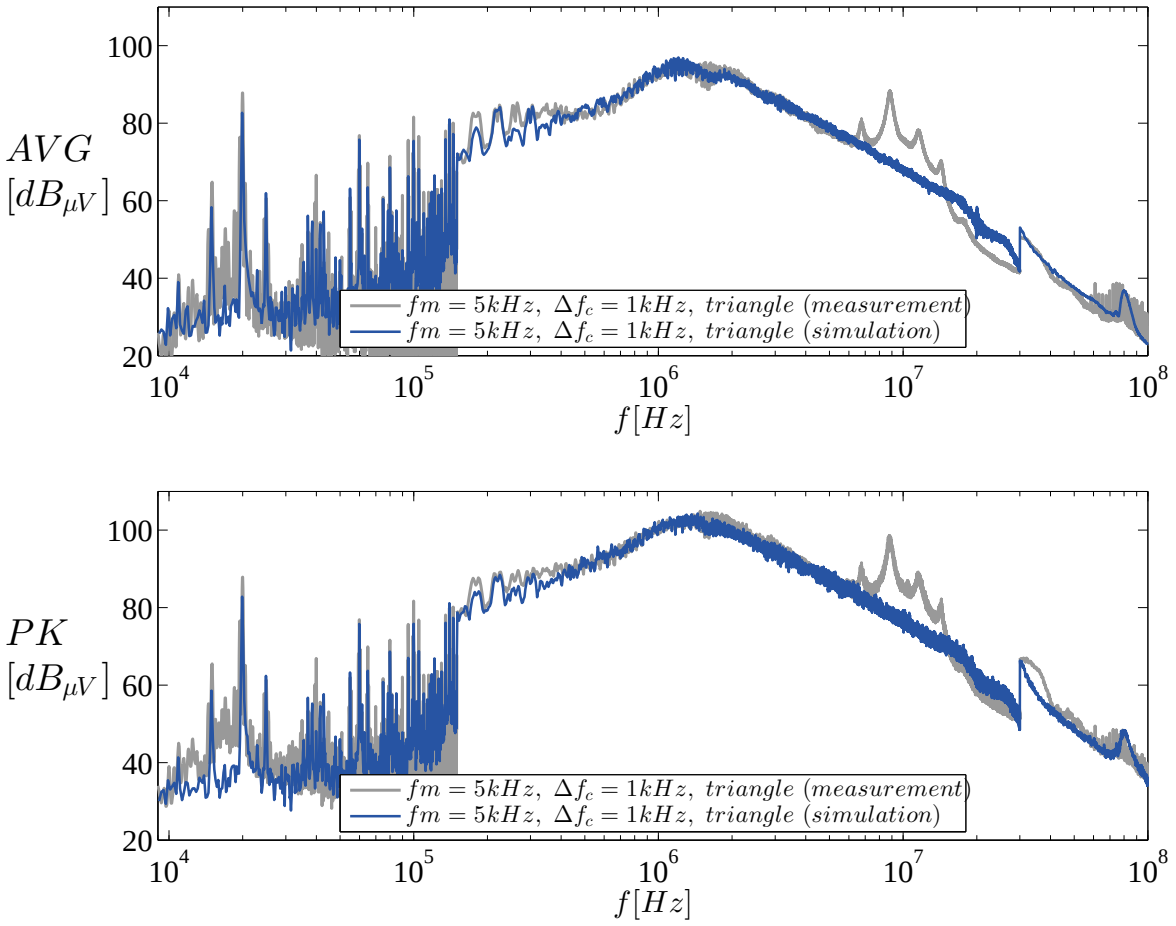

Figure B.15: Simulation vs. measurement: triangular FM, f_m = 5*kHz*, Δf_c = 1*kHz*

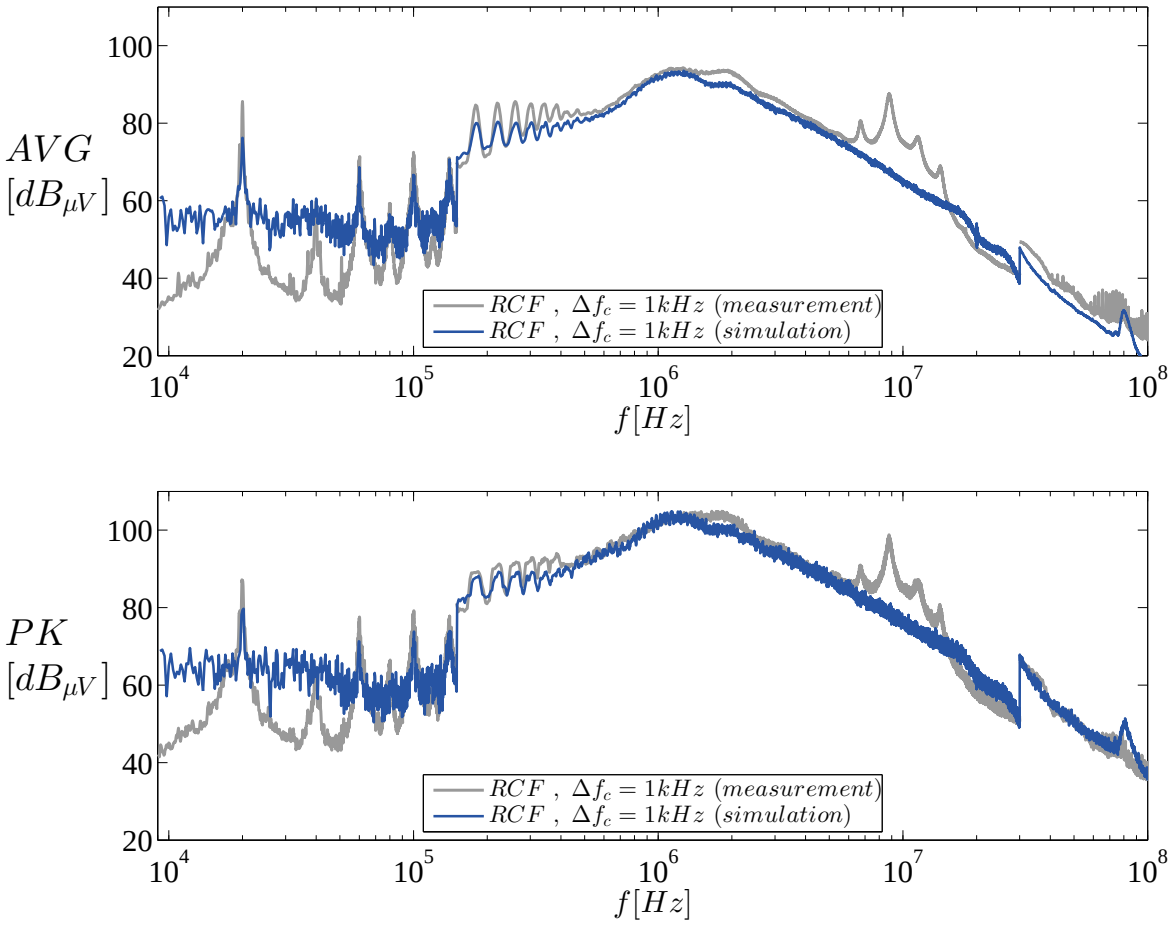

Figure B.16: Simulation vs. measurement: RCF, Δf_c = 1kHz

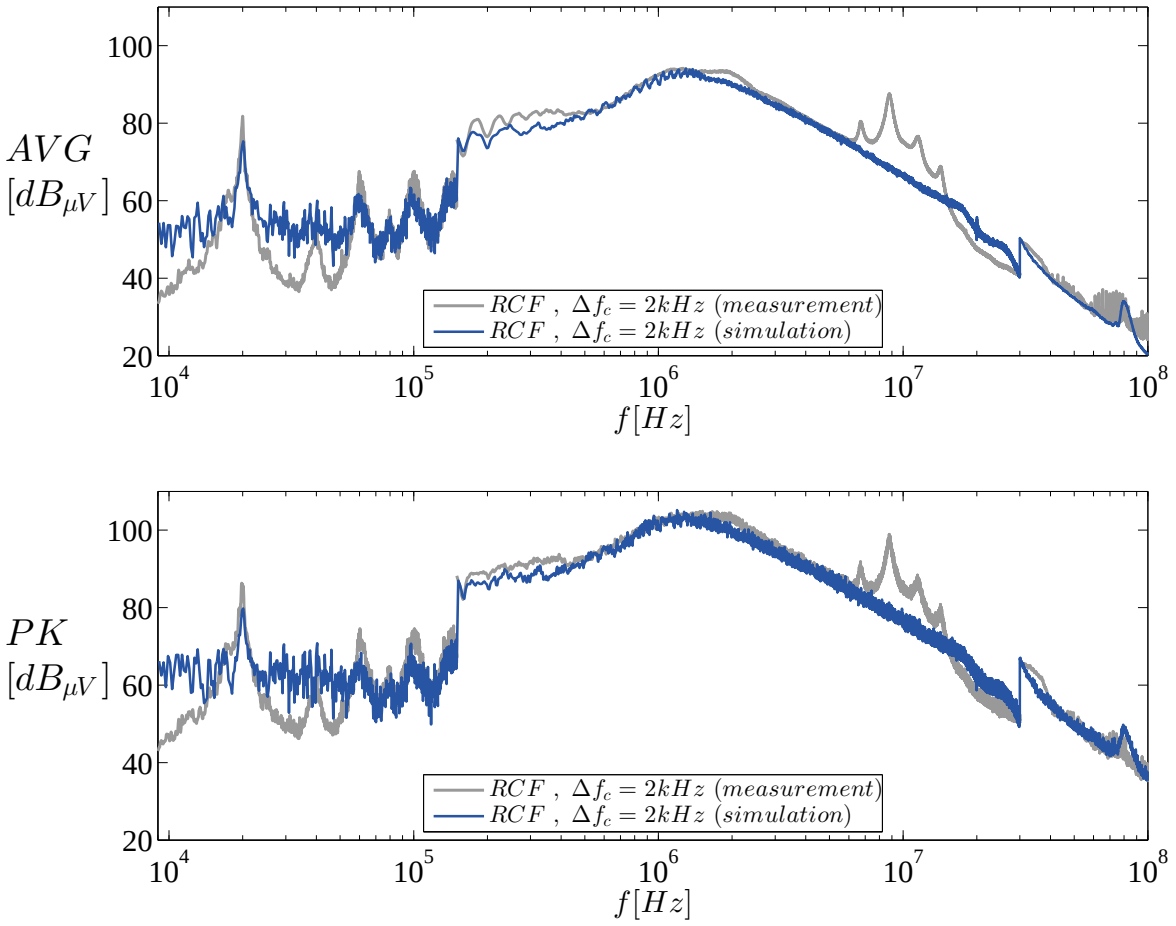

Figure B.17: Simulation vs. measurement: RCF, $\Delta f_c = 2kHz$

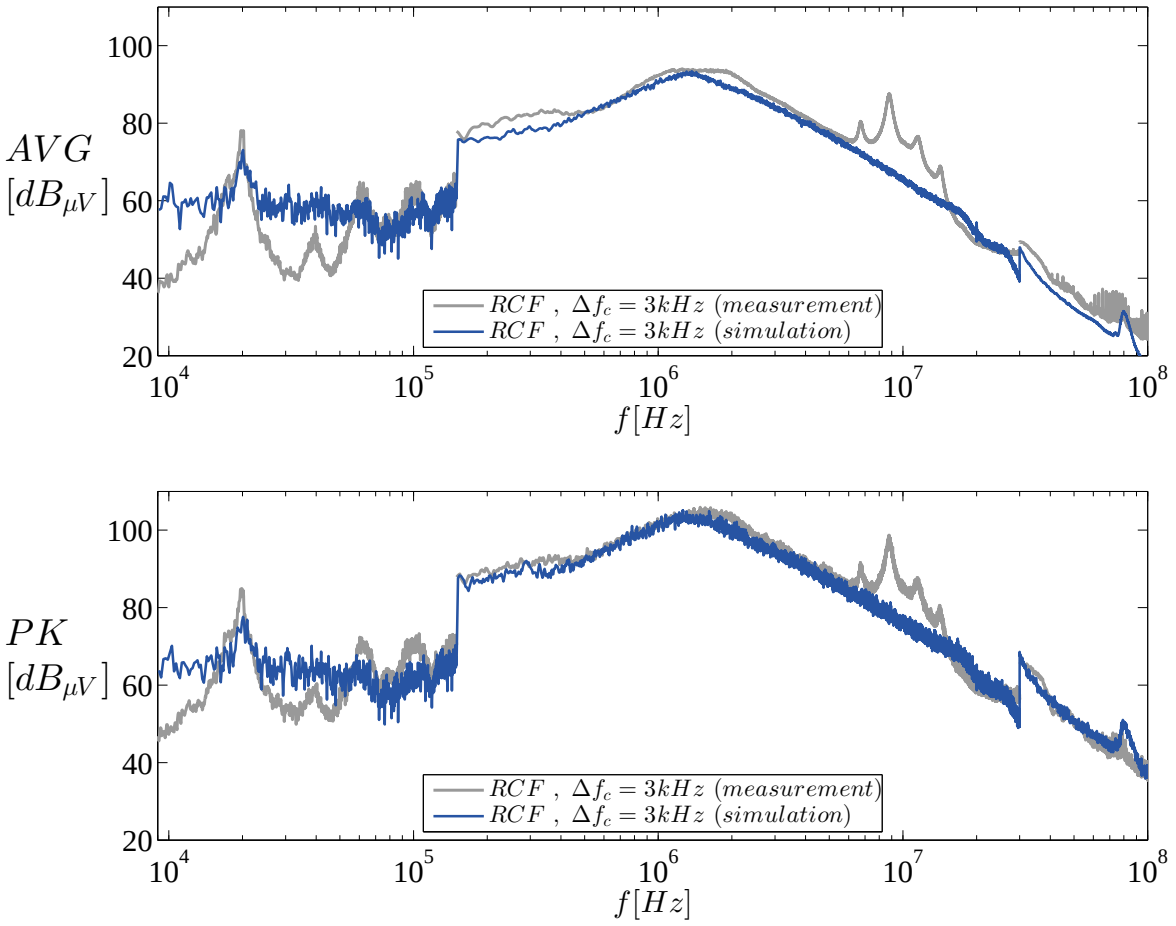

Figure B.18: Simulation vs. measurement: RCF, Δf_c = 3*kHz*

Bibliography

[1] "CISPR 25, Edition 4.0". In *CISPR Std.* IEC, Okt 2016.

[2] *"CISPR 16-1-1 ed3.0 - Specification for radio disturbance and immunity measuring apparatus and methods - Part 1-1: Radio disturbance and immunity measuring apparatus - Measuring apparatus"*. Jan 2010.

[3] M. Paramasivan, M. M. Paulraj, and S. Balasubramanian. "Assorted carrier-variable frequency-random PWM scheme for voltage source inverter". *IET Power Electronics*, Jul 2017.

[4] L. Zhu, F. Bu, W. Huang, and T. Pu. "Analysis and Performance of Two Dual Random SVPWM for Five-phase Inverter". In *2017 20th International Conference on Electrical Machines and Systems (ICEMS)*, pages 1–4, Aug 2017.

[5] N. Boudjerda, A. Boudouda, M. Melit, B. Nekhoul, K. El Khamlichi Drissi, and K. Kerroum. "Optimized Dual Randomized PWM Technique for Reducing Condcuted EMI in DC-AC Converters". In *Proc. of the 10th Int. Symposium on Electromagnetic Compatibility (EMC Europe 2011), York, UK*, pages 701–706, Sep 2011.

[6] P. Muthukumar, P. Melba Mary, and S. Jeevananthan. "An Improved Hybrid Space Vector PWM Technique for IM Drives". *Circuit and Systems*, 7(9):2120–2131, Jul 2016.

[7] H. Kiani Savadkoohi, D. Arab Khaburi, and S. Sadr. "A New Switching Method for PWM Inverter with Uniform Distribution of Output Current's Spectrum". In *The 6th Power Electronics, Drive Systems Technologies Conference (PEDSTC2015)*, pages 242–246, Feb 2015.

[8] B. Deutschmann, B. Auinger, and G. Winkler. "Spread Spectrum Parameter Optimization to Supress Certain Frequency Spectral Components". In *11th International Workshop on Electromagnetic Compatibility of Integrated Circuits (EMC Compo)*, pages 39–44, July 2017.

[9] B. Deutschmann. "Spread Spectrum Clocking for Emission Reduction of Charge Pump Applications". In *9th International Workshop on Electromagnetic Compatibility of Integrated Circuits (EMC Compo)*, pages 123–128, Dec 2013.

[10] F. Galtie´ and C. Marot. "Spread Spectrum Clocking applied to Charge Pump for Conducted Emission improvement in Automotive". In *Asia-Pacific Symposium on Electromagnetic Compatibility and 19th International Zurich Symposium on Electromagnetic Compatibility*, pages 267–270, May 2008.

[11] A. Benedicks, S. Frei, N. Hees, and M. Wiegand. "Systematic Reduction of Peak and Average Emissions of Power Electronic Converters by the Application of Spread Spectrum". *IEEE Transactions on Electromagnetic Compatibility*, 60(5):1571–1580, Oct 2018.

[12] K. B. Hardin, J. T. Fessler, and D. R. Bush. "Spread Spectrum Clock generation for the Reduction of Radiated Emissions". In *Proceedings of IEEE Symposium on Electromagnetic Compatibility*, pages 227–231, Aug 1994.

[13] "A Solution for Peak EMI Reduction with spread Spectrum Clock Generators". In *Semiconductor Components Industries, LLC, Application Note AND9015/D Rev.0*, Jul 2011.

[14] Seung-Wook Oh, Hyung-Min Park, Yong-Hwan Moon, and Jin-Ku Kang. "A Spread Spectrum Clock Generator for DisplayPort 1.2 with a Hershey Kiss Modulation Profile". *Journal of Semiconductor Technology and Science*.

[15] K. Krischan. "Stromrichtertechnik". In *TU Graz, lecture notes, summer term 2016*.

[16] E. Kreyszig. "Determination of Fourier Coefficients Without Integration". In *Advanced Engineering Mathematics, Fifth Edition, Sec. 10.6*, pages 483–488.

[17] H. Hartl, E. Krasser, W. Pribyl, P. Söße r, and G. Winkler. *"Elektronische Schaltungstechnik"*. Pearson Studium, 2008.

[18] F. J. Harris. "On the Use of Windows for Harmonic Analysis with the Discrete Fourier Transform". *Proceedings of the IEEE*, 66(1):51–83, Jan 1978.

[19] M. Neumayr and T. Bretterklieber. "Signal Analysis". In *TU Graz, lecture notes, winter term 2016/2017*.

[20] J. R. Carson. "Notes on the theory of modulation". In *Proc. IRE*, pages 57–64, Feb 1922.

[21] C. Rauscher, V. Janssen, and R. Minihold. *"Grundlagen der Spektrumanalyse"*. Rohde & Schwarz, 2000.

[22] K. Hörmaier, H. Zangl, and H. Zojer. "An EMI Receiver Model to Evaluate Electromagnetic Emissions by Simulation". In *2012 IEEE International Instrumentation and Measurement Technology Conference Proceedings*, pages 2558–2562, May 2012.

[23] H. Hackl and B. Deutschmann. "An EMI Receiver Model to Minimize Simulation Time of Long Data Transmissions". In *2016 Austrochip Workshop on Microelectronics (Austrochip)*, pages 57–62, Oct 2016.

[24] R. Lynn Kirlin, Michael M. Bech, and Andrzej M. Trzynadlowski. "Analysis of Power and Power Spectral Density in PWM Inverters With Randomized Switching Frequency". *IEEE Transactions on Industrial Electronics*, 49(2):486–499, Apr 2002.

[25] A. A. Adnani, J. Duplicy, and L. Philips. "Spectrum Analyzers Today and Tomorrow: Part 1". *IEEE Instrumentation Measurement Magazine*, 14(5):6–11, Oct 2013.

[26] A. A. Adnani, J. Duplicy, and L. Philips. "Spectrum Analyzers Today and Tomorrow: Part 2". *IEEE Instrumentation Measurement Magazine*, 16(6):36–40, December 2013.

[27] T. Karaca, B. Deutschmann, and G. Winkler. "EMI-Receiver Simulation Model with Quasi-peak Detector". In *2015 IEEE International Symposium on Electromagnetic Compatibility (EMC)*, pages 891–896, Aug 2015.

[28] F. Krug and P. Russer. "Quasi-Peak Detector Model for a Time-Domain Measurement System". *IEEE Transactions on Electromagnetic Compatibility*, 47(2):320–326, May 2005.

[29] M. Keller. "Comparison of Time Domain Scans and Stepped Frequency Scans in EMI Test Receivers". In *Rohde & Schwarz, Whitepaper 12.2013-1EE24_1E*, Dec 2013.

[30] N. Moonen, F. Buesink, and F. Leferink. "EMI reduction in sPWM Driven SiC converter based on carrier frequency selection". In *2017 International Symposium on Electromagnetic Compatibility - EMC EUROPE*, pages 1–5, Sep. 2017.